Xuemeng Chen

# Synthesis of single and mixed metal oxides for VOCs oxidation

Helsinki Metropolia University of Applied Sciences
Bachelor's Degree
Environmental Engineering
Thesis
11 May 2012

Metropolia

**Abstract**

| | |
|---|---|
| Author(s)<br>Title<br><br>Number of Pages<br>Date | Xuemeng Chen<br>Synthesis of single and mixed metal oxides for VOCs oxidation<br><br>92 pages + 16 appendices<br>11 May 2012 |
| Degree | Bachelor's Degree |
| Degree Programme | Environmental Engineering |
| Specialisation option | Environmental Construction Engineering |
| Instructor(s) | Dr. Sónia Carabineiro, Assistant Researcher<br>Dr. Esa Toukoniitty, Senior Lecturer |


Volatile organic compounds (VOCs) are important environmental pollutants that can originate from petroleum refineries, fuel storage and loading procedures, painting and printing operations, and motor vehicles. These compounds usually have high vapor pressure, and therefore, easily appear in gaseous form at ambient temperature and atmospheric pressure. In many sectors of industry and traffic, VOCs are regulated to prevent ozone depletion and smog formation; moreover, some of them are also carcinogenic and malodorous. Conventional thermal oxidation requires high operation temperatures (650 to 1100 $^{o}$C), whereas catalytic oxidation can lower the temperature range to around 250-500 ºC and causes less $NO_x$ formation. Therefore, catalytic oxidation is a more energy-efficient and environmentally friendly technology for VOC abatement.

The purpose of this thesis project is to prepare metal oxides for the catalytic oxidation of VOCs. Single and mixed oxides were prepared by the exotemplating method (EX). Two carbon materials, carbon xerogel (CX) prepared by a method described in literature and commercial activated carbon NORIT ROX 0.8 (CROX), were used as templates in the synthesis of copper, iron and nickel oxides. Several zinc, magnesium and lanthanum oxides were made by EX as well, but showed relatively low catalytic activities. The thermal evaporation method (EM) was used for the synthesis of mixed oxides. Also some attempts to prepare materials with perovskite structures were made, by using the glycine-nitrate process (GNP) and a combination of GNP with EX. All synthesized samples were characterized by thermogravimetry and differential scanning calorimetry, $N_2$ adsorption and temperature programmed reduction. Selected samples were analyzed by X-ray diffraction (XRD). The materials obtained were tested for oxidation of VOCs (ethyl acetate and toluene). Also a series of gold nanoparticle doped oxides, along with the corresponding commercial oxide supports, were tested in the oxidation of ethyl acetate.

CX templated CuO showed the best performance among all tested single oxides. Large improvements were found upon gold addition to NiO and $Y_2O_3$, in comparison to the respective commercial oxides. In mixed oxides, Ce-Co samples showed the highest activity for VOCs oxidation. Ce-Cu and La-Co materials also had good catalytic performances.



| | |
|---|---|
| Keywords | Metal oxides, catalytic oxidation, VOCs abatement, gold, exotemplates, evaporation method, glycine-nitrate process, perovskite. |

**Contents**

**Acknowledgements**

**Abbreviations**

*Dedicated to my grandparents*

**Acknowledgements:**

First of all, I would like to acknowledge the following organizations and intuitions: IAESTE –The International Association for the Exchange of Students for Technical Experience, for providing me this precious work opportunity; APIET - Associação Portuguesa Para Permuta Internacional Estudantes Estagiários Técnicos for offering me a monthly scholarship during my working period in Porto; the University of Porto and the Associate Laboratory LSRE/LCM for accepting my internship program.

Secondly, I would like to show my appreciation to the following people: Finnish Consul at Embassy of Finland, Lisbon, Mr. Tero Hyttinen; Exchange Coordinator of IAESTE Portugal, Mr. Miguel Silveiro; and Senior Programme Adviser at CIMO, Ms. Niina Juuti. Without the generous help and arrangement they offered, I could not have made this trip, nor done this work.

I am also very thankful to the LCM staff, namely Prof. José Luís Figueiredo, Prof. José de Melo Órfão, Prof. Joaquim de Faria and Prof. Fernando Pereira, for allowing me to use the laboratory facilities and resources. Also I want to thank all the team members of LCM for all the help they offered me and for making me such a sound and pleasant environment in the lab.

Last but the most, I would like to express my sincere gratitude to Dr. Sónia Carabineiro, my supervisor, and also to Ph.D. student Sandra Bastos at LCM for their munificent teaching and liberal guidance as well as the valuable suggestions and assistance offered to me in work and genuine care and help in life. I also used some gold/oxide samples that were previously prepared by Dr. Sónia Carabineiro and carbon xerogel prepared by Ph.D. student Sandra Bastos, and by the former IAESTE student Thanakrit Thavorn-amornsri.

Additionally, I would like to acknowledge the characterisation of several samples by X-ray diffraction carried out by Prof. Pedro Tavares from Universidade de Trás-os-Montes and Alto Douro, Portugal. The high-resolution transmission electron microscopy images used in this work for the Au/oxides catalysts were obtained by Dr. Nina Bogdanchikova (Universidad Nacional Autónoma de Mexico), Dr. Miguel Avalos-Borja (Instituto Potosino de Investigación Científica y Tecnológica, Mexico) and Dr. Alexey Pestryakov (Tomsk Polytechnic University, Russia), in a previous collaborative work of Dr. Sónia Carabineiro.

PT/2011/59

**Abbreviations:**

| | |
|---|---|
| Vocs | Volatile Organic Compounds |
| Cfcs | Chlorofluorocarbons |
| Hcfcs | Hydrochlorofluorocarbons |
| NMVOC | Non-Methane VOC |
| IPCC | Intergovernmental Panel On Climate Change |
| NEC | National Emission Ceilings |
| PM | Particulate Matter |
| LEL | Lower Explosive Limit |
| EU BREF | European Union Best Available Techniques Reference Document |
| AES | Auger Electron Spectroscopy |
| BET | Brunauer, Emmett And Teller |
| EX | Exotemplating Method |
| EM | Evaporation Method |
| EXAFS | Extended X-Ray Absorption Fine Structure |
| GNP | Glycine-Nitrate Process |
| GN-EX | A Combination Of Glycine-Nitrate Process And Exotemplating Method |
| LEIS | Low-Energy Ion Scattering |
| SEM | Scanning Electron Microscopy |
| SIMS | Secondary Ion Mass Spectrometry |
| TEM | Transmission Electron Microscopy |
| TG-DSC | Thermogravimetry And Differential Scanning Calorimetry |
| TPR | Temperature Programmed Reduction |
| TPD | Temperature Programmed Desorption |
| XAFS | X-Ray Absorption Fine Structure |
| XRD | X-Ray Diffraction |
| XPS | X-Ray Photoelectron Spectroscopy |
| HRTEM | High Resolution Transmission Electron Microscopy |

# 1. Introduction

The purpose of this work is to synthesis catalytic active metal oxides for volatile organic compounds (VOCs) abatement. Background information on VOCs and their impacts are introduced in this Section. The legislation and available control technologies regarding VOCs are also presented here with the emphasis on catalytic oxidation. This section also includes the theoretical background of the material synthesis methods and various characterisation techniques used in this work.

## 1.1. Volatile Organic Compounds and Their Impacts

Volatile organic compounds (VOCs) are a group of organic compounds with high vapor pressure, often present as gases at ambient temperature and atmospheric pressure. Their emissions can be originated from various different human activities, such as painting procedures, petroleum refineries, solvent cleaning, fuel storage and loading operations, printing operations, and motor vehicles [1].

The EU Directive 1999/13/EC dealing with the limitation of emissions of VOCs, due to the use of organic solvents in certain activities and installations, defines them as any organic compounds having a vapour pressure of 0.01 kPa or more at 293.15 K, or having a corresponding volatility under the particular conditions of use [2]. Halogenated organic compounds, such as chlorofluorocarbons (CFCs) and hydrochlorofluorocarbons (HCFCs), are also included. Examples of other common VOCs comprise acetone, ethyl acetate, benzene, toluene and methyl chloride [3].

These compounds, when emitted into atmosphere, are capable of undergoing reactions with $NO_x$ in the presence of sunlight to form photochemical oxidants. The most well known photochemical oxidants are ozone ($O_3$), peroxyacetyle nitrate (PAN) and hydrogen peroxide ($H_2O_2$). For this reason, VOCs are regarded as ozone precursors for the potential formation of troposphere ozone. $O_3$ at ground level can cause various types of damage to human health, vegetation, forests and buildings. Some adverse effects, such as damage to human health and morphological, biochemical, and

functional changes in the respiratory tract, as well as decreases in host defence functions on humans; visible leaf injury, growth and yield reductions, and altered sensitivity to biotic and abiotic stresses on vegetation and forests; and acceleration of material degradation on buildings, have been reported [4]. As for the special groups, namely CFCs and HCFCs, which are also commonly known by the trade name Freon, they are active $O_3$ reducers and greenhouse gases, with a much higher potential than $CO_2$ to enhance the greenhouse effect (defined as relative forcing by the Intergovernmental Panel on Climate Change -IPCC) [5]. The phase-out of the productions and consumptions of these compounds has been agreed internationally upon the Montreal Protocol, where the treaty provided a timetable for the phase-out management plan for each group of compounds: complete phase-out of CFCs achieved by 2010 and of HCFCs by 2030 in industrialized countries but by 2040 in developing countries [6]. In addition, VOCs are responsible for the formation of secondary particulate matters in the atmosphere, which can further result in smog formation. The fine particles are formed together with other substances, such as $NO_x$, $SO_x$ and $NH_3$, through nucleation processes, and the resulted particulates usually bear diameters of microns or even nanometres which can penetrate into the human thorax causing premature deaths and reducing quality of life by aggravating respiratory conditions such as asthma [4]. Therefore, in order to minimize the negative impacts, VOCs are regulated in many sectors of industry and traffic. Moreover, some of these compounds are also carcinogenic and malodorous [7].

### 1.2. Legislations and Statistics

And the European Union has set several legislations on VOC emissions: Directive 1994/63/EC is set for petrol vapor recovery during storage and distribution, Directive 2009/126/EC for petrol vapor recovery at gasoline stations; specifications of different fuel types are defined by Directive 2009/30/EC; emissions from motor vehicles are regulated by Directive 1996/69/EC, Directive 1999/96/EC (ignition engines) and Euro emission standards, Euro 5 and Euro 6 for light duty vehicles and Euro 3 for motorcycles and mopeds; in the industrial sector, Directive 1999/13/EC sets limits for solvents and Directive 2004/42/EC for paints, varnishes and vehicle refinishing products. Directive 2001/81/EC sets National Emission Ceilings (NEC directive) for certain atmospheric pollutants ($SO_2$, $NO_x$, non-methane VOC – NMVOC, and $NH_3$) to be

achieved before 2010. A consolidated NEC Directive for the EU 27 as an amended version of NEC directive was released by the EU in 2009 due to the accession of new Member States. Since the entering into force of this legislation, NMVOC emissions in the relevant member states showed continuously declining tendency as exhibited in Figure 1 (EC-15 countries are shown as examples). Most member states had successfully reduced their NMVOC emissions to lower levels than the limits set in NEC directive by 2010, however, with the exceptions of Denmark, Germany and Spain, which are marked with red colour in Figure 2.

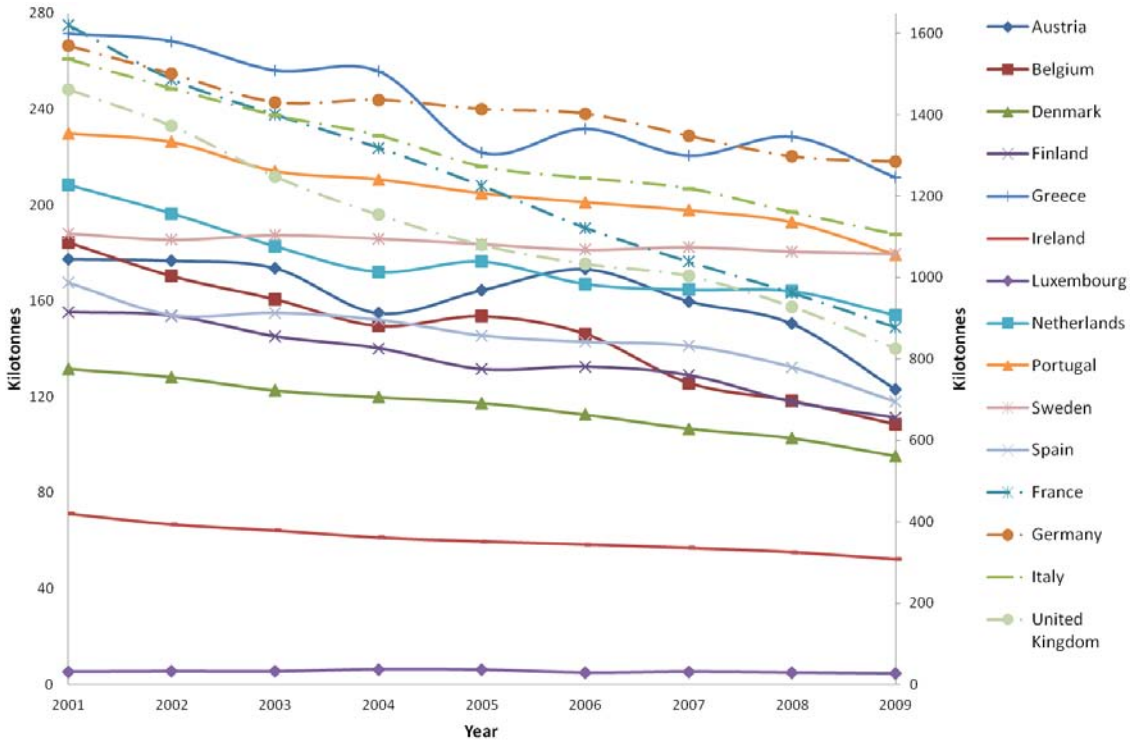


Figure 1: NMVOC emissions (kilotonnes) from year 2001 to 2009 in EC-15 countries. Countries marked with a dashed line are presented with a scale on the right-hand side. Emission data are taken from Eurostat (http://epp.eurostat.ec.europa.eu/portal/page/portal/eurostat/home/). Due to the unavailability of NMVOC emission data for the year 2010 and thereafter, this Figure only includes data until 2009.

In order to fulfil the scenario set out in Thematic Strategy on Air Pollution [9], the NEC directive was reviewed and evaluated based on the National Programmes 2002 and 2006. A revision of the NEC directive is under preparation by the Community, and it will set emission ceilings to be respected by 2020, for the four already regulated substances and for the primary emissions of $PM_{2.5}$ (particulate matter with diameter smaller than 2.5 μm) as well [10].

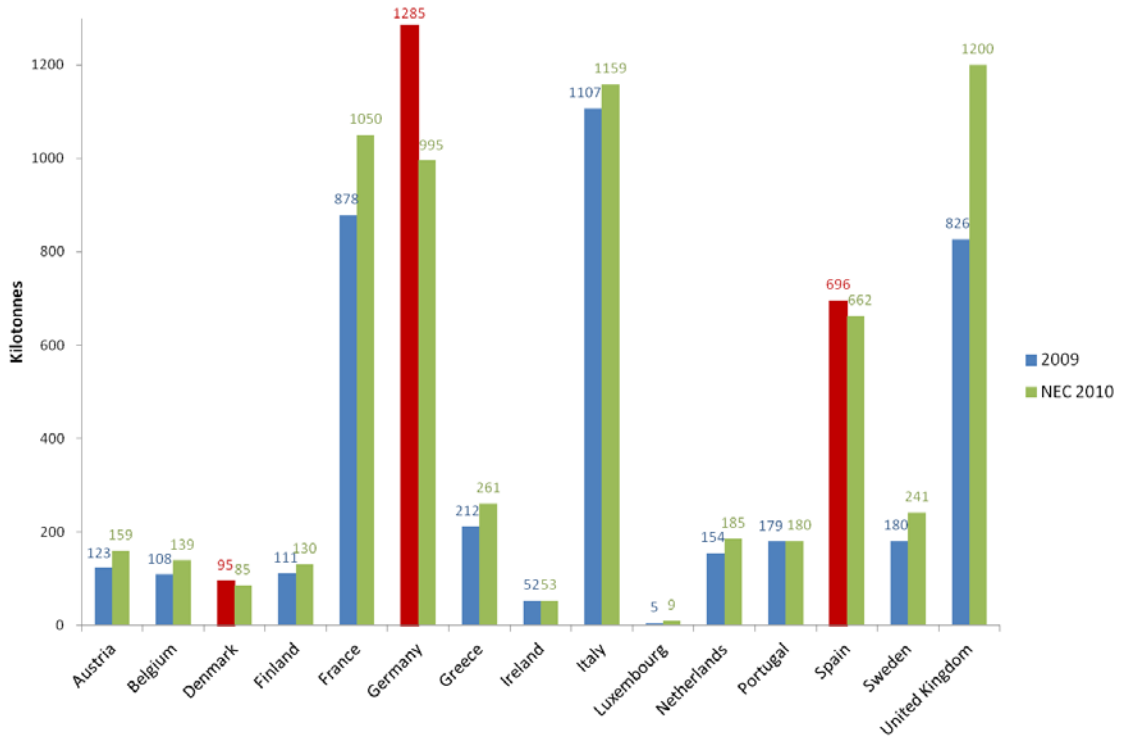


Figure 2: Comparison of VOC emission in each EC-15 country with NEC 2010. Red color indicates the exceeding of National Emission Ceiling. The NEC data come from Directive 2001/81/EC [8].

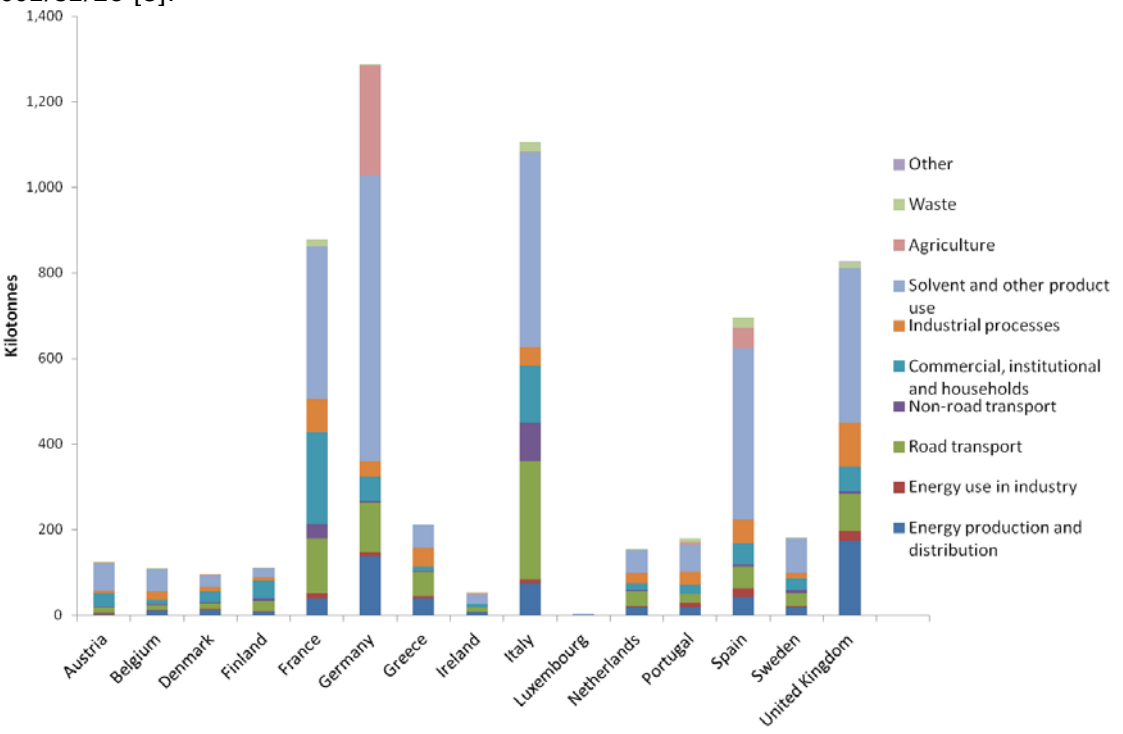


Figure 3: NMVOC emissions of 2009 in EC-15 countries by source sector.

Figure 3 shows the NMVOC emissions by source sectors in the year 2009 for each EC-15 country. Emissions from solvent and other product use together with emissions from industrial processes account for the largest proportion in the total amount in all

EC-15 member states. The second largest contributors to VOC emissions in different countries are transportation (mainly road transport), energy production and distribution as well as commercial, institutional and households with varying portions.

## 1.3. Control Technologies of Volatile Organic Compounds

Various VOC control technologies have been developed as a result of the promotion in political, social, and economic attention on environmental issues and life quality. These technologies can be classified into two main categories: process and equipment modification as well as add-on-control techniques [3], as displayed in Figure 4.

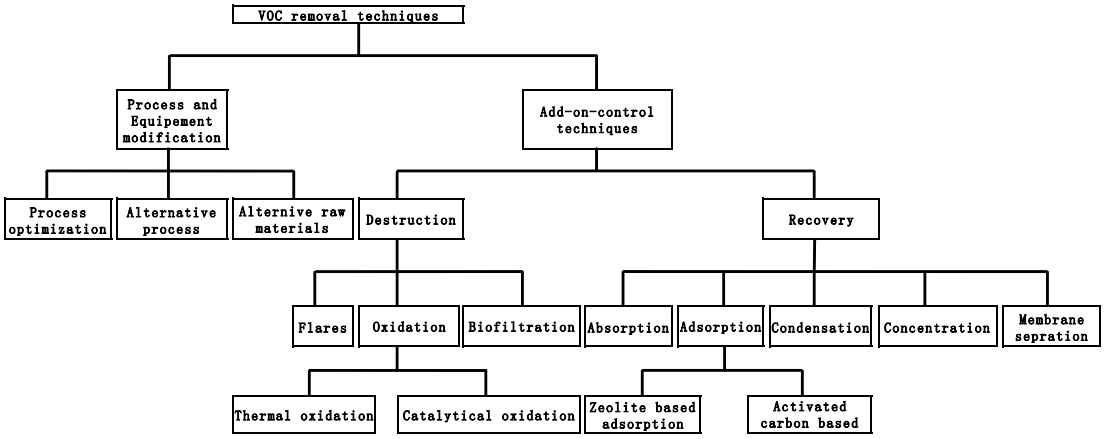


Figure 4: Classification of VOC control techniques [3, 11].

Priority in technique solution for VOC abatement should be given to process and equipment modification. Upgrading installation and using less odorous raw material and/or process can effectively minimize waste generation with high efficiency. However, constrains from the characterization of the process, availabilities of technology, raw material or equipment, the requirement of control level as well as cost considerations usually limit the applicability of this pathway to various extents. As a consequence, seeking alternative solutions in add-on control techniques is often the case.

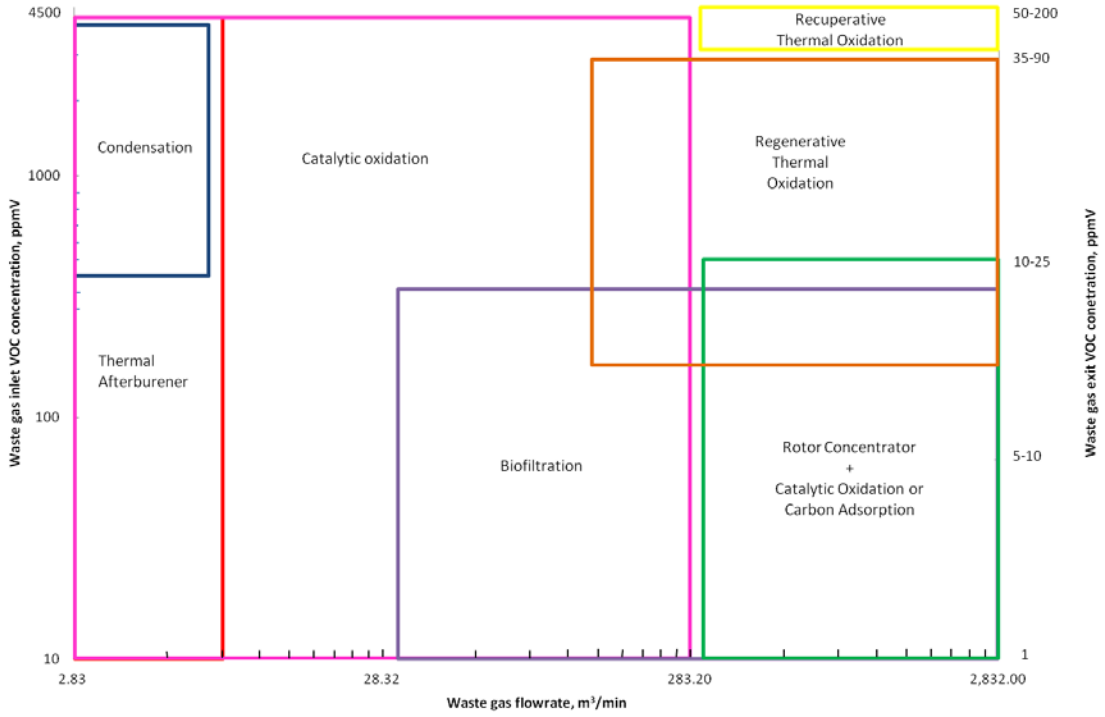


Figure 5: Selection map of add-on control techniques for VOC abatement. Adapted from [11].

The selection of an appropriate add-on control technique is mainly restricted by four criteria: permitted emissions, waste gas flow rate, VOC concentration in the inlet stream, and costs [11]. Figure 5 demonstrates a selection map of the most popular add-on control techniques for VOC abatement based on the lowest net costs in 2002, assuming no halogenated organics, catalyst poisons or particulates in the waste gas stream and 25% lower explosive limit (LEL) to be 4500 ppm. The operation ranges for different techniques shown in the Figure 5 are determined upon the waste gas flow rate and concentration for the most efficient and cost-effective performance of the devices; however, technically, many of these devices also have the capability to deal with conditions outside the indicated ranges, although possibly with less cost-efficiency [11]. The application of a pretreatment on the inlet waste gas may be necessary in some cases to reduce the moisture content or remove particulate matter. According to the EU BREF (Best Available Techniques reference document) on Common Waste Water and Waste Gas Treatment / Management Systems in the Chemical Sector, recovery techniques are often also applied as pretreatment to recover the main VOC load before downstream abatement facilities [12], especially when waste gas inlet stream contains valuable VOC with considerable concentration.

As can be seen in Figure 5, catalytic oxidation tolerates a much wider operation range than any other technique, and has very promising removal efficiency. The catalysts accelerate the oxidation rate and decrease the activation energy required to initialize the reaction, therefore allowing it to occur at a lower temperature than conventional thermal oxidation, which requires high operation temperatures, typically from 650 to 1100 $^{o}$C [3, 11]. Catalytic oxidation, however, needs only around 250-500 $^{o}$C, consequently originating lower $NO_x$ formation, which is a more environmentally friendly solution in VOC abatement [1, 13].

## 1.4. Catalysts for VOC Abatement

The catalysts used for VOC control are usually either supported precious metals, supported or unsupported metal oxides, or precious metal doped metal oxides, usually in the nano-scale. Platinum and palladium are the common precious metals used in such applications [11, 14]. Gold doped catalytic materials have also been investigated [13, 15-17]. Metal oxides based catalysts for oxidation reaction, such as manganese dioxide [11, 13], copper oxide [18, 19], nickel oxide [15, 19] and iron oxide [16, 20], often fall in the transition range. Common support materials include alumina [21], titania [22], zirconia [23], zeolites [19] and carbon based materials [18]. It is reported that although metal oxides based catalysts are more resistant to poisoning phenomena, generally they are less active than the supported precious metals in oxidizing VOC streams [24, 25]. However, alternatively mixed oxides [15, 26-28], perovskite [29-31] and cryptomelane type oxides [24, 32] show good activities in catalytic oxidation of VOCs. These materials are heterogeneous catalysts, as the catalytic oxidation of gaseous VOC occurs at the surface of the solid catalyst surface. In general, the five elementary steps are involved in the reaction: (i) transport of VOC molecules to the active sites on the catalysts; (ii) adsorption of VOC molecules onto these sites; (iii) decomposition of VOC molecules to $CO_2$ and $H_2O$ either directly or through some intermediate; (iv) desorption of the products; and (v) transport of the products from the catalyst surface to the gas stream [33].

In order to obtain effective catalysts which are resistant to poisoning with relatively low cost, porous materials with large surface area and tunable textural properties are of more interest. This can be achieved by using treated or alternative support materials,

changing the type and amount of previous metal contents, or seeking promotions in material properties of the synthesized catalysts.

## 1.5. Catalyst Synthesis

The preparation method of catalysts can have a critical influence on the morphology of the resulting material [34], and consequently affect the catalytic activities. A lot of efforts have been made in the development of preparation procedures for the ability to control particle size, shape, size distributions and composition. “Bottom-up” and “top-down” are the two main approaches in the preparation of nano-scale materials. Breaking down larger starting materials to desired sizes is the fundamental idea in the “top-down” method, whereas “bottom-up” deals with permutation and combination of atoms and molecules for the formation of the final products, the latter being more attractive in the synthesis of nanostructured materials [35]. Various procedures can be used in the preparation of nanostructured metal oxides for catalytic applications, including co-precipitations, sol-gel processes, solvothermal techniques, micro - emulsion techniques, combustion methods, vapor condensation procedures, spray pyrolysis, and templated/surface derivatized nanoparticles [35].

The purpose of this work was the preparation of active metal oxide based catalysts for the oxidation of VOCs. The synthesis procedures involved in this work were the exotemplating technique (EX), the evaporation method (EM) and the glycine - nitrate process (GNP).

### 1.5.1. Exotemplating Method

Exotemplating, together with endotemplating, are the two categories of templating approaches (Figure 6). In endotemplating, an isolated precursor acts as the template and is occluded into the growing solid particle. Exotemplating is also known as nanocasting, in a similar way as the casting process in macro scale. A porous solid provides a scaffold with voids which are filled up with the precursor for another solid to be obtained [24, 36]. In both pathways, the template material is removed after the target solid is formed as demonstrated in Figure 6.

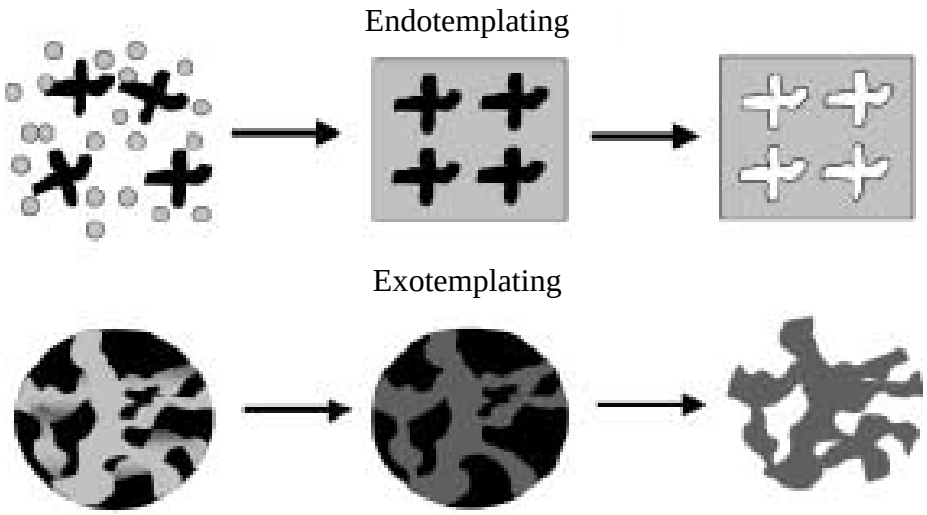


Figure 6: Scheme of endotemplating and exotemplating procedures [36].

By using the templating method, a high degree of control over the structural and textural properties of the material can be achieved [36]. Molecules, especially organic, and supramolecular surfactant aggregates are typical endotemplates used for the synthesis of zeolitic and ordered mesoporous oxides [36]. Carbon materials however, are popular for exotemplating, as their large surface area and highly porous structure can function as the suitable mould (template) for the precursor of the desired material. Plus, the low cost and the fact that they can easily be removed by combustion, makes them potential choice candidates [24].

### 1.5.2. Evaporation Method and Glycine - Nitrate Process

Both the evaporation method and the glycine-nitrate process are within the scope of thermal decomposition of solid coordination compounds, the former belonging to the co-precipitation category and the latter to combustion methods. The coordination compounds can also be known as metal complexes, which consist of metallic cations and surrounding arrays of molecules or anions (organic ligands). The organic skeletons of the coordination compounds can be viewed as molecular templates for the final metal oxide. Metal oxides or pure metals can be made by thermal decomposition in air

or inert atmosphere. Mixed oxides can also be easily synthesized this way, as well as materials with certain structures, such as spinel ($AB_2O_4$) or perovskite ($ABO_3$) [37].

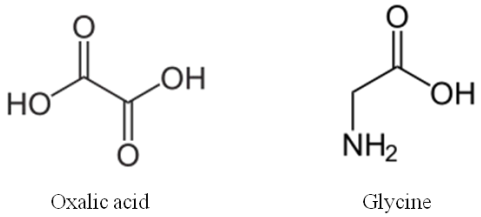


Figure 7: Structural formula of oxalic acid and glycine.

Solid oxalates are formed in the evaporation method, as ethanol coming from the metal precursor solutions is evaporated, after the addition of oxalic acid (Figure 7). Later, oxalates are decomposed into metal oxides. Glycine-nitrate method is an auto-ignited process, due to the presence of the amino acid ligand in glycine and $NO_3^-$ in metal nitrate precursor [37]. Glycine (Figure 7) acts as the fuel for the auto ignition, with nitrate being the oxidant. Furthermore, glycine also plays the role of a complexant, as the amine group tends to complex with transitional metal ions and carboxyl group bond with alkaline earth metal ions [38].

## 1.6. VOC Oxidation

As described above in Section 1.1, various compounds fall into the category of VOCs. For non-halogenated VOCs, the desired final products from the catalytic oxidation reaction are $CO_2$ and $H_2O$. In some cases, the formation of CO can also be observed, when a less active/selective catalyst is used within the defined temperature range. Two volatile organic compounds were used in this work: ethyl acetate and toluene (Figure 8) that are common volatile organic compounds that can easily affect humans in daily life.

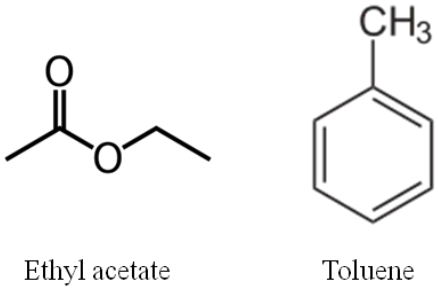


Figure 8: Structural formula of ethyl acetate and toluene.

Ethyl acetate ($C_4H_8O_2$), with CAS number 141-78-6, is a colourless liquid which has an ethereal and fruity smell. It has a boiling point of 77 $^oC$ and vapour pressure of 9.686 kPa at 20 °C ( 2.3 kPa for water, 5.9 kPa for ethanol) [39]. It is manufactured mainly for solvent usage worldwide, and can be found in glues, nail polish removers, and cigarettes. Toluene ($C_7H_8$), CAS number 108-88-3, with a boiling point of 110.6 °C and a vapor pressure of 2.734 kPa at 20 °C [39], is also a colourless liquid. It has a typical smell of thinner, as it is commonly used in paints. Traces of toluene can also be found in printing ink, rubber, glues and leather tanners. Due to the benzene ring structure, higher temperature is required for its decomposition in oxidation reaction.

## 1.7. Characterization Techniques of Catalytic Materials

Various techniques can be applied in the characterization of catalytic materials and as assistance in sample preparation. These include temperature-programmed techniques, such as temperature programmed reduction (TPR) and temperature programmed desorption (TPD); photoemission and Auger spectroscopy, such as X-ray photoelectron spectroscopy (XPS) and Auger electron spectroscopy (AES); ion spectroscopies, such as secondary ion mass spectrometry (SIMS) and low-energy ion scattering (LEIS); Mössbauer spectroscopy; diffraction and extended X-ray absorption fine structure (EXAFS), such as X-Ray Diffraction (XRD) and X-ray absorption fine structure (XAFS); microscopy and imaging, such as scanning electron microscopy (SEM) and transmission electron microscopy (TEM); vibrational spectroscopy, such as infrared spectroscopy and Raman spectroscopy; as well as calorimetric methods.

The samples synthesized in this work were characterized by thermogravimetry and differential scanning calorimetry (TG-DSC), $N_2$ adsorption, and temperature programmed reduction (TPR). Also X-ray diffraction (XRD) and high resolution transmission electron microscopy (HRTEM) were employed for certain samples.

### 1.7.1. Thermogravimetry-Differential Scanning Calorimetry (TG-DSC)

Thermogravimetry (TG), also known as thermogravimetric analysis (TGA), is a technique used to measure the changes in sample weight with increasing temperature.

Differential scanning calorimetry (DSC) is used to determine the changes in heat flow rate between target sample and reference sample, which can be measured in two systems: heat flux DSC and power compensating DSC. The difference in the heat flow rates is measured directly as the temperature difference in heat flux DSC. However, in power compensating DSC, target sample and reference sample are arranged in two separate small furnaces: each equipped with a heating unit and a temperature sensor to minimize the temperature difference between them [40].

Both TG and DSC are used to study the thermal behavior of a material under heating at a constant rate. TG is one of the primary techniques frequently applied in catalysis, for the determination of transformation of catalyst precursors, for studies of dehydration/dehydroxylation, for the determination of the porous structure of catalysts by adsorption measurements and for studies of the adsorption/desorption properties of gases. In combination with DSC, information such as activation energies and some reaction kinetics features together with weight loss, which are especially useful in catalyst preparation, can be revealed [33].

### 1.7.2. $N_2$ Adsorption

This technique is used to determine the BET surface area and pore size distribution of various solid materials including industrial absorbents, catalysts, pigments, ceramics and building materials [41]. The BET theory was introduced by Brunauer, Emmett and Teller (from where the B.E.T. initials come from) in 1938, and it has been widely applied in surface area calculations for solid materials ever since. In principle, the amount of gas adsorbed can be determined either by volumetric or gravimetric methods based on mass increase. However, nitrogen adsorption isotherms at the temperature of the boiling point of this gas, at ambient atmospheric pressure, are commonly determined by the volumetric method [41]. Before performing gas adsorption experiments, all of the physisorbed species, such as water and oils, should be removed from the solid (absorbent) surfaces in a degassing process. Then the BET surface area can be determined through the monolayer of $N_2$ molecule coverage on the entire adsorbent surface, as shown in the following formula:

$$S_{\mathrm{BET,\ total}} = \frac{v_{\mathrm{m}} \cdot N \cdot s}{V},$$

where $v_{\mathrm{m}}$ is the volume of the adsorbed $N_2$, $N$ is the Avogadro's number, $s$ is the cross section of $N_2$ molecule, and $V$ is the molar volume of adsorbed $N_2$. Knowing the mass of the adsorbent, $m$, the specific surface area $S_{\mathrm{BET}}$ can be obtained as follows:

$$S_{\mathrm{BET}} = \frac{S_{\mathrm{BET,\ total}}}{m}.$$

Further admission of $N_2$ leads to multilayer adsorption, and when the saturation stage is reached, pore size can be determined from equilibrium gas pressure by Barrett, Joyner and Halenda (B.J.H.) or the more accurate Density Functional Theory (DFT) models.

### 1.7.3. Temperature Programmed Reduction (TPR)

Temperature programmed reduction (TPR) is a valuable technique in the characterisation of metallic catalysts. In the catalytic reaction of VOC oxidation, the catalysts (metal oxides) undergo reduction and reoxidation, as the surface lattice oxygen ions are often used to oxidize VOC molecules, and replenished by the oxygen molecules from the gaseous phase. This kind of phenomenon is known as redox catalysis. The mechanism of the catalytic redox processes on metal oxides can be described as follows:

$$\mathrm{Cat\text{-}O + VOC \rightarrow Cat + VOC\text{-}O}$$
$$\mathrm{Cat + O_x\text{-}O \rightarrow Cat\text{-}O + O_x}$$

The VOC molecule is oxidized by the surface lattice oxygen on the catalyst (Cat-O). By taking an oxygen ion from an oxidant ($O_x$-O), the catalyst is reoxidized back to its initial state [42].

By employing TPR, the information on the reducibility of the prepared material surface can be revealed through heating at a constant rate in a reducing atmosphere, typically

$H_2$ diluted with Ar. A thermal conductivity detector (TCD) is often used to monitor the changes in the thermal conductivity of the gas stream. The total amount of $H_2$ consumption during the reduction is obtained through the area under the TPR curve [43].

### 1.7.4. X-ray Diffraction

X-ray diffraction (XRD) is a powerful technique used in the identification of the crystalline phases present in materials and for acquiring information on structural properties, such as strain state, grain size, epitaxy, phase composition, preferred orientation, and structure defects [44]. It is based on the diffraction of X-rays bombarding the sample by the atoms in the material lattice. Figure 9 illustrates the principle of a XRD device.

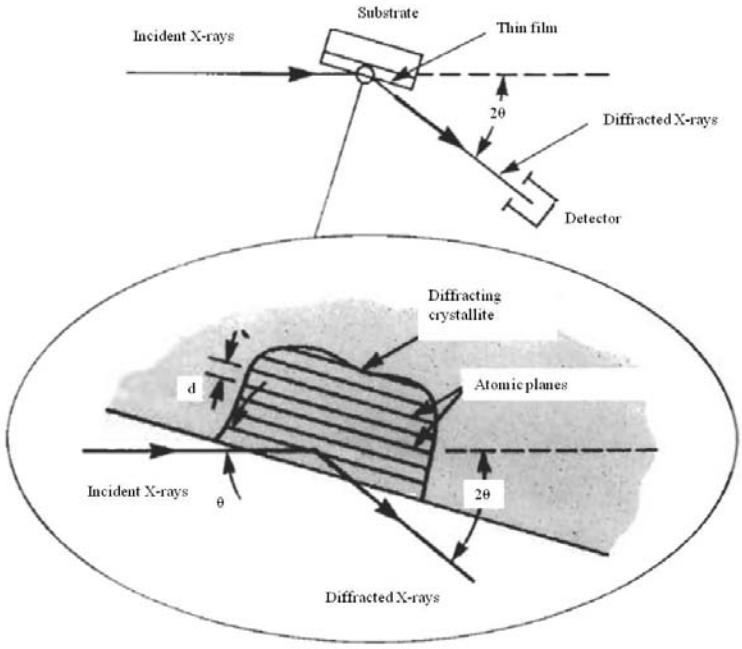


Figure 9: Scheme of a typical XRD experiment [44]

2θ is the angle between the path of the scattered X-ray and its original route, which is the quantity being measured in an XRD analysis. According to Bragg's law, shown below, lattice spacing, which is characteristic of a certain compound, can be determined as follows, [43]:

$$n\lambda = 2d \cdot \sin\theta,$$

where $\lambda$ is the wavelength of the X-rays, $d$ is the distance between two atomic planes, $\theta$ is the angle between the incident X-rays and the scattering plane, and $n$ ($n$ = 1, 2, ...) is the integer called the order of the reflection.

### 1.7.5. High Resolution Transmission Electron Microscopy (HRTEM)

High resolution transmission electron microscopy (HRTEM) is a fundamental characterization technique used to obtain information on the surface structure of the material being examined. Both image and diffraction information of the sample surface can be provided. Figure 10 demonstrates the basic principle. A focused incident beam of electrons is subjected onto a thin film (less than 200 nm) of sample being analyzed. The incident electrons that pass through the sample are partially transmitted and partially diffracted, both being collected as signals. After magnification by a factor of 50 to $10^6$, it is further projected onto a detector, usually a fluorescent screen, a film plate, or a video camera [44].

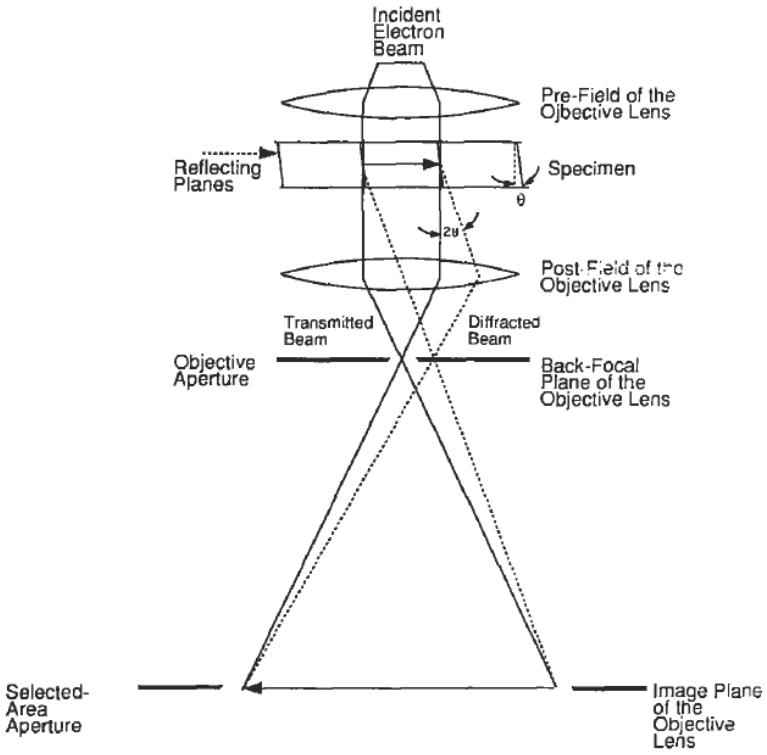


Figure 10: schematic representation of the theory that TEM is based on [44].

Atomic species cannot be identified with HRTEM alone, but this is possible when HRTEM is associated with further characterization techniques, such as energy-dispersive X-ray spectroscopy (EDXS), electron energy loss spectroscopy (EELS), extended X-ray energy loss fine structure (EXELFS), backscattered and secondary electron imaging as the interaction of the highly energetic beam of electrons with the sample matter generates characteristic radiation and particles for different elements [44].

# 2. Experimental Procedure

## 2.1. Single Metal Oxides

The synthesis, characterization, and catalytic experiments of single metal oxides, including gold nanoparticle doped oxides (prepared by Dr. Sónia Carabineiro), are discussed here. Emphasis is placed on exotemplated copper, nickel and iron oxides. Zinc, magnesium and lanthanum oxides were also synthesised by the exotemplating method, but they are presented in Appendix 1, together with their catalytic results, since they did not show relevant activity.

### 2.1.1. Synthesis of Catalysts

The method used in preparing metal oxides by exotemplating was based on the procedure described by Schwickardi et al. [45], which was similar to that used by Bastos et al. [13, 24]. As concluded in earlier studies, the use of metal-nitrate precursors results in the formation of materials with higher surface areas [36]. In this work, metal nitrates were chosen as precursors for both single (discussed in this Section) and mixed oxides (discussed in Section 3.2).

Two different carbon materials were used here as exotemplates: Activated carbon NORIT ROX 0.8 (CROX) and carbon xerogel (CX). The latter was previously prepared by Ph.D. student Sandra Bastos, through condensation of resorcinol and formaldehyde, following the method described by Job et al. [46]. The particle sizes ($D$) of both carbon template materials used in the synthesis of all oxide samples were between 0.05 mm

and 0.25 mm; CX with particle size less than 0.1 mm was used in the preparation of copper oxide as well, for comparison.

Saturated metal nitrate precursor solutions were added to the templates for impregnation. For each 1.7 g of carbon template, 7 ml of saturated nitrate precursor was used as described in Schwickardi et al. [45] and Bastos et al. [24]. Some efforts were also made to study the impregnation efficiency by comparing the use of 7 ml of precursor and impregnation performed based on a maintained Spv-ratio of 1.5. The Spv-ratio expresses the relationship between the added volume of the precursor solution and the available pore volume of the active carbon given by the following formula:

$$Spv\text{-}ratio = \frac{V_{\text{solution}}}{m_{\text{AC}} \cdot v_{\text{pore}}},$$

where $V_{\text{solution}}$ is the volume of the precursor solution (ml), $m_{\text{AC}}$ is the mass of the activated carbon (g) and $v_{\text{pore}}$ the specific pore volume (ml/$g_{AC}$) of activated carbon [47]. Specific pore volumes of template materials are shown in Table 1.

Table 1: Specific pore volumes of template materials.

| Specific pore volume (ml/g) | |
|---|---|
| CX | 1.32* |
| CROX | 0.67** |

* value taken from Table 2 of S.S.T. Bastos et al.[24]

** value taken from Table 1 of S.A.C. Carabineiro et al. [48]

For this purpose, the amount of precursor used was cut down to 3.4 ml for CX and 1.7 ml for CROX. Also the effects of adding isopropanol and pre-drying templating materials were investigated. A detailed discussion on these results can be found in Appendix 2. The excess precursor solution was then removed by vacuum filtration. The residual liquid on the surface of the template material was removed by “sandwiching” the solid phase between two sheets of filter paper and squeezing gently. Then the impregnated template material was dried overnight in an oven at about 80 ºC and calcined in a furnace, first at a low temperature (between 200 ºC and 250 ºC) for the

decomposition of the precursor and then at a high temperature (around 350 ºC) in order to burn out the carbon templates, under 100 $cm^3$/min of air flow, with a heating rate of 2 ºC/min. A list of detailed temperature programmes used for the different metal oxide samples is shown in Table 2. The intermediate temperatures were chosen based on the TG/DSC results, as explained in Section 3.1.1.1.

Table 2: Temperature programs used for CuO, NiO and $Fe_2O_3$ made with CX and CROX.

| Metal oxides | Heating rate (ºC/min) | Intermediate *T* (ºC) | Final *T* (ºC) |
|---|---|---|---|
| CuO | 2 | 220 | 350 |
| NiO | 2 | 250 | 350 |
| $Fe_2O_3$ | 2 | 200 | 350 |

The chemical formulas do not mean the phases present in the prepared samples.

#### 2.1.1.1. Gold Nanoparticle Doped Metal Oxides

The oxide samples doped with gold were previously prepared by Dr. Sónia Carabineiro, using a double impregnation method (DIM) as described in Bowker et al. [49]. Commercial metal oxides (CuO from Riedel-de Haën, NiO from Aldrich and $Fe_2O_3$ from Sigma-Aldrich) were used as supports. Similar to traditional impregnation, where the support is impregnated with a solution of $HAuCl_4$ using sonication, a second impregnation step with addition of an aqueous solution of $Na_2CO_3$ (1 M) was additionally introduced during the sample preparation, under constant ultrasonic stirring [50].

### 2.1.2. Material Characterizations

TG-DSC was carried out in a Netzsch STA 409 PC Luxx1 apparatus. The mass used for each analysis was around 15 mg. This amount of sample was weighted in a microbalance and placed in a ceramic crucible. Experiments were carried out in air, with a heating rate of 10 $^oC$/min, until 800 $^oC$.

BET surface areas were calculated from the $N_2$ adsorption isotherms obtained in a Quantachrome Instruments Nova 4200e. All samples were previously degassed before analysis at 160 $^{o}$C, for 5 h.

TPR experiments were carried out in a fully automated AMI-200 Catalyst Characterization Instrument (Altamira Instruments), to acquire information on the reducibility and the amount of surface oxygen of the samples.

XRD analysis was carried out, with the help of Professor Pedro Tavares, in Universidade de Trás-os-Montes e Alto Douro, Portugal, in a PAN'alytical X'Pert MPD equipped with an X'Celerator detector and secondary monochromator (Cu Kα = 0.154 nm, 50 kV, 40 mA). The collected spectra were analyzed by Rietveld refinement using the PowderCell software, allowing the determination of the grain size.

The gold nanoparticle doped metal oxides were additionally characterized using high resolution transmission electron microscopy (HRTEM) on the FEI Tecnai F30 instrument by Dr. Nina Bogdanchikova from Universidad Nacional Autónoma de Mexico, Dr. Miguel Avalos-Borja from Instituto Potosino de Investigación Científica y Tecnológica, Mexico, and Dr. Alexey Pestryakov from Tomsk Polytechnic University, Russia.

### 2.1.3. Catalytic Performance Tests

The exotemplated metal oxides, gold loaded oxides as well as commercial oxides were tested as catalysts for the oxidation of ethyl acetate in a special set-up previously built by Ph.D. student Sandra Bastos in LCM (Laboratory of Catalysis and Materials), as schematized in Figure 11.

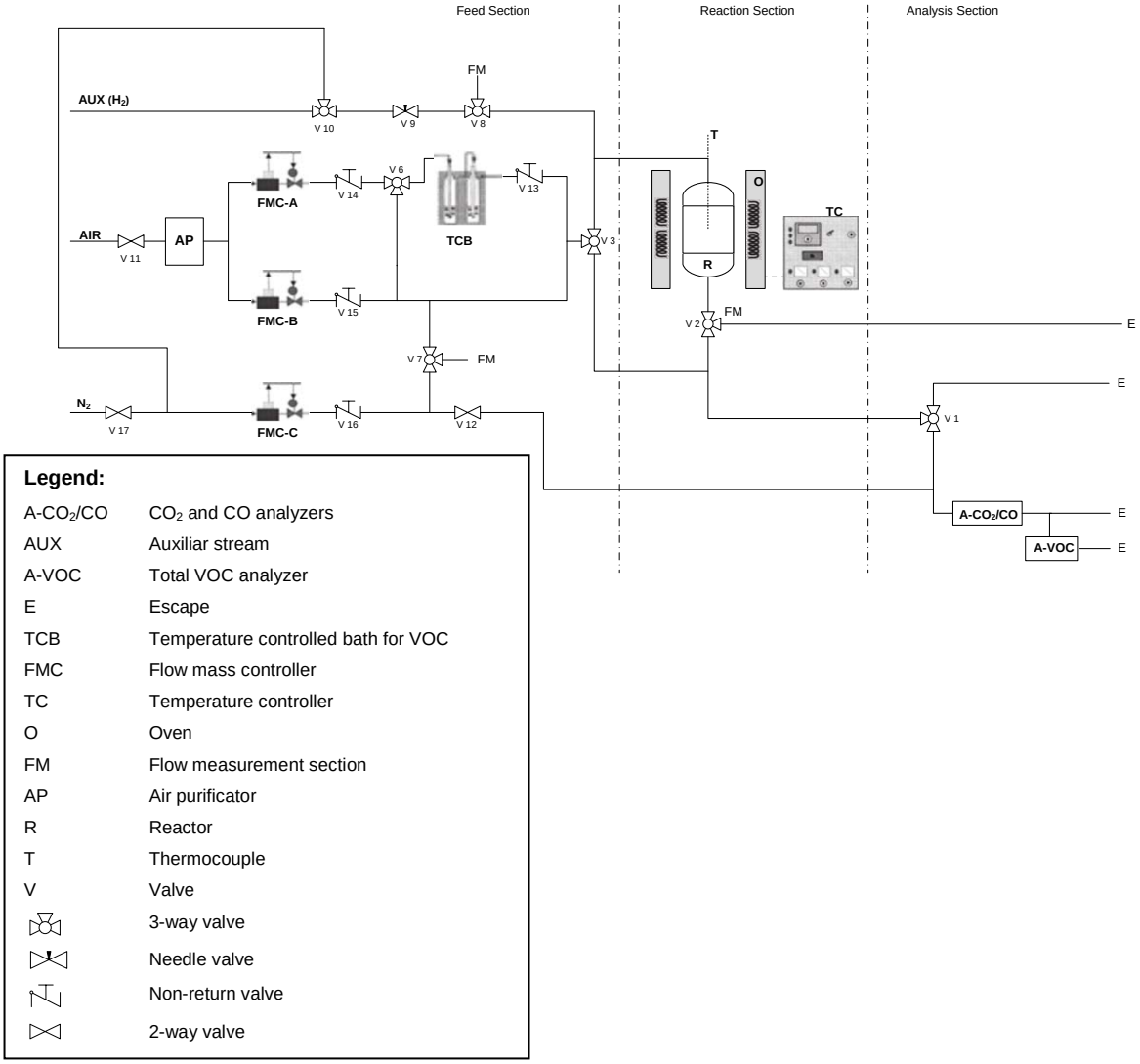


Figure 11: VOC-Set-Up Scheme [51].

The VOC Set-Up consists of a U-shaped quartz tube fixed-bed reactor with a 6-mm internal diameter as shown in Figure 12 (inset), placed inside a temperature controlled electrical furnace (shown in the circle); a VOC generator that includes two VOC saturator bottles and a cooling bath; a gas purificator, a gas holder and a flow controller composed of the air feed section; and the parameter analyzers including a silica-based $CO_2$ non-dispersive infrared (NDIR) sensor (Vaisala GMP222), a total volatile organic compounds analyzer MiniRAE2000 (which had different sensitivity for each VOC), a portable CO sensor, as well as a K type thermocouple placed in the middle of the catalyst bed to measure the temperature of the reaction [24].

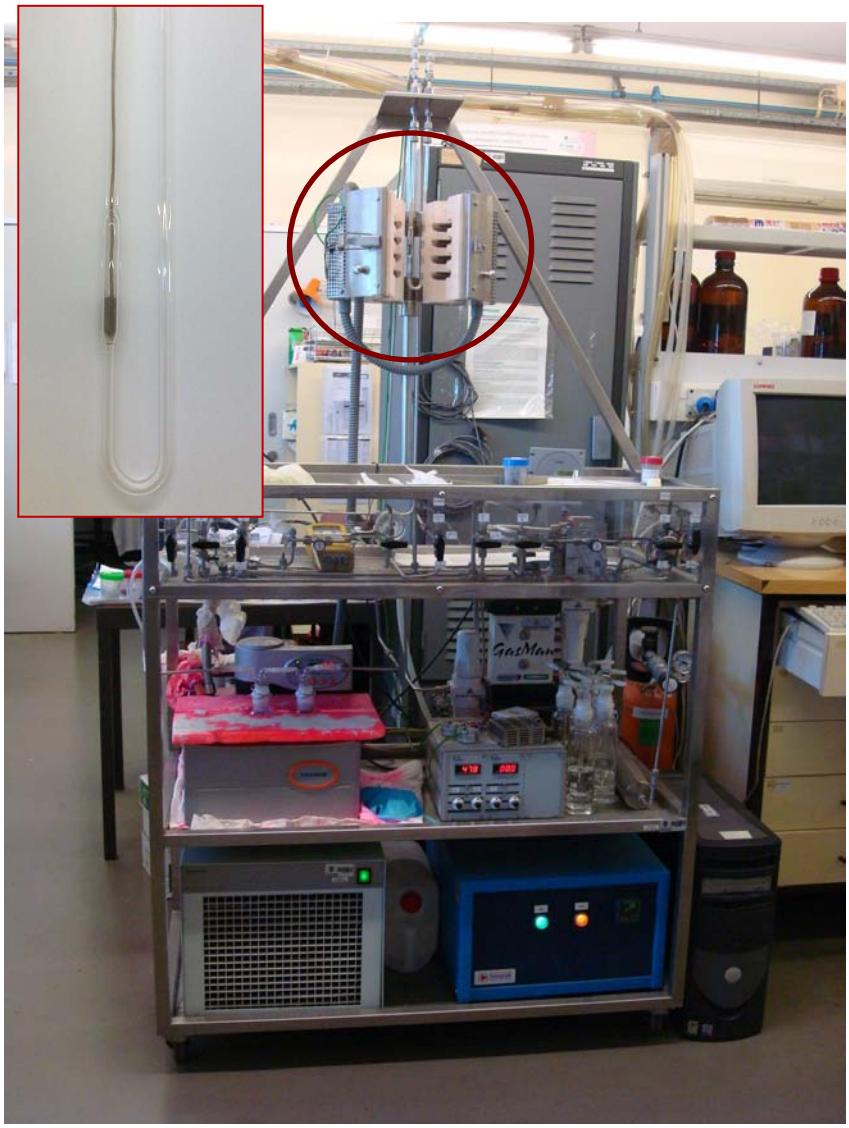

Figure 12: VOC Set-Up. The furnace is signaled with a circle and a closer detail of the reactor, which is inside the furnace, is shown as inset on top left.

The catalytic reactions were performed with a total flow of 500 $cm^3$/min (measured at room temperature and atmospheric pressure), which corresponded to a space velocity of 53050 $h^{-1}$ (determined in terms of total bed volume), having a composition of 1000 $mg_{Carbon}/m^3$ (~466 ppmV of ethyl acetate and ~226 ppmV of toluene) [24]. Each experiment used about 50 mg of catalyst, which was mixed thoroughly with an inert (SiC, carborundum) with dimensions between 0.2 mm and 0.5 mm. The total volume of the mixture of catalyst sample and inert was about 0.5 $cm^3$. A pretreatment was carried out before the catalytic reaction. The temperature used in pretreatments and catalytic reactions was the maximum temperature used during the calcination stage of sample preparation (this temperature was chosen based on the TG/DSC results, as described in Section 3.1.1.1.). Two cycles of increasing and decreasing temperature

were performed for each catalyst at a heating rate of 2 $^{o}$C/min. The extent of VOC oxidation was evaluated by continuously monitoring the $CO_2$ formation with the $CO_2$ sensor. The concentration of VOC in the effluent was measured with the total VOC analyzer. In case of incomplete conversion of VOC into $CO_2$ and $H_2O$, the portable CO sensor was also used to obtain information on CO formation at the maximum reaction temperature during experiments. The catalytic performance was presented as $X_{CO2}$, which was obtained by the following equation [24]:

$$X_{CO_2} = \frac{F_{CO_2}}{\nu \cdot F_{in,\,VOC}},$$

where $F_{in,\,VOC}$ is the inlet molar flow rate of VOC, $F_{CO2}$ is the outlet molar flow rate of $CO_2$, and $\nu$ is the number of carbon atoms in the VOC molecule (for ethyl acetate, $\nu$ = 4, and for toluene, $\nu$ = 7).

## 2.2. Mixed Metal Oxides

In this work, three primary synthesis methods were involved for the preparation of mixed metal oxides. These oxides focused on the coupling of two metal elements amongst lanthanum, cerium, copper, nickel, cobalt, which can be generally categorized into two groups: cerium- and lanthanum-containing mixed oxides. Moreover, an attempt to obtain La-Fe oxide was also made, by using the evaporation method (EM). Mixed metal oxides with the molar ratio of the two metal elements being 1:1, 1:2, and 2:1 were prepared. TG-DSC, $N_2$ adsorption, XRD and TPR were utilized to characterise the obtained materials. Synthesized oxides were tested on the catalytic oxidation of ethyl acetate.

### 2.2.1. Synthesis of Catalysts

Exotemplating (EX) [13, 24, 45] and evaporation (EM) [15] are the two primary methods employed in the synthesis of the mixed-oxide catalysts. A glycine-nitrate process (GNP) [38] was also adopted for the synthesis of perovskite-type materials. Also a combination of glycine-nitrate process and exotemplating method, named GN-EX, was exploited for La-Co preparation with intention in surface area improvement.

2.2.1.1. Exotemplating Method (EX)

The exotemplating method applied in preparing mixed oxides was similar to that described above in Section 2.1.1 for single-oxide synthesis: impregnation of the carbon template was carried out with the nitrate precursor; however, instead of a saturated solution of the single metal oxide, a 2 M aqueous solutions of the different metal precursors, previously mixed, were used. All impregnations involved in the synthesis of mixed oxides were based on a Spv-ratio equal to 1.5, being CX with particle size (*D*) between 0.05 mm and 0.25 mm chosen as the templating material. Therefore, the 3.4 ml of the precursor solution was a mixture of two different metal precursor solutions, with selected volumetric proportions, in order to achieve the desired molar ratio of metal elements in the material (1:1, 1:2, or 2:1). For comparison, a different xerogel (CXN), made by the IAESTE student Thanakrit Thavorn-amornsri [52], with larger mesopore size (31.3 nm for CXN [52], instead of 24.4 nm for CX [24]), was also used as templating material. The excess solution was removed only by sandwiching the solid phase between two sheets of filter paper and squeezing gently, since filtration was found to possibly cause a variation in the impregnated amount of precursor, as explained in Appendix 2. Filtration was used in the preparation of Ce-Ni CX4 as this material was made to study the effect of preliminary drying. More detailed information on the sample prepation procedures of these Ce-Ni oxides can be found in Appendix 2.
The temperature programs used in the calcination of mixed oxides are listed in Table 3. These temperatures were chosen based on the TG/DSC results, as explained in Section 3.1.1.1.

Table 3: Temperature programs used for exotemplated mixed oxides.

| Metal oxides | Heating rate (ºC/min) | Intermediate *T* (ºC) | Final *T* (ºC) |
|---|---|---|---|
| Ce-Cu | 2 | 200 | 350 |
| Ce-Ni | 2 | 200 | 400 |
| Ce-Co | 2 | 200 | 350 |
| La-Cu | 2 | 220 | 350 |
| La-Co | 2 | 200 | 350 |

2.2.1.2. Evaporation Method (EM)

In the evaporation method, 2 M ethanol solutions of two metal precursors were mixed together with a predefined volumetric proportion. Then oxalic acid was added, maintaining the molar ratio of oxalic acid/total amount of metal cations in the solution at 1. For the evaporation of solvent, the mixture was heated up to 60 ºC under stirring until only solid oxalate was left. The resulting material was further dried in an oven, at about 80 ºC overnight, and then calcined in a furnace at 300 ºC or 600 ºC for 2 h (or 800 ºC for 1 h), under 100 $cm^3$/min of air flow, with a heating rate of 10 $^oC$/min. If not specified, EM samples were calcined at 300 $^oC$.

A test for synthesizing the La-Fe 1:1 sample was carried out by this method. Additionally, through random selection, a La-Ni 1:1 and a La-Co 1:2 samples were prepared by evaporation at 80 ºC, for comparision.

2.2.1.3. Glycine-Nitrate Method (GNP)

The glycine-nitrate method was used in order to obtain pervoskite-type materials with structure $ABO_3$. Glycine was added to a mixture of equal amounts of the two aqueous metal nitrate precursor solutions (2 M each). The molar ratio of glycine/total amount of metal cations in the solution was kept as 1. The mixture was then gradually heated up until ignition. The resulting black powder was then calcined under 100 $cm^3$/min of air flow, with a heating rate of 10 $^oC$/min, for the further decomposition of the small portion of residual metal complex. Three calcination temperatures were used: 350 $^oC$, 600 $^oC$ and 800 $^oC$.

2.2.1.4. GN-EX Method

A combination of the glycine-nitrate process and the exotemplating method was tested, in the attempted synthesis of a perovskite-type La-Co material with large surface area. In this procedure, the simple mixture of solutions of the two nitrate precursors, used in exotemplating method, was replaced by the mixture of nitrate precursors and glycine as in the glycine-nitrate process. Calcinations were carried out at an intermediate temperature of 200 $^oC$, and then further heated up to the desired end temperature:

350 $^{o}$C, 600 $^{o}$C or 800 $^{o}$C, with a heating rate of 10 $^{o}$C/min, under 100 cm$^3$/min of air flow.

### 2.2.2. Material Characterizations

Material characterizations were carried out by TG-DSC, $N_2$ adsorption and TPR. Selected samples were also analyzed by XRD. The conditions used for characterisation of these materials were the same as those described in detail in Section 2.1.2 for the single oxides.

### 2.2.3. Catalytic Performance Tests

The synthesized materials were tested as catalysts on the oxidation of ethyl acetate on the VOC set-up, with the same settings as described in Section 2.1.3. A series of selected samples were also tested for the oxidation of toluene. These results will be discussed in Section 3.3.

## 3. Results and Discussion

### 3.1. Single Metal Oxides

The characterization results and catalytic performances of exotemplated single metal oxides and gold nanoparticle doped samples are included in this Section, along with those of the commercial supports (CuO from Riedel-de Haën, NiO from Aldrich and $Fe_2O_3$ from Sigma-Aldrich).

### 3.1.1. Material Characterizations

#### 3.1.1.1. TG-DSC

As said above, this technique allowed the determination of the adequate temperature of calcination for the different oxides, and also the verification of the presence of residual carbon template in the samples after calcination.

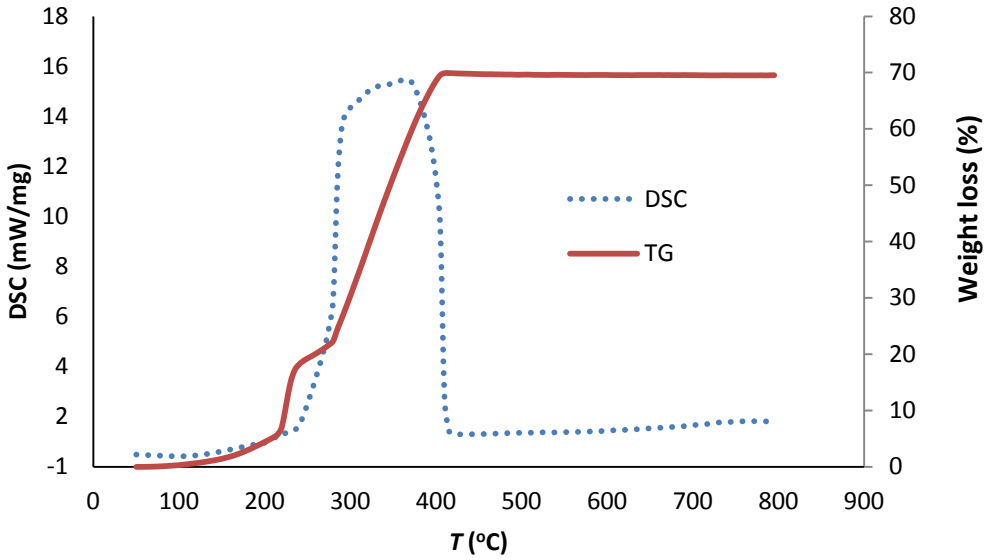


Figure 13: TG-DSC of CX (D<0.1mm) impregnated with a saturated solution of copper nitrate.

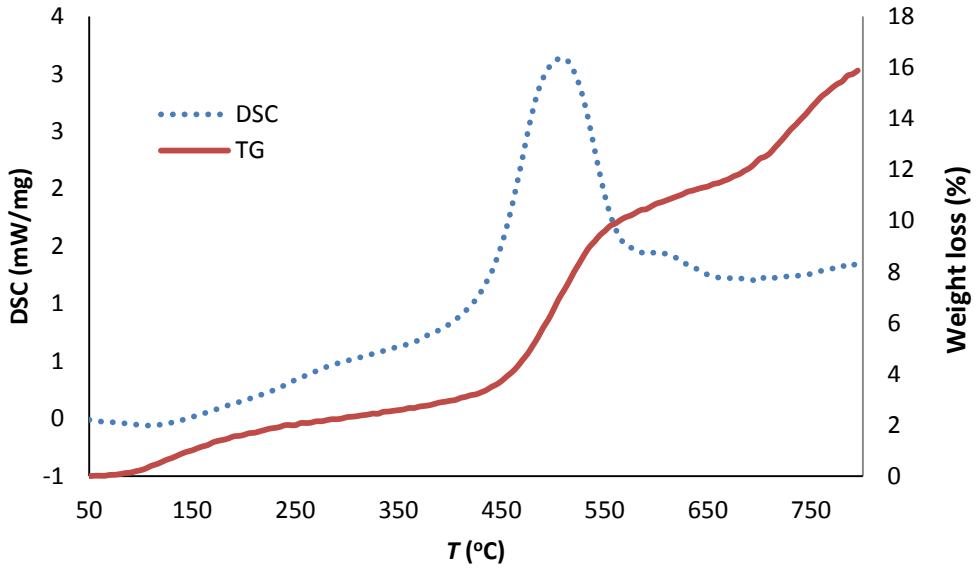


Figure 14: TG-DSC of CROX templated nickel oxide after (insufficient) calcination.

As an example, Figure 13 shows the TG-DSC profile of CX (D<0.1mm) exotemplated CuO before calcination. The amount of energy released reached a maximum at about 350 °C as can be seen in the DSC curve. Therefore, the calcination temperature of 350 °C was chosen for CuO CX. A shoulder appeared in the TG curve at around 250 °C, corresponding to the primary transformation of copper nitrate into copper oxide, so

this temperature was set to be the intermediate temperature in calcination, in order to allow the formation of the oxide (at a lower temperature), before calcination of the template (at a higher temperature).

TG-DSC could also determine whether residual carbon was present or not in already calcined samples. Figure 14 shows a case where more calcination was needed as still a weight loss of about 16% was found for this sample, with a peak present in the DSC curve.

### 3.1.1.2. BET Surface Area

The BET surface area of materials used as exotemplates was 944 $m^2/g$ for CROX, which is larger than that of CX (633 $m^2/g$) [24]. The values obtained for the exotemplated oxides are shown in Table 4.

Table 4: BET surface areas of the exotemplated samples obtained by adsorption of $N_2$ and crystallite sizes and phases detected by XRD.

| **Metal oxide samples** | **BET area ($m^2/g$)** | **Phase detected** | **Crystallite size (nm)** |
|---|---|---|---|
| Commercial CuO [*] | 11 | CuO (tenorite) | 25 |
| CuO CX D<0.1mm | 34 | CuO (tenorite) | 26 ± 5 |
| CuO CX 0.05mm<D<0.25mm | 12 | CuO (tenorite) | 26 ± 5 |
| CuO CROX | 24 | CuO (tenorite)[c] | 28 |
| Commercial NiO [a] | 81 | NiO (cubic) | 26 [*] |
| NiO CX | 96 | NiO (cubic) | 12 |
| NiO CROX | 81 | NiO (cubic)[c] | 9 |
| Commercial $Fe_2O_3$ [b] | 6 | $Fe_2O_3$ (hematite) | 63 |
| $Fe_2O_3$ CX | 63 | $Fe_2O_3$ (hematite) 74.52 vol.%<br>$Fe_3O_4$ (magnetite) 25.48 vol.% | 39<br>20 |
| $Fe_2O_3$ CROX | 115 | Too much amorphous | - |

[a] - Results from [53]; [b] - Results from [50]; [c] – contamination peaks found (most likely due to ashes present on CROX – see text for details)

Iron oxide synthesized with the CROX template had the highest BET surface area (Table 4), which is more than 19 times larger than that of the commercial sample (6 $m^2$/g). A smaller BET surface area (63 $m^2$/g) was obtained with CX exotemplated iron oxide. The use of CROX did not improve the BET surface area in the case of nickel oxide. However, the use of CX led to an increase of 15 $m^2$/g, compared to the commercial sample. All copper samples had smaller BET surface areas than the iron and nickel oxides prepared in this work. Using CROX and CX with dimension less than 0.1 mm as templates raised the BET values of the exotemplated oxides to about double and triple of the value 11 $m^2$/g of the commercial CuO.

3.1.1.3. XRD

This technique provided information on sample composition and the volume percentage of each constituent. It also allowed the determination of the particle sizes of each sample components. Table 4 shows the phases obtained and the corresponding particle sizes for selected samples. The XRD spectra of metal oxides, with Miller Indices identified, are shown in Figures 15 to 17. Exotemplating methods led to metal oxides with the same structures as the respective commercial oxides, except for the case of iron oxide, where 25.5 vol. % of $Fe_3O_4$ (magnetite) was also present. For nickel and iron oxides, samples with smaller particle sizes were obtained by templating with CX whereas copper oxides showed particle sizes similar to those of the commercial samples. For CROX samples, some minor contamination peaks were identified in the copper and nickel samples (Figures 15 and 16 and Table 4) and a very amorphous XRD spectrum was obtained for iron oxides (Figure 17). A possible explanation for this can be related with the fact that CROX material contains ~3.6% of ashes, as determined by TG/DSC in a previous study [54]. Energy-dispersive X-ray spectroscopy (EDS) analysis of the ashes showed the presence of O (48.8 wt.%), Si (22.0 wt.%) and S (8.5 wt.%). Smaller amounts of Ca, Al, Mg, Na, Fe (3–5 wt.% each) and P, K, Ti (0.6–1.4 wt.% each) were also detected.

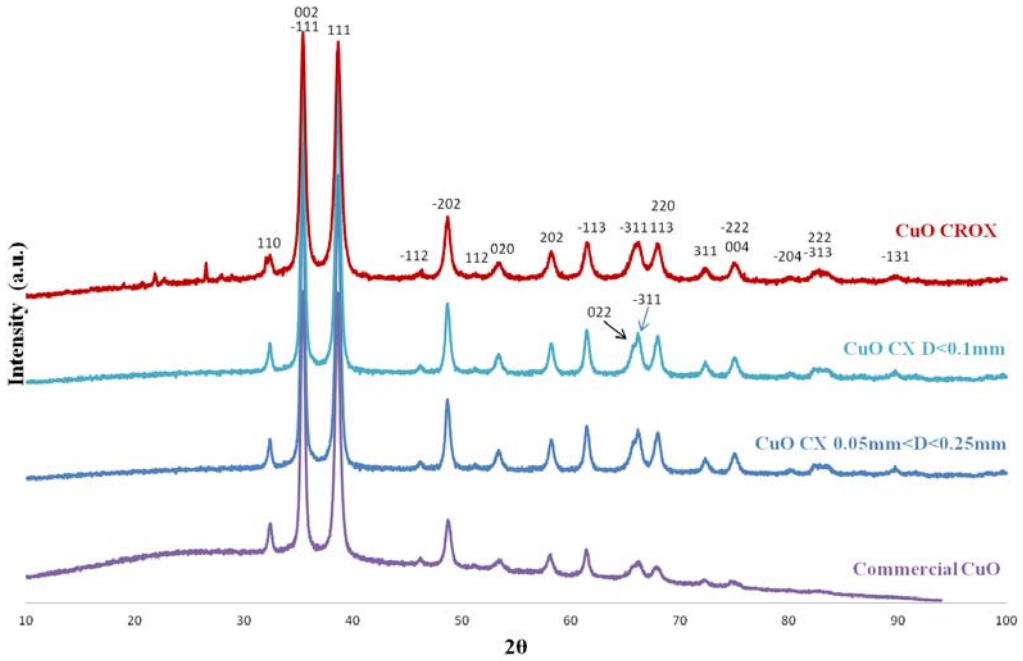


Figure 15: XRD spectra of commercial, CX and CROX templated copper oxides. Miller Indices from AMCSD 0011639.

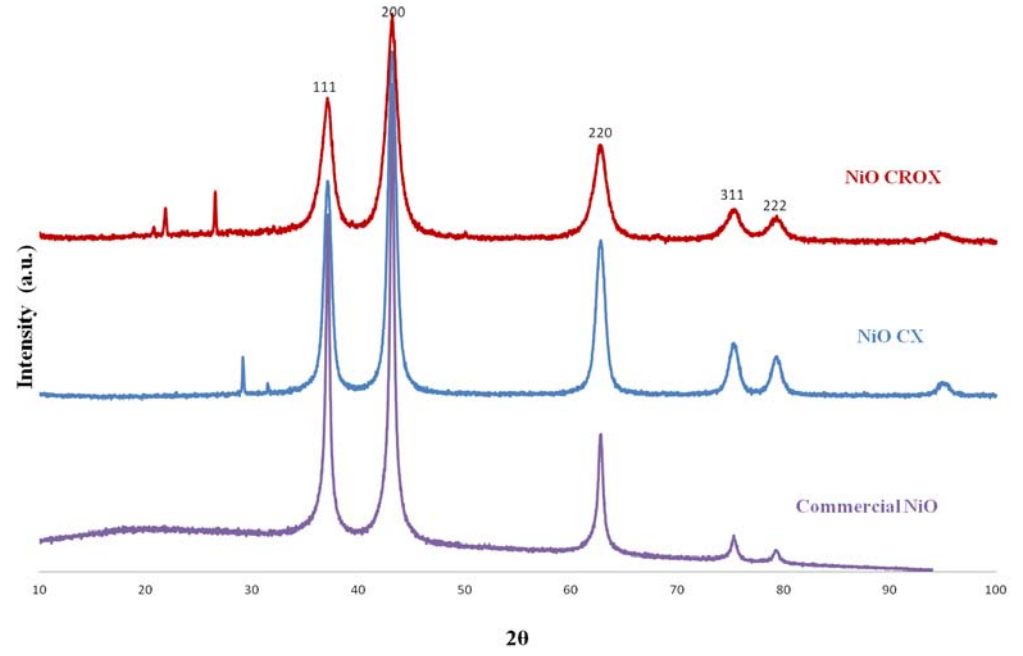


Figure 16: XRD spectra of commercial, and CX and CROX templated nickel oxides. Miller Indices from AMCSD 0017028.

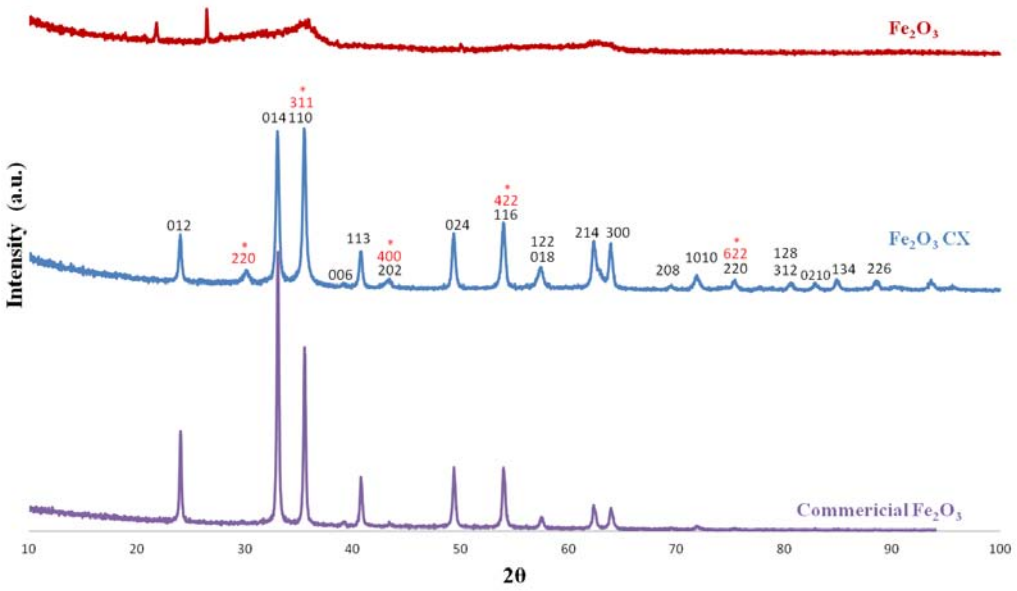


Figure 17: XRD spectra of commercial, and CX and CROX templated iron oxides. Miller Indices from AMCSD 0000143 for hematite (black) and AMCSD 0007824 for magnetite (red, marked with *).

### 3.1.1.4. TPR

This technique allowed the determination of the reduction profiles of samples prepared with different templates. The TPR spectra of commercial metal oxides and gold loaded samples (data adapted from [50, 53]) are also presented for comparison.

Figure 18 shows the TPR profile of copper samples. It can be observed that the whole curve of gold loaded CuO was shifted about 10 $^{o}$C to a lower temperature range, however, still following the same tendency, in general, as that of the commercial oxide. CuO template with CX $D$<0.1mm has the first reduction peak appearing at a much lower temperature than that of the commercial sample and gold loaded sample, whereas CuO CX 0.05mm<$D$<0.25mm and CuO CROX failed in lowering the reduction temperature of copper oxide. This might be ascribed to the larger BET surface area obtained for the $D$<0.1mm template material, since a higher CuO surface area means a higher reducibility of CuO, due to the decrease of crystallite size [55]. A shoulder on the peak of the commercial CuO TPR spectrum appeared at 256 $^{o}$C. Also a shoulder can be observed in the profile of CuO CROX at lower temperature, before the highest reduction peak. However, only one saturated peak was seen in both CX exotemplated

cases. This is probably because the temperatures at which changes between oxidation states ($CuO \rightarrow Cu_2O \rightarrow Cu$) occurred were very adjacent to each other, so that they appeared as one single peak in the reduction profile.

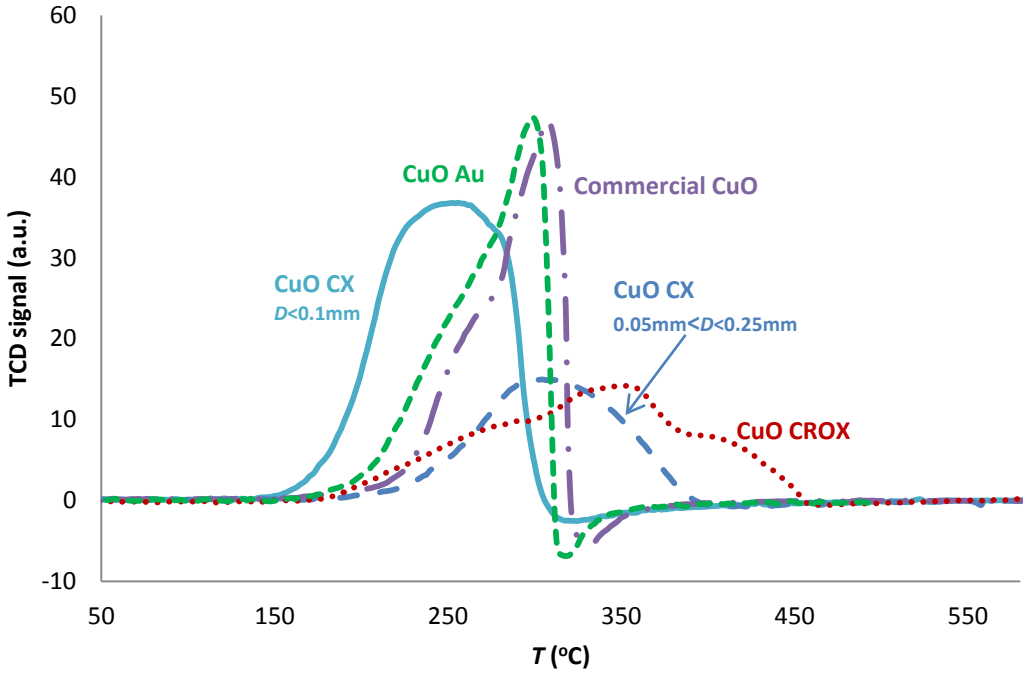


Figure 18: TPR of commercial, gold loaded, and CROX and CX ($D$<0.1mm and 0.05mm<$D$<0.25mm) exotemplated copper oxides.

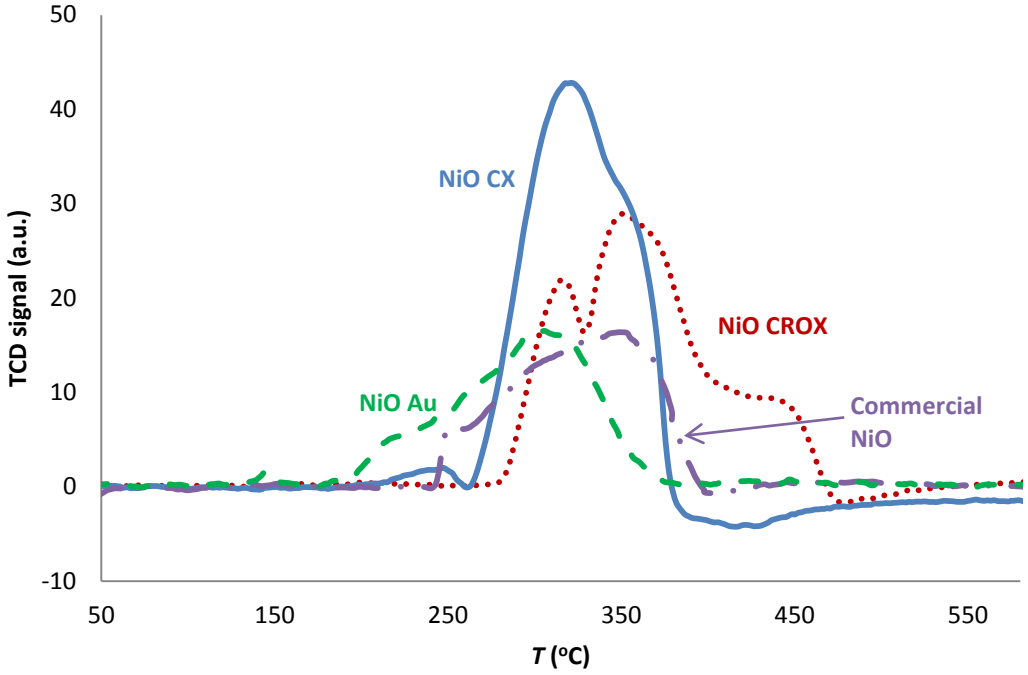


Figure 19: TPR of commercial, gold loaded, and CROX and CX exotemplated nickel oxides.

A similar tendency can be found in the TPR spectra of nickel oxides (Figure 19). Using CX as template can shift the temperature required for reduction towards lower values. For commercial oxide, the main peak appeared at approximately 343 $^{o}$C, with a shoulder at around 250 $^{o}$C. These were decreased to 315 $^{o}$C and 243 $^{o}$C, respectively, for the NiO CX sample, where the shoulder was separated from the main peak forming a single small feature. This small peak, just like the shoulder in the commercial sample, could be attributed to the reduction of surface oxygen, as large surface areas were found in NiO samples, so more oxygen could be bound to the material surface. A new shoulder appeared on the main peak at about 348 $^{o}$C, which did not appear in the commercial sample. This might mean that the two-step reduction ($Ni_2O \rightarrow NiO \rightarrow Ni$) formed a joint peak in the commercial oxide, but two peaks in the CX templated material. For both copper and nickel oxides, the reduction peaks of CROX templated samples were shifted to higher values. These may be due to the ash content of the CROX template material, which might also be responsible for the occurrence of shoulders in the main peaks of the respective spectra. However, in this case, the gold loaded sample had the best reducibility, as its main reduction peak appeared at the lowest temperature among all materials, that is, around 303 $^{o}$C, and the shoulder was shifted by about 30 $^{o}$C to lower values. It is expected on the basis of literature that the presence of a metal, such as gold, has such an effect [15, 16, 53].

Lower reduction temperatures were found for the CX templated iron oxide sample (Figure 20). However, the two peaks found at higher temperatures, after the main peak, were no longer present in $Fe_2O_3$ CX. As determined in literature, the reduction peak at around 300 $^{o}$C is due to the reduction of the hydroxylated iron oxide species [16, 20, 56-59] and the peak for reduction of hematite ($Fe_2O_3$) to magnetite ($Fe_3O_4$) appears at about 400 $^{o}$C [16, 20, 56-61]. The reduction of $Fe_3O_4$ to FeO (wüstite) results in a peak at approximately 600 $^{o}$C [16, 56, 57, 60, 62] and the final transformation to metallic iron occurs above 800 $^{o}$C [57]; however, overlapping cases of the last two peaks were reported as well [50, 57, 61]. The two peaks shown after 800 $^{o}$C in the TPR spectrum of the commercial sample (Figure 20) indicate that the reduction of $Fe_3O_4$ to FeO (or of FeO to Fe) may possibly occur in two stages [50]. In $Fe_2O_3$ CX, only two reduction steps can be observed: the peak at 348 $^{o}$C can be the reduction of hematite ($Fe_2O_3$) to magnetite ($Fe_3O_4$) as an increase in surface area can shift its position to a lower temperature [57-59], and the reduction of $Fe_3O_4$ to FeO

(wüstite) and further to Fe, maybe overlap at about 552 °C. The low intensity of the first reduction peak in CX templated sample can be attributed to the presence of $Fe_3O_4$, which accounted for 25 vol. % of the sample (Table 4). However, it seems that the larger BET surface area of the CROX templated sample did not shift the starting point of the reduction ($Fe_2O_3 \rightarrow Fe_3O_4$) to a lower temperature. Yet, the transition from $Fe_3O_4$ to metallic Fe appeared at a lower temperature (670 °C) in $Fe_2O_3$ CROX, with a shoulder appearing at 550 °C. In the case of gold-loaded sample, although the set-on temperature of the first reduction peak appeared 30 °C lower than that of the CX templated material, the occurrence of first reduction was 10 °C delayed after $Fe_2O_3$ CX.

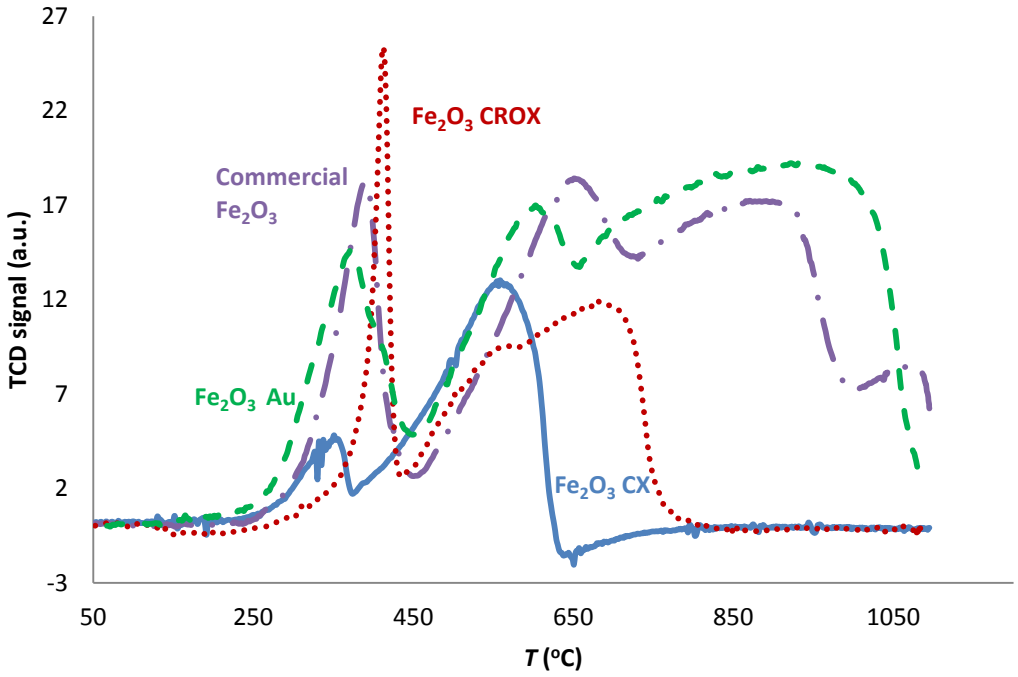


Figure 20: TPR of commercial, gold loaded, and CROX and CX exotemplated iron oxides.

### 3.1.1.5. HRTEM

The HRTEM images of gold loaded copper, iron and nickel oxides are shown in Figures 21 to 23. Gold nanoparticles can be seen as darker spots in copper and iron samples, but can hardly be identified in the nickel sample. This could be attributed to the presence of carbon on the support as ~2.9% of “free carbon” was detected in this material by energy-dispersive X-ray spectroscopy (EDXS) and 2.5% carbon was found

by thermogravimetry in a previous study [53]. The information on the sizes of the doped gold nanoparticles are listed in Table 5.

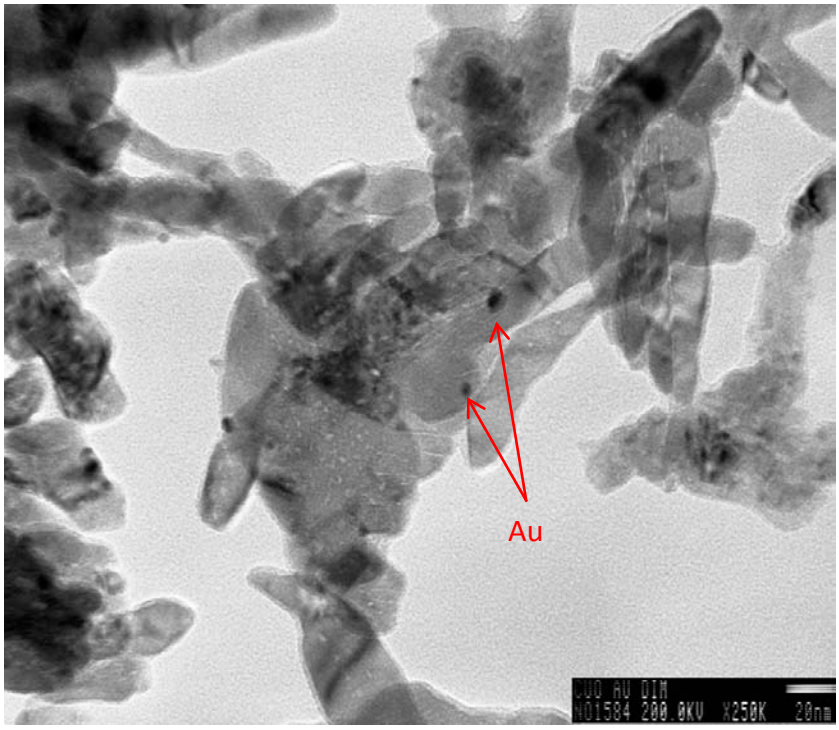


Figure 21: HRTEM image of CuO with Au loaded by DIM.


Figure 22: HRTEM image of $Fe_2O_3$ with Au loaded by DIM.

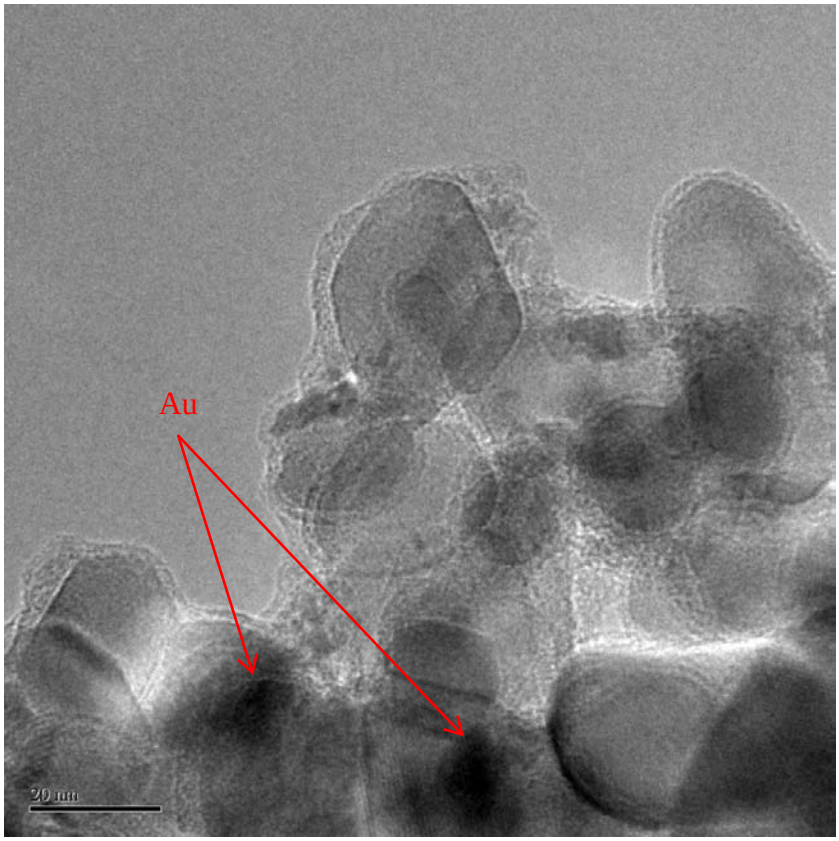


Figure 23: HRTEM image of NiO with Au loaded by DIM.

Table 5: Gold nanoparticle size range and average (determined by HRTEM) for gold loaded samples.

| Au/oxide | Gold particle size range (nm) | Average gold particle size (nm) |
|---|---|---|
| Au/CuO * | 2–12 | 5.8 |
| Au/$Fe_2O_3$ ** | 4–20 | 11.8 |
| Au/NiO * | 2–8 | 4.8 |

* - Results from [53]; ** - Results from [50]

### 3.1.2. Catalytic Performance Tests

The catalytic performances of gold nanoparticle doped samples are shown in Section 3.1.2.1, together with the catalytic activities of commercial oxides for comparison. The catalytic results of the exotemplated samples, as well as the comparisons with gold laded and commercial samples will be presented in Section 3.1.2.2.

3.1.2.1. Au/Commercial Metal Oxides

Figures 24 and 25 exhibit the catalytic results, obtained with two cycles of increasing and decreasing temperature, for gold loaded copper and nickel oxides, respectively. It can be observed, in both Figures, that the first increasing step occurred at a temperature lower than that of the respective remaining three steps. This can be related to the partial deactivation of active sites of gold nanoparticles as it is well known that they are very sensitive to temperature increase [7]. Therefore, in the following comparison of catalytic activities, the first increasing steps of these samples are excluded, and only the stabilized phases in the remaining three steps are used.

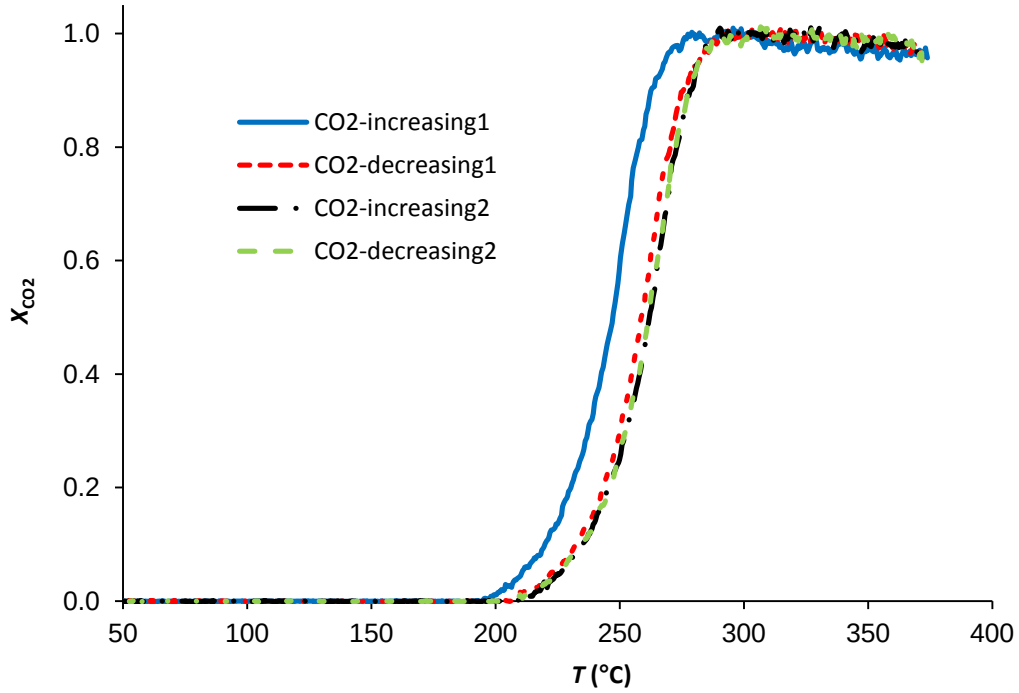


Figure 24: Catalytic performance of gold doped copper oxide (two cycles of increasing and decreasing temperature are shown).

The catalytic performance of copper oxide was improved by doping with gold nanoparticles, as shown in Figure 26. The same tendency can be found in gold loaded nickel oxide (Figure 27). However, in this case, although full decomposition of ethyl acetate was achieved, about 10 ppm of CO was detected whereas gold-loaded copper oxides showed good activity and selectivity for the catalytic oxidation of ethyl acetate without CO formation. Gold loaded CuO lowered the temperature required for 100% conversion of ethyl acetate to $CO_2$ and $H_2O$ down to 289 $^oC$ while the complete conversion catalyzed by commercial CuO was reached at 309 $^oC$.

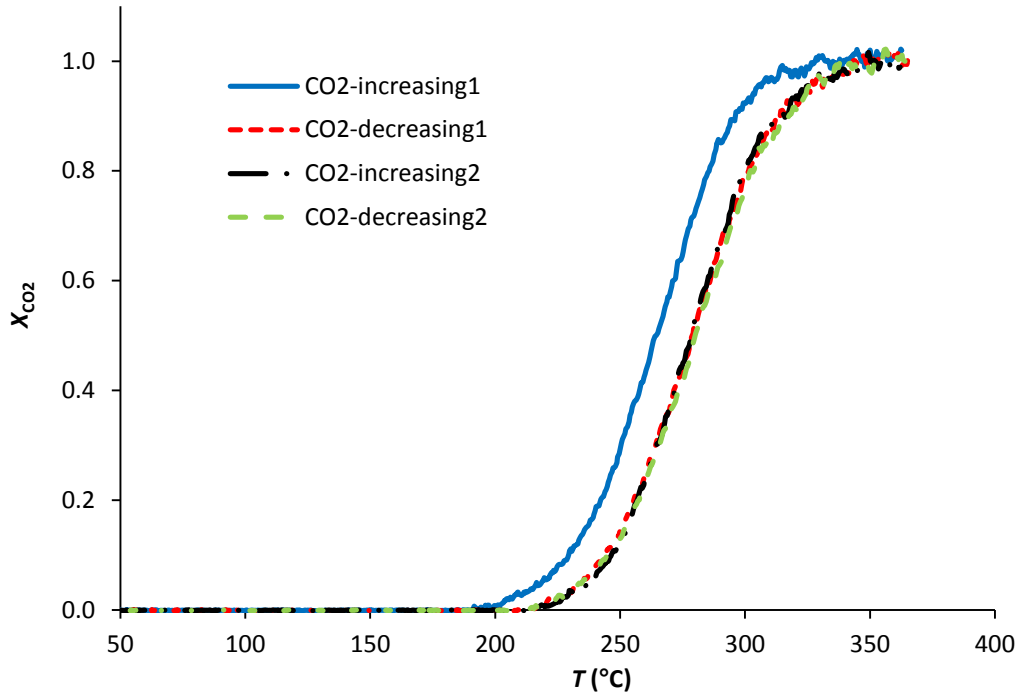


Figure 25: Catalytic performance of gold doped nickel oxide (two cycles of increasing and decreasing temperature are shown).

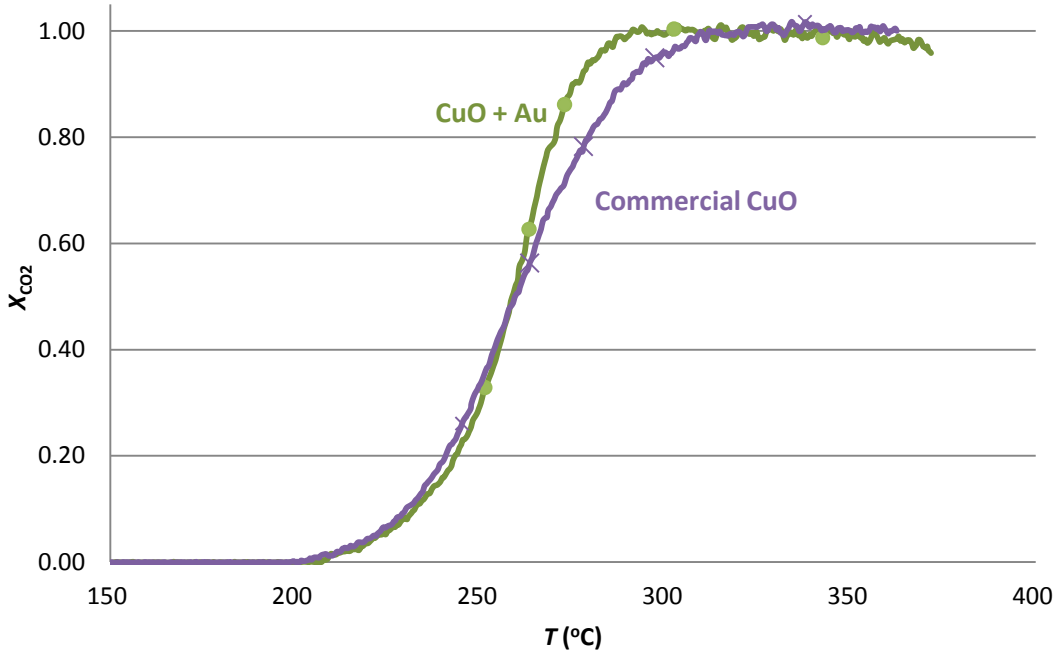


Figure 26: Catalytic performance of commercial copper oxide alone or loaded with gold.

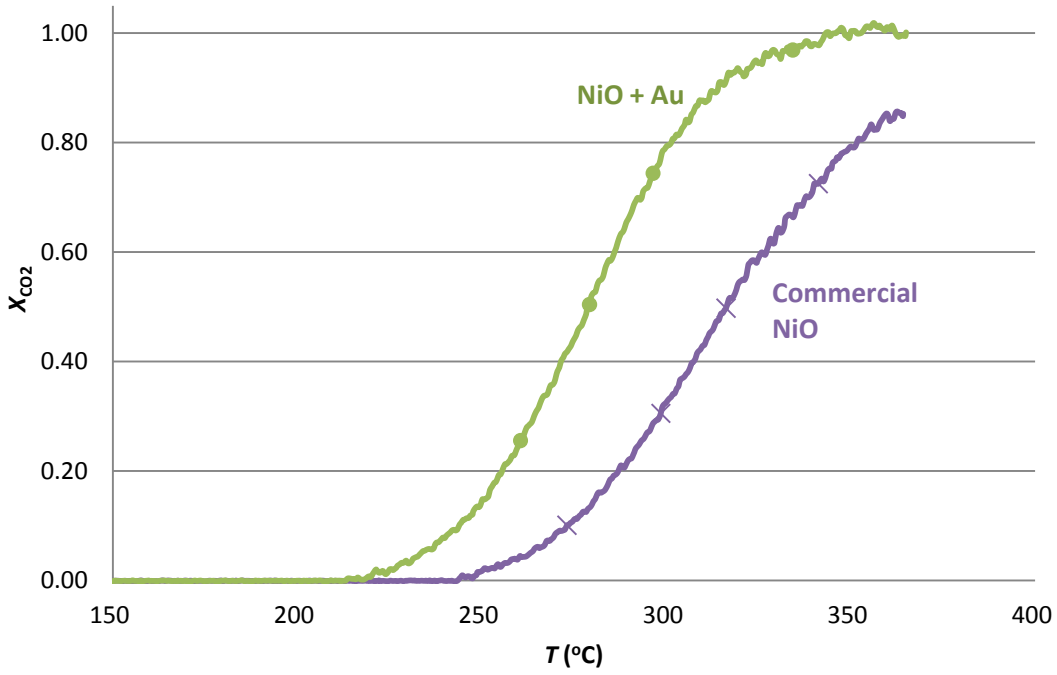


Figure 27: Catalytic performance of commercial nickel oxide alone or loaded with gold.

The phenomenon of partial deactivation of catalyst was not observed for the gold loaded iron oxide (Figure 28). However, this material did not show any improvement in the catalytic activity when compared to the respective commercial sample. The maximum conversion achieved with this sample was 92%, as presented in Figure 29. The catalytic activities of gold loaded samples are possibly related to the particle size of the doped gold nanoparticle. For copper and nickel samples, the average size of the gold particles were 5.8 nm and 4.8 nm respectively [53], corresponding to improvements over the commercial oxides, while 11.8 nm was found for gold loaded on the iron sample [50]. It is known from literature that smaller gold nanoparticles show better performance in catalytic reactions [15, 53], which might be the reason for the lower activity shown by the iron containing sample in the oxidation of ethyl acetate. The catalytic activity of the nickel oxide was promoted upon gold doping, yet it did not give good $CO_2$ selectivity to this material. This might be due to the presence of free carbon in the support material; although carbon in the nickel oxide was found to be a promoter in CO oxidation [53], it may hinder the catalytic activity of this sample for VOC oxidation.

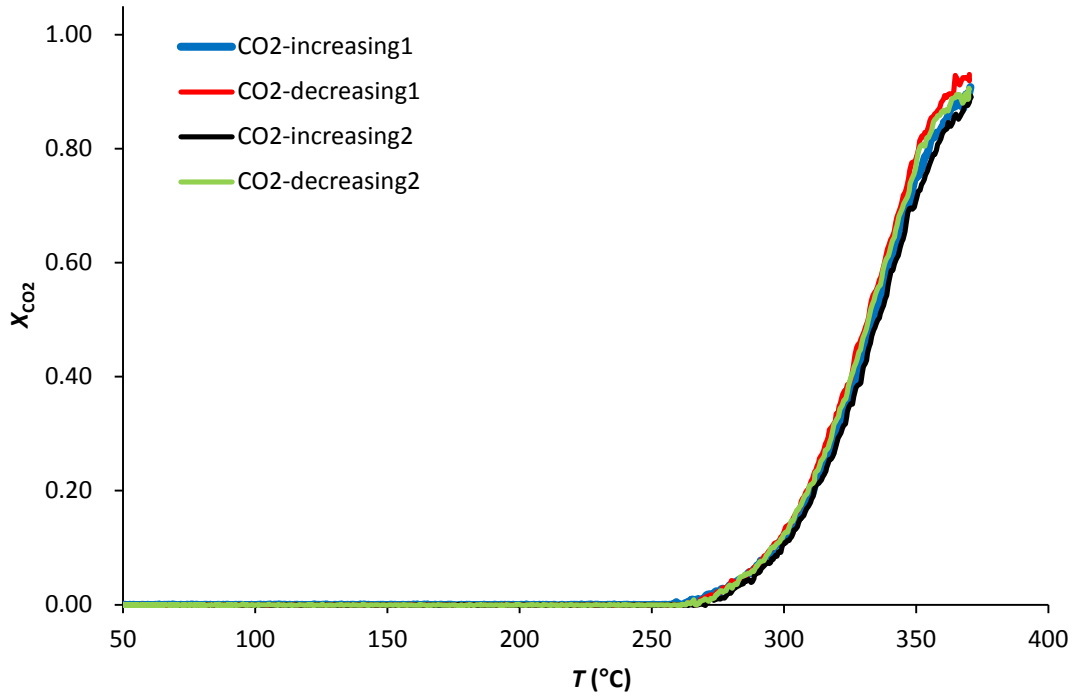


Figure 28: Catalytic performance of gold doped iron oxide (two cycles of increasing and decreasing temperature are shown).

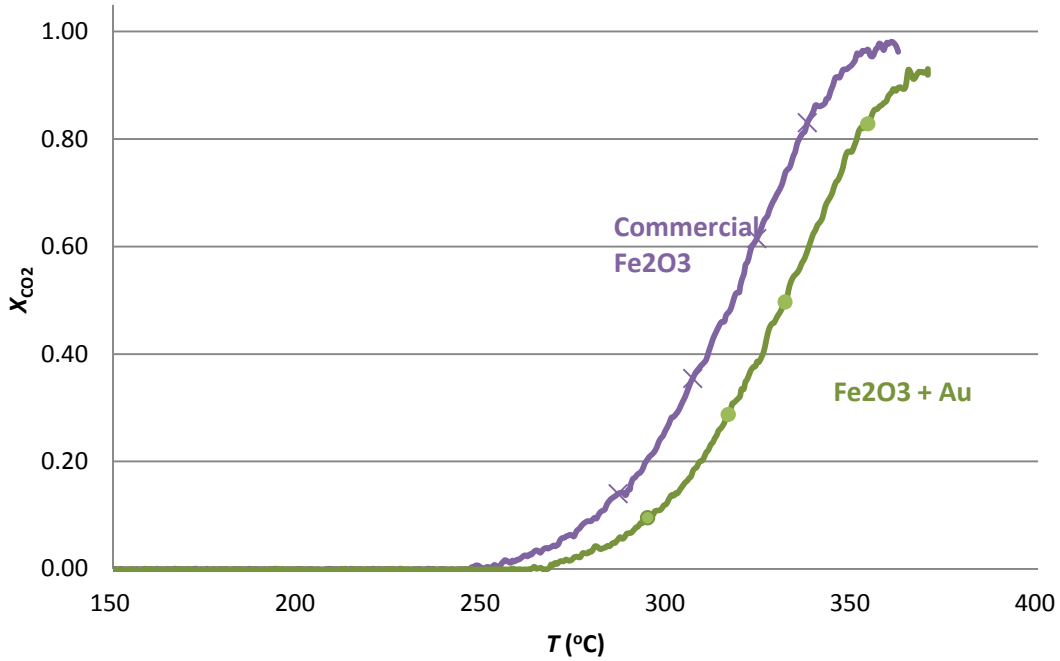


Figure 29: Catalytic performance of commercial iron oxide alone and doped with gold.

The not so good results obtained with MgO, $La_2O_3$ and $Y_2O_3$, alone or doped with gold, are shown in Appendix 1.

### 3.1.2.2. Exotemplated Metal Oxides

No significant variations were found between the two cycles of increasing and decreasing temperature of the catalytic experiments of all exotemplated samples. Therefore, only the comparisons of catalytic activities are shown in this Section. Further information on these cycles can be found in Appendix 1.

The experimental results dealing with the catalytic oxidation of ethyl acetate using copper oxides are shown in Figure 30. All CX templated samples were very active, whereas only about 90% conversion of ethyl acetate to $CO_2$ was achieved by CuO CROX. CX 0.05mm< *D*<0.25mm did not lead to a more active copper oxide, when compared to the commercial sample, and traces of CO were detected at maximum conversion. But significant improvement was attained by CuO CX *D*<0.1 mm, without any CO formation, the maximum conversion being reached at 280 °C, which was 10 °C lower than that of the gold loaded commercial copper oxide. The reason for this may be attributed to the larger BET surface area and improved reducibility of the CX *D*<0.1mm templated oxide, compared with those of the commercial and gold loaded CuO and CuO CX 0.05mm< *D*<0.25mm.

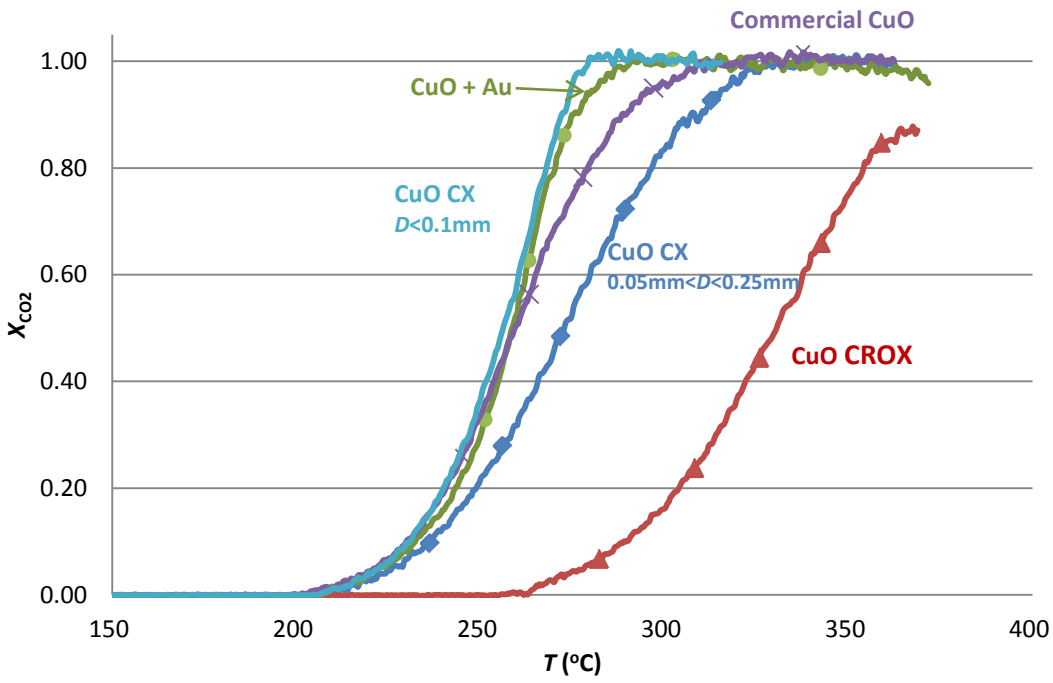


Figure 30: Catalytic performance of copper oxides.

Figure 31 shows the catalytic performance of nickel oxides for the same reaction. Unlike commercial CuO, the commercial NiO sample did not catalyze the oxidation reaction to 100% conversion. However, by using the CX templated material, complete conversion into $CO_2$ was achieved at 330 $^{o}$C. In the case of iron oxides (Figure 32), there was some improvement by using CX as template, probably due to the presence of the $Fe_3O_4$ phase, yet this sample was not as selective as the CX templated CuO and NiO. CROX templated oxides showed the lowest activities of all three metal oxides, although $Fe_2O_3$ CROX had the largest BET surface area among all samples. This again could be attributed to the impurities contained in the CROX carbon material, as explained above, which possibly hindered the functioning of active sites on the metal catalysts. On the contrary, CX has no ashes and is a more suitable templating material. The presence of both mesopore and micropore systems in CX [52] makes it even more valuable for applications in catalysis both as template or support material.

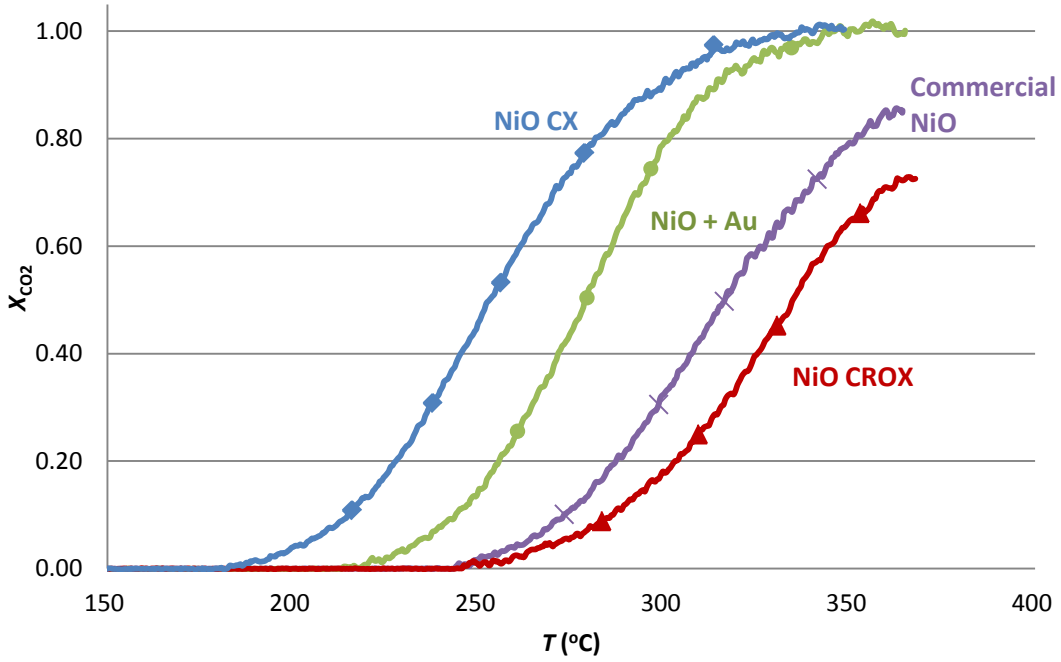


Figure 31: Catalytic performance of nickel oxides.

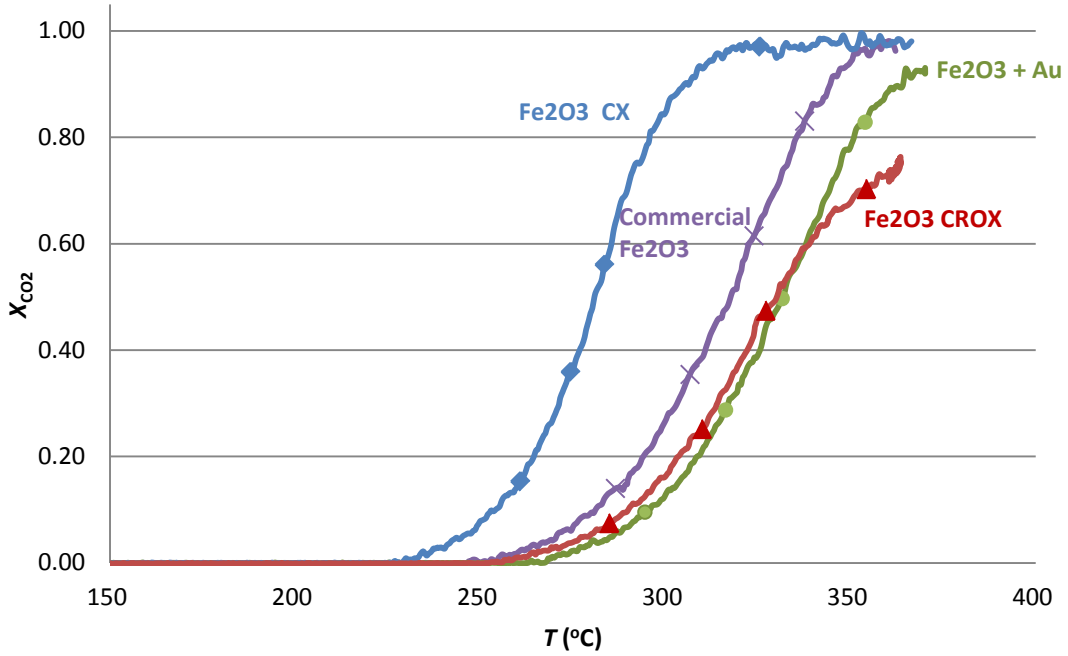


Figure 32: Catalytic performance of iron oxides.

### 3.1.3. Conclusions

The highest BET surface area was observed for the iron oxide prepared with CROX. However, due to the ash content of CROX, this sample did not show any attractive properties or activity as a catalyst. For copper and nickel oxide, larger surface area materials were achieved by using CX template, with reducibility shifted to lower temperatures. The same phases present in the respective commercial oxides were obtained with the exotemplating method, with the exception of the CX templated iron oxide, where magnetite ($Fe_3O_4$) was also detected by XRD.

In the catalytic experiments of gold loaded samples, catalytic activities for the oxidation of ethyl acetate of copper and nickel oxides were promoted upon loading with gold. However, the same did not happen with the iron sample. This may be related to the particle size of the gold nanoparticles, which was much larger on the iron oxide than on the other samples (since it is well known that smaller gold nanoparticles lead to improved catalytic materials). The free carbon found in the nickel oxide support might act as an obstruction for the catalytic activity, causing the formation of a small amount of CO. This subject needs further investigation.

For exotemplated metal oxides, enhancements in catalytic performances could be observed for samples prepared with the CX template, whereas CROX samples exhibited the lowest activities. The CX templated samples showed better catalytic results than the commercial and gold loaded samples. Therefore, CX is a better templating material than CROX. NiO prepared with CX showed large improvement in performance in the catalytic oxidation of ethyl acetate; however, CuO was the best catalyst among all the single oxide samples, full conversion of ethyl acetate to $CO_2$ without CO formation being achieved at 280 $^{o}$C.

## 3.2. Mixed Metal Oxides

The characterisation and catalytic performances on ethyl acetate oxidation of the prepared mixed oxides are presented in this section. Catalytic activities of the selected materials on toluene oxidation will be discussed in Section 3.3.

### 3.2.1. Material Characterizations

#### 3.2.1.1. TG-DSC

Figures 33 and 34 illustrate two examples of TG-DSC curves of mixed oxides. Just like with the single oxides, this technique was applied for the determination of the adequate calcination temperatures and verification of residual carbon for the mixed oxides exotemplated samples.

Figure 33 shows two small shoulders on the TG curve, one at 200 $^{o}$C and the other at around 260 $^{o}$C, corresponding to the primary transformation of cerium and nickel nitrates to oxides. A small separated peak can be seen in the DSC curve at around 200 $^{o}$C. However, at about 260 $^{o}$C, a shoulder appears only on the main peak. Therefore, 200 $^{o}$C was chosen as the intermediate calcination temperature for exotemplated Ce-Ni samples. A temperature of 400 $^{o}$C was selected as the end calcination temperature since the maxima in the DSC curve stretched between about 350 $^{o}$C and 450 $^{o}$C, with 400 $^{o}$C being approximately in the middle.

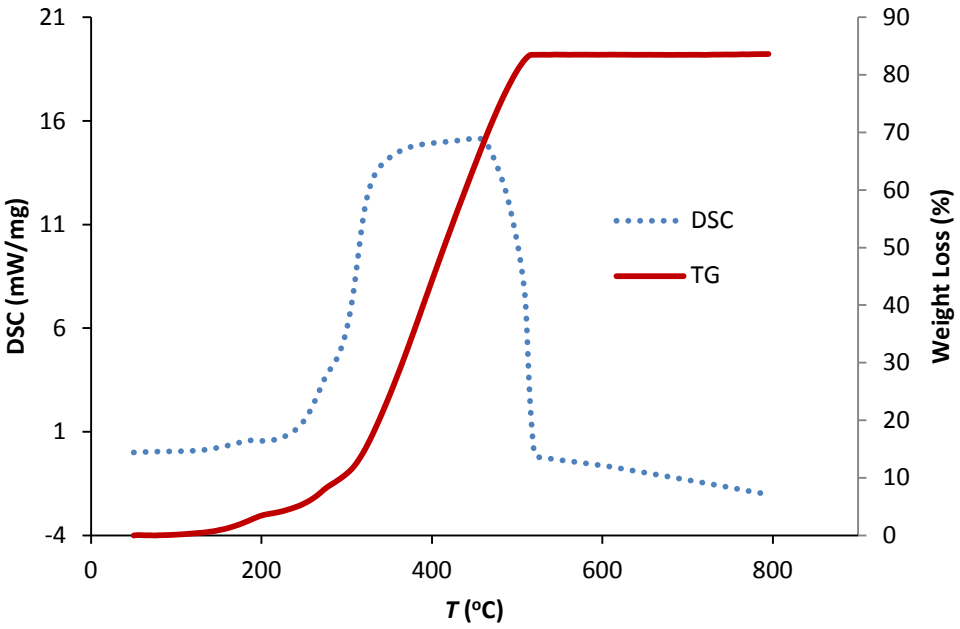


Figure 33: TG-DSC of CX (0.05mm<D<0.25mm) impregnated with a mixture of cerium and nickel nitrate solutions.

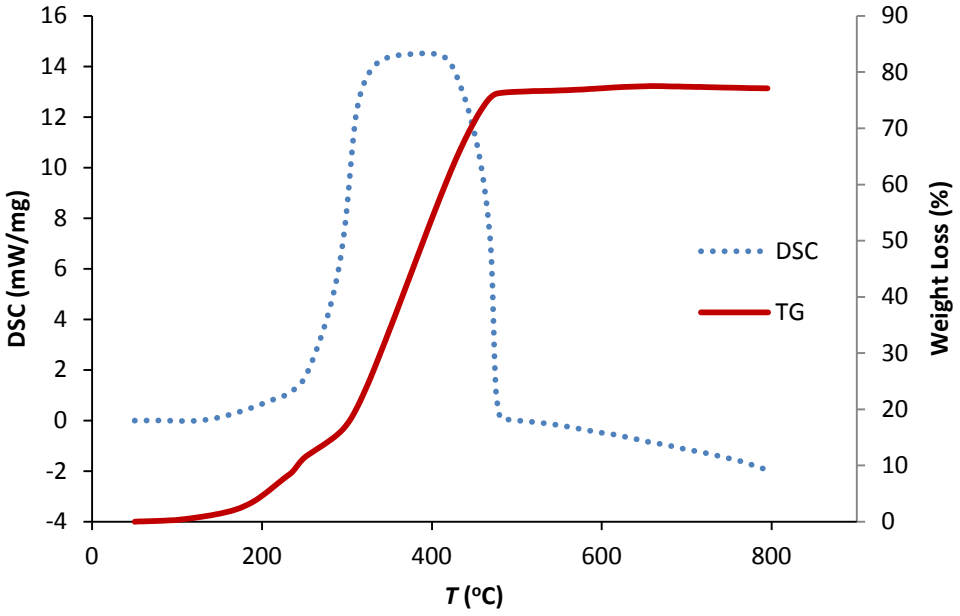


Figure 34: TG-DSC of CX (0.05mm<D<0.25mm) impregnated with a mixture of lathanum and copper nitrate solutions.

Similarly in the case of La-Cu sample shown in Figure 34, 350 $^{o}$C was set as the end calcination temperature. For the intermediate calcination temperature, a shoulder appears at about 250 $^{o}$C in the TG curve; however, no single peak can be observed in the DSC curve. However, at about 220 $^{o}$C, the DSC curve shows a flat feature being a

rising tendency in the TG curve, at the same position. Consequently, 220 $^{o}$C was selected as the intermediate calcination temperature.

#### 3.2.1.2. BET Surface Area

All synthesized samples were analyzed by $N_2$ adsorption to obtain information on their BET surface area. The results are presented in the following Sections: 3.2.1.2.1 for cerium-containing samples and 3.2.1.2.2 for lanthanum-containing samples.

##### 3.2.1.2.1. Cerium-Containing Mixed Oxides

The BET surface areas of Ce-Cu samples are listed in Table 6. The 1:1 sample showed larger surface area than the corresponding 1:2, prepared by the same method. Larger BET values were obtained by the exotemplating method and both 1:1 and 1:2 samples had better results than the respective materials made by EM. The use of higher calcination temperatures decreased the BET surface area dramatically, from 95 $m^2$/g to 3 $m^2$/g (calcined at 600 $^{o}$C) and to 15 $m^2$/g (calcined at 800 $^{o}$C).

Table 6: BET surface areas of Ce-Cu samples.

| **Metal oxide samples** | **BET surface area ($m^2$/g)** |
|---|---|
| Ce-Cu CX 1:1 | 106 |
| Ce-Cu CX 1:2 | 93 |
| Ce-Cu EM 1:1 | 95 |
| Ce-Cu EM 1:1 600C | 3 |
| Ce-Cu EM 1:1 800C | 15 |
| Ce-Cu EM 1:2 | 90 |

If not specified, EM samples were calcined at 300 $^{o}$C.

For the Ce-Ni samples listed in Table 7, the highest surface area was achieved with the Ce-Ni 1:2 synthesised by the evaporation method. Unlike in Ce-Cu materials, the 1:2 sample showed the highest surface area value, so again the 2:1 had better result than the 1:1. A series of Ce-Ni 1:1 samples were prepared by the exotemplating method in order to study the effect of preliminary drying of the template material on the

impregnation efficiency. These results can be found in Appendix 2. The largest surface area achieved with exotemplated Ce-Ni was 138 $m^2$/g, which was smaller than 145 $m^2$/g obtained in Ce-Ni EM 1:1. Two extra samples prepared by modifying the evaporation method, one with an aqueous solution and the other without addition of oxalic acid, were analyzed for comparison. Both showed much smaller surface areas than those synthesized using the procedure described in literature [45]. The BET surface area of Ce-Ni EM 1:1 (aqueous) was 33 $m^2$/g, and about twice of this value was obtained in Ce-Ni EM 1:1 with no oxalic acid.

Table 7: BET surface areas of the Ce-Ni samples.

| **Metal oxide samples** | **BET surface area ($m^2$/g)** |
|---|---|
| Ce-Ni CX1 1:1 | 124 |
| Ce-Ni CX2 1:1 | 133 |
| Ce-Ni CX3 1:1 | 121 |
| Ce-Ni CX4 1:1 | 111 |
| Ce-Ni CX5 1:1 | 138 |
| Ce-Ni CX6 1:1 | 126 |
| Ce-Ni EM 1:1 | 145 |
| Ce-Ni EM 1:2 | 211 |
| Ce-Ni EM 2:1 | 158 |
| Ce-Ni EM 1:1 (aqeous) | 33 |
| Ce-Ni EM 1:1 (with no oxalic acid) | 67 |

All EM samples were calcined at 300 $^oC$.

For the Ce-Co samples, larger surface areas were obtained using the exotemplating method, CX being a better templating material, as shown in Table 8. For samples prepared by EM, the 1:2 materials showed similar results. A decreasing tendency in the BET surface area can be observed in both 1:1 and 1:2 samples, with increasing calcination temperature.

Table 8: BET surface areas of the Ce-Co samples.

| **Metal oxide samples** | **BET surface area ($m^2/g$)** |
|---|---|
| Ce-Co CX 1:2 | 131 |
| Ce-Co CXN 1:2 | 120 |
| Ce-Co EM 1:1 | 105 |
| Ce-Co EM 1:1 600C | 46 |
| Ce-Co EM 1:1 800C | 15 |
| Ce-Co EM 1:2 | 109 |
| Ce-Co EM 1:2 600C | 43 |
| Ce-Co EM 1:2 800C | 11 |

If not specified, EM samples were calcined at 300 $^oC$.

For cerium-containing samples, EX led to larger surface areas in the Ce-Cu and Ce-Co systems, yet failed with Ce-Ni. 1:2 samples showed larger surface areas than the corresponding 1:1, while reversed cases occurred in the Ce-Cu system. In the case of Ce-Co samples, CX was found to be a better templating material. However, significant high surface area was observed for Ce-Ni EM 1:2.

3.2.1.2.2. Lanthanum-Containing Mixed Oxides

For La-Cu samples, exotemplated materials showed larger surface areas than the oxides prepared by EM. Also the 1:2 samples had larger BET values than the corresponding 1:1, as shown in Table 9. Two samples were prepared by direct calcination of a physical mixture of the grounded raw nitrate precursors, denoted as PC 1:1 and PC 1:2. It can be observed that both EX and EM methods led to materials with improved surface areas, in comparison with PC samples. Unlike the tendency observed in cerium-containing oxides, La-Cu 1:1 calcined at 600 $^oC$ resulting in 5 $m^2/g$ larger surface area than sample obtained at lower temperature while La-Cu 1:1 800C had the lowest BET surface area of the EM group.

As shown in Tables 10 and 11, La-Ni EM 1:1 and La-Co EM 1:2 samples, prepared by evaporation at 80 $^oC$, showed worse results than the corresponding properly-prepared samples following procedures described in literature [45]. In both La-Ni and La-Co

systems, the 1:2 sample showed a surface area almost twice as higher as the value observed for the respective 1:1 material.

Table 9: BET surface areas of the La-Cu samples.

| **Metal oxide samples** | **BET surface area ($m^2/g$)** |
|---|---|
| La-Cu CX 1:1 | 19 |
| La-Cu CX 1:2 | 31 |
| La-Cu CXN 1:2 | 45 |
| La-Cu PC 1:1 | 6 |
| La-Cu PC 1:2 | 9 |
| La-Cu EM 1:1 | 15 |
| La-Cu EM 1:1 600C | 20 |
| La-Cu EM 1:1 800C | 8 |
| La-Cu EM 1:2 | 22 |

If not specified, EM samples were calcined at 300 $^{o}$C.

Table 10: BET surface areas of the La-Ni samples.

| **Metal oxide samples** | **BET surface area ($m^2/g$)** |
|---|---|
| La-Ni EM 1:1 (80 ºC) | 25 |
| La-Ni EM 1:1 | 86 |
| La-Ni EM 1:2 | 147 |

If not specified, EM samples were calcined at 300 $^{o}$C.

The exotemplated La-Co samples had the largest surface areas among all prepared materials, with CX showing better results as a template than CXN, as demonstrated in Table 11. The lowest values were found for GNP samples. However, calcination at 600 $^{o}$C surprisingly improved the BET result by 5 $m^2$/g compared with GNP sample calcined at 300 $^{o}$C. For the EM and GN-EX materials, BET decreased when the calcination temperature was increased from 600 ºC to 800 ºC, as mentioned above in connection with the cerium-containing oxides, with a larger decrease presented in GN-EX samples.

Table 11: BET surface areas of the La-Co samples.

| **Metal oxide samples** | **BET surface area ($m^2/g$)** |
|---|---|
| La-Co CX 1:2 | 98 |
| La-Co CXN 1:2 | 92 |
| La-Co EM 1:1 | 39 |
| La-Co EM 1:1 600C | 28 |
| La-Co EM 1:1 800C | 14 |
| La-Co EM 1:2 | 68 |
| La-Co EM 1:2 (80C) | 58 |
| La-Co GNP 1:1 300C | 7 |
| La-Co GNP 1:1 600C | 12 |
| La-Co GNP 1:1 800C | 8 |
| La-Co GN-EX 1:1 350C | 68 |
| La-Co GN-EX 1:1 600C | 18 |
| La-Co GN-EX 1:1 800C | 10 |

If not specified, EM samples were calcined at 300 $^oC$.

A La-Fe sample was synthesised also by EM. The surface area obtained was 72 $m^2/g$. However, only fresh ethanol precursor of iron could be used, as the iron nitrate precursor in ethanol solution became solid after one night. This could have resulted from the additive cetrimide being employed as a stabilizer in the ethanol (96º for medical usage), used in this work for the preparation of the precursor solution, which possibly underwent some reaction with the iron nitrate. For this reason, no other La-Fe samples were prepared, not even by the exotemplating method, due to the low activity of exotemplated iron samples previously obtained. Further information on the characterization and catalytic performance of the La-Fe sample can be found in Appendix 1.

In La-containing oxides, larger surface area materials were achieved by using the exotemplating method for the La-Cu and La-Co systems. CXN led to larger surface area materials than CX in the La-Cu system but failed in the La-Co system. With both EX and EM methods, the 1:2 samples showed larger BET values. In general, a decreasing trend was found in the BET surface area with temperature increase; yet, different results were obtained for La-Cu EM 1:1 600C and La-Co GNP 1:1 600C. For EM

samples, lower surface areas were obtained by evaporation at 80 $^{o}$C. Materials with lowest surface areas were achieved by GNP. An improvement was observed in combination with the exotemplating method. However, if a higher calcination temperature was used, the improvement was not so pronounced.

In both cerium- and lanthanum-containing systems, EX showed a more compatible profile in copper- and cobalt-containing samples. CX was found to be a better templating material, with the exception of the La-Cu sample. Apart from the Ce-Cu system, the 1:2 samples had larger surface areas than the corresponding 1:1 materials. A reversed tendency of BET results with increasing temperature was observed for the lanthanum-containing system, with the La-Cu EM 1:1 600C and the La-Co GNP 1:1 600C samples. Evaporation at temperatures higher than 60 $^{o}$C, for EM, also had an adverse effect on the BET of the materials. Samples with low surface areas were obtained by GNP, but improvements were found for GN-EX prepared samples.

#### 3.2.1.3. XRD

##### 3.2.1.3.1. Cerium-Containing Mixed Oxides

The phases obtained, compositions by volume percentage and crystallite sizes of selected samples are shown in Table 12. For all selected samples, two separate phases were formed for the cerium and the coupling transition metal. With the exception of exotemplated Ce-Cu, the grain sizes of CuO and NiO crystals in cerium-containing mixed oxides were smaller than those of the corresponding single oxides. Same phase compositions can be observed within each system for samples obtained by both EX and EM methods. However, in general, smaller crystalline grains resulted by EM. This is probably due to the lower calcination temperature (300 $^{o}$C) used in EM, compared to that in EX (350 $^{o}$C). As it is known that higher temperatures can cause the coalescence and growth of the bulk oxide crystallites [63], resulting in a loss of surface defects on the metal oxides, which contribute to the surface area and porosity and are usually responsible for the activity of the material. This phenomenon is called sintering and is often related with catalyst deactivation.

Table 12: Compositions, crystallite sizes and phases of cerium-containing mixed oxides detected by XRD.

| Metal oxide samples | Phase detected | Composition (vol.%) | Crystallite size (nm) |
|---|---|---|---|
| Ce-Cu CX 1:2 | $CeO_2$ | 49.19 | 7 |
| | CuO (tenorite) | 50.81 | 26 |
| Ce-Cu EM 1:1 | $CeO_2$ | 75.42 | 5 |
| | CuO (tenorite) | 24.58 | 10 |
| Ce-Cu EM 1:1 600C | $CeO_2$ | 71.9 | 11 |
| | CuO (tenorite) | 28.1 | 22 |
| Ce-Ni CX4 1:1 | $CeO_2$ | 78.46 | 8 |
| | NiO (cubic) | 21.54 | 8 |
| Ce-Ni EM 1:1 | $CeO_2$ | 83.26 | 4 |
| | NiO (cubic) | 16.74 | 6 |
| Ce-Ni EM 2:1 | $CeO_2$ | 87.76 | 5 |
| | NiO (cubic) | 12.24 | 5 |
| Ce-Co EM 1:1 | $CeO_2$ | 66.47 | 6 |
| | $Co_3O_4$ | 33.53 | 14 |
| Ce-Co EM 1:1 600C | $CeO_2$ | 64.18 | 13 |
| | $Co_3O_4$ | 35.82 | 21 |
| Ce-Co EM 1:1 800C | $CeO_2$ | 67.81 | 46 |
| | $Co_3O_4$ | 32.19 | 68 |
| Ce-Co EM 1:2 | $CeO_2$ | 49.04 | 5 |
| | $Co_3O_4$ | 50.96 | 11 |
| Ce-Co GNP 1:1* | $CeO_2$ | 77.89 | 4 |
| | $Co_3O_4$ | 22.11 | 9 |

*possibly containing contamination.

The tendency of crystallite size to increase with the rise of calcination temperature can be clearly observed in the Ce-Cu EM 1:1 and the Ce-Co EM 1:1 samples (Table 12). Calcinations at 600 $^oC$ led to a crystallite size of about twice of that found for both the Ce-Cu and the Ce-Co samples calcined at 300 $^oC$ and 800 $^oC$, with a worse case for the crystallite sizes of 45.89 nm for $CeO_2$ and 67.62 nm for $Co_3O_4$, in the Ce-Co mixed oxide. By using two portions of cobalt in the Ce-Co EM, smaller grain sizes of both $CeO_2$ and $Co_3O_4$, in comparison with the Ce-Co EM 1:1, were acquired.

A Ce-Co GNP 1:1 sample was also prepared. XRD was used to analyze the as-synthesized material (obtained after auto-ignition, without further calcination and the

smallest grain sizes were found for this sample, among all other Ce-Co materials. However, due to the incapability of cobalt to form perovskite type materials with cerium below 1000 °C [64], no further characterization or catalytic test was carried out for this material.

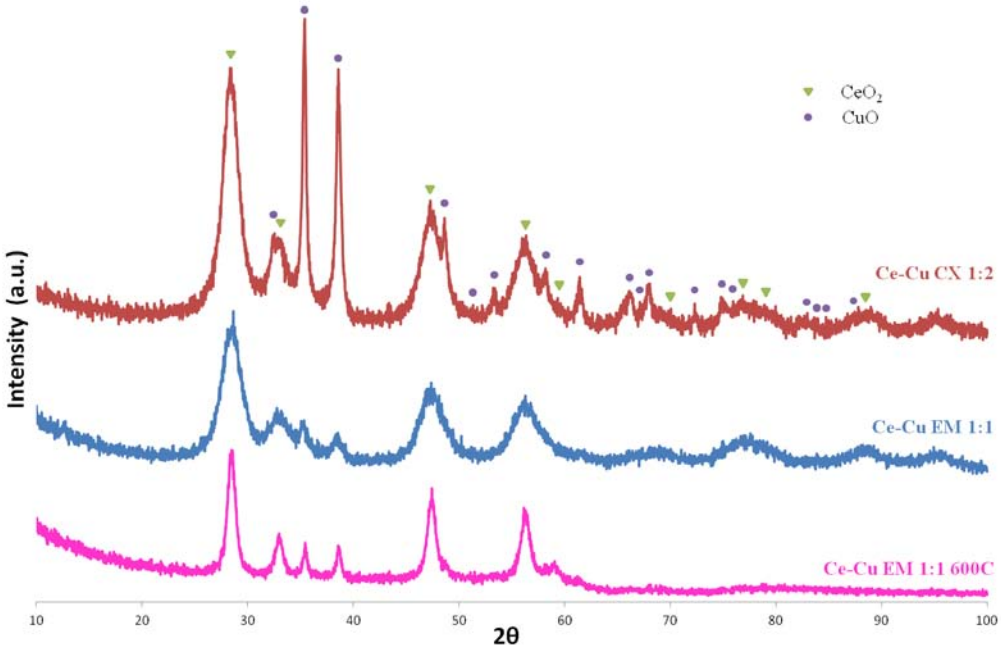


Figure 35: XRD spectra of exotemplated Ce-Cu and Ce-Cu samples prepared by EM. Miller indices from AMCSD 0011686 for $CeO_2$ and from AMCSD 0011639 for CuO.

Figure 35 shows the XRD spectra of the Ce-Cu samples. Even the materials prepared by different methods (EX and EM) contained the same phases, as shown in the above Figure that the occurrences of peaks are similar to each other. Further peaks, characterisitic of CuO, with relatively high intensities, could be observed for the Ce-Cu CX 1:2 sample. In the Ce-Cu EM material calcined at 600 °C, sharper peaks were observed, in comparison with the corresponding material prepared at lower temperature. Moreover, the peaks at higher 2θ nearly disappeared.

For Ce-Ni samples, Figure 36 shows some peaks indicating $CeO_2$for the EM 2:1 material, with higher intensities than those of the EM 1:1 sample, which can be related to the higher content of $CeO_2$ phase in the latter. The crystallite size of the NiO phase in the EM samples was smaller than that in the exotemplated sample, therefore showing a more amorphous profile in the spectra. In general, flatter peaks were found in EM samples in both Ce-Cu and Ce-Ni systems, which means that materials with more amorphous features were obtained by EM.

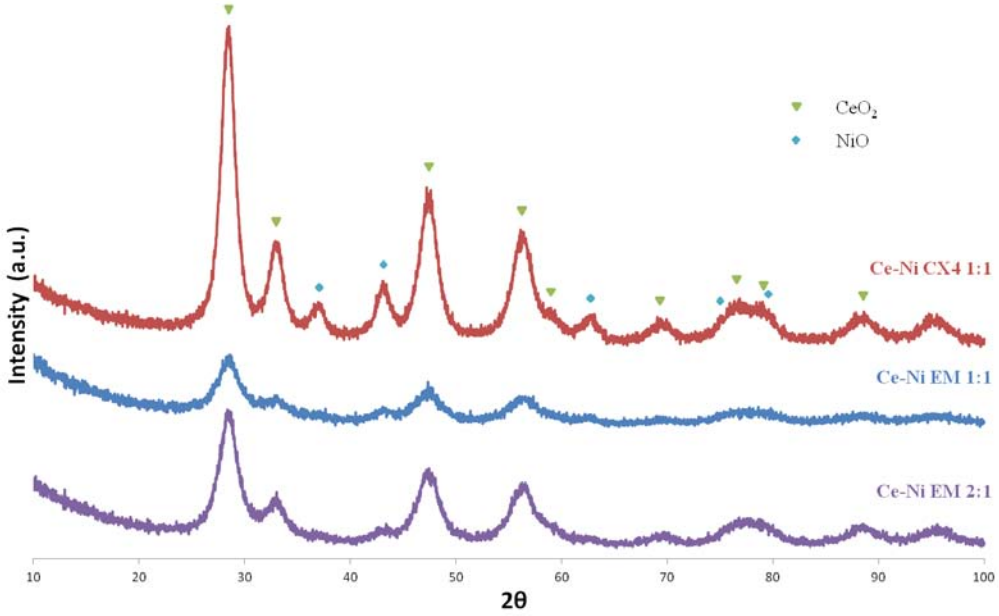


Figure 36: XRD spectra of Ce-Ni samples prepared by EX and EM. Miller Indices from AMCSD 0011686 for $CeO_2$ and from AMCSD 0017028 for NiO.

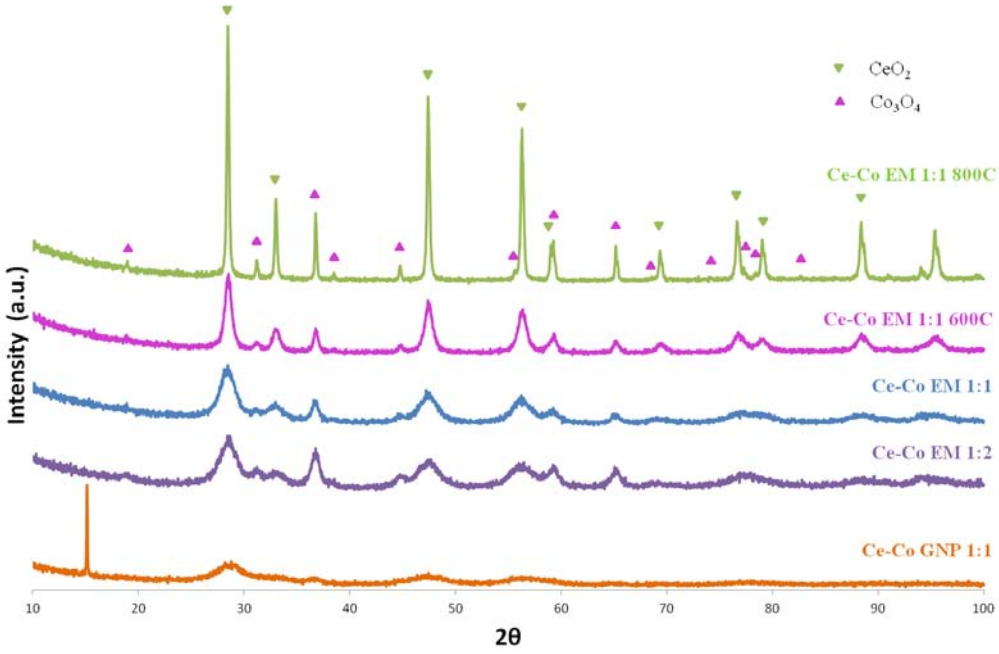


Figure 37: XRD spectra of Ce-Co samples prepared by EM and GNP. Miller Indices used for the indication of phases in the figure from AMCSD 0011686 for $CeO_2$ and from AMCSD 0007469 for $Co_3O_4$.

In the Ce-Co system, the spectra of EM samples (Figure 37) also presented amorphous profiles. However, sharper and smaller peaks could be observed for samples synthesized at higher temperatures. The 1:1 material prepared by GNP showed some flat features, recognized as $CeO_2$ and $Co_3O_4$ phases; however, a sharp peak at very low

*2θ* angle was also observed, which might result from some residual nitrate anions from the precursor.

3.2.1.3.2. Lanthanum-Containing Mixed Oxides

The phases obtained, compositions by volume percentage and crystallite sizes of selected lanthanum-containing samples are shown in Table 13.

Table 13: Compositions, crystallite sizes and phases of cerium-containing mixed oxides detected by XRD.

| **Metal oxide samples** | **Phase detected** | **Composition (vol.%)** | **Crystallite size (nm)** |
|---|---|---|---|
| La-Cu EM 1:1 | $La_2O_2CO_3$ (monoclinc)<br>CuO (tenorite) | - | - |
| La-Cu EM 1:1 600C | $La_2CuO_4$<br>CuO (tenorite)<br>Unidentified phase | - | 40<br>21<br>- |
| La-Cu EM 1:1 800C | $La_2CuO_4$<br>CuO (tenorite) | 81.38<br>18.62 | 58<br>40 |
| La-Ni EM 1:1 | NiO<br>Amorphous | - | 2 (with large uncertainty)<br>- |
| La-Co EM 1:1 | $Co_3O_4$<br>Amorphous | - | 16 (with large uncertainty)<br>- |
| La-Co EM 1:1 600C | $Co_3O_4$<br>$LaCoO_3$<br>Unidentified phase | - | - |
| La-Co GNP 1:1 600C | $Co_3O_4$<br>Amorphous | - | 20 (with large uncertainty)<br>- |
| La-Co GNP 1:1 800C | $LaCoO_3$ | 100 | 59 |
| La-Co GN-EX 1:1 600C | $LaCoO_3$ | 100 | 32 |
| La-Co GN-EX 1:1 800C | $LaCoO_3$<br>$Co_3O_4$ | 96.9<br>3.1 | 62<br>51 |

As shown in Table 13, crystallite in the material tends to grow bigger with the calcination temperature increase, due to the sintering phenomenon. However,

amorphous spectra were obtained with samples prepared at relatively lower temperature. Solid solution structures, $La_2CuO_4$ and $LaCoO_3$, were detected in La-Cu and La-Co samples calcined 600 $^oC$ and 800 $^oC$.

Figure 38 illustrates the XRD spectra of La-Cu samples. In the 800 $^oC$ sample, only $La_2CuO_4$ ($K_2NiF_4$-yupe structure) and CuO phases were detected. However, in samples prepared at lower temperatures, compositions varied a lot. More amorphous spectrum was obtained for La-Cu EM 1:1, which was mainly composed of monoclinic $La_2O_2CO_3$ and CuO. $La_2CuO_4$ was formed in the 600 $^oC$ sample, together with the presence of CuO phase and unidentified phase, which might also be $La_2O_2CO_3$, according to Abboudi et al. [65]. $La_2O_2CO_3$ is usually found with perovskite material, which can easily be formed through carbonatation of $La_2O_3$ in the atmosphere of $CO_2$ with elevated temperature. The occurrence of the formation of $La_2O_2CO_3$, in the study made by Bakiz et al. [66], was observed at 525 $^oC$, which was stable over the temperature range until 960 $^oC$. This is why, $La_2O_2CO_3$ appeared in the La-Cu EM 1:1 instead of $La_2O_3$, as a large amount of $CO_2$ was released during calcination due to the burning off of the molecular template – organic skeleton formed with oxalic acid. The presence of CuO may act as catalyst in the carbonatation process of primarily formed $La_2O_3$, so that $La_2O_2CO_3$ phase was obtained when calcined at merely 300 $^oC$. On the other hand, the stability of $La_2O_2CO_3$ may also be degraded by the dispersed CuO. Formation of $La_2CuO_4$ phase with small quantity of residual CuO was observed already in the 600 $^oC$ sample. Similar phenomena possibly exist in La-CO and La-Ni systems as well.

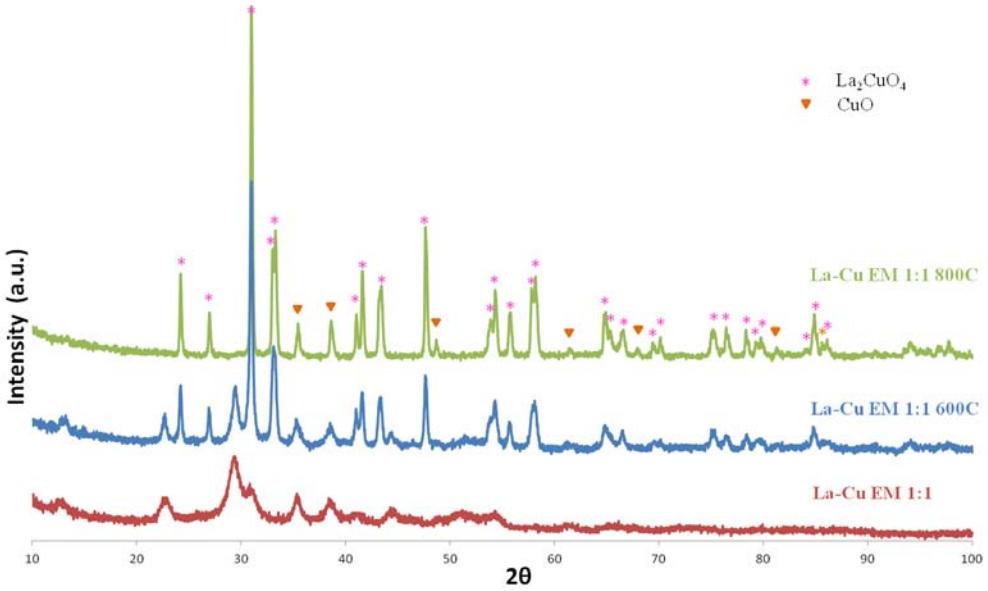


Figure 38: XRD spectra of La-Cu EM 1:1 samples. Miller Indices from AMCSD 0016433 for $La_2CuO_4$ and AMCSD 0011639 for CuO.

In La-Ni EM 1:1, no other phases than NiO could be identified due to the amorphous XRD spectrum obtained (Figure 39). However, seemingly smaller crystallite of NiO was obtained than in the Ce-Ni samples.

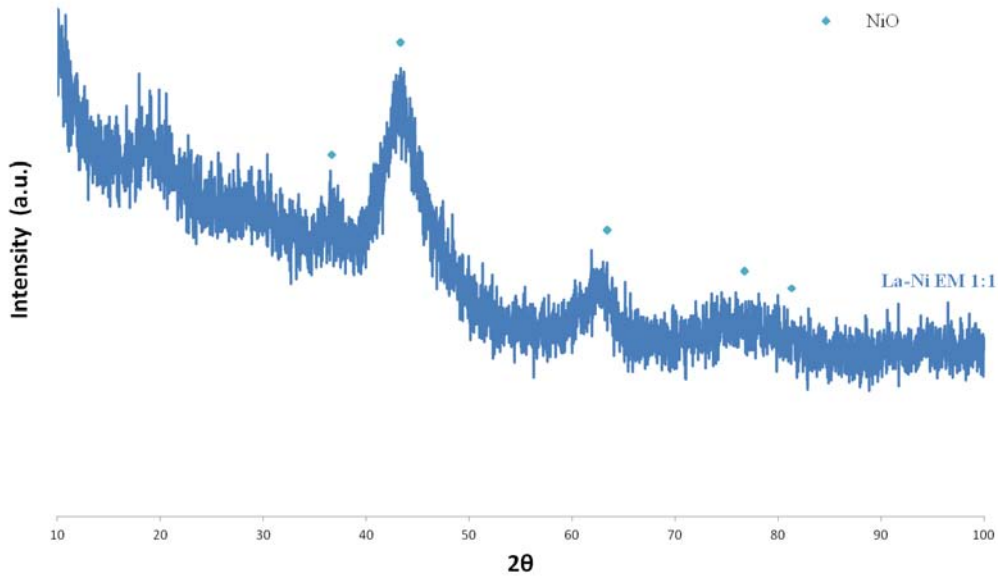


Figure 39: XRD spectra of La-Ni EM 1:1 sample. Miller Indices from AMCSD 0017204 for $La_2O_3$ and from AMCSD 0017028 for NiO.

The XRD spectra of La-Co samples are exhibited in Figure 40. Very amorphous profile was obtained in the GNP 600 $^oC$ sample, where only some $Co_3O_4$ phase could be

roughly addressed. By rising the calcination temperature to 800 °C, pure $LaCoO_3$ perovskite material was achieved. However, pure $LaCoO_3$ with perovskite structure could be successfully formed at 600 °C by combining the GNP and EX methods. The spectrum of La-Co EM 1:1 resembled the amorphous profile of the GNP sample calcined at 600 °C. However, in La-Co EM 1:1 600C, some distorted perovskite $LaCoO_3$ could be detected, with some undefined phase around $2\theta$ = 30°, perhaps being $La_2O_2CO_3$, as in the La-Cu samples.

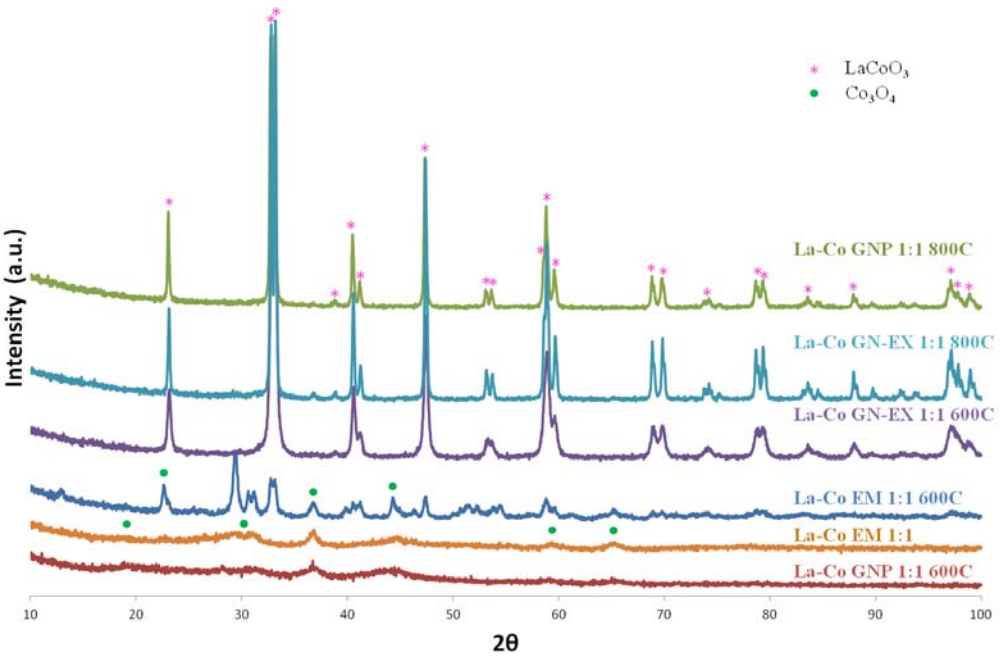


Figure 40: XRD spectra of La-Co samples. Miller Indices from JCPDS 00-048-0123 for $LaCoO_3$ and from AMCSD 0007469 for $Co_3O_4$.

### 3.2.1.4. TPR

#### 3.2.1.4.1. Cerium-Containing Mixed Oxides

Figure 41 exhibits the TPR spectra of Ce-Cu samples. Similar profiles could be observed when the same preparation method was used in the synthesis. The shape of CuO curve, consisting in a main peak with a shoulder at a lower temperature, was roughly retained in the EX Ce-Cu samples. However, the outline of $CeO_2$ could not be identified in the mixed oxides. A possible explanation for this might be that the energetic effect of binary metal oxide system joined the peaks of single CuO and $CeO_2$ together, and caused the occurrence of reduction at a lower temperature. It can be seen from Figure

41 that the main peak and the shoulder of CX 1:1 sample appeared at lower temperatures than those of the EX 1:2 sample (189 °C and 215 °C vs. 208 °C and 230 °C respectively). This is probably due to the higher content of $CeO_2$ in the 1:1 sample, which was believed to enhance the reducibility of finely dispersed CuO clusters [67]. The profiles of the reduction peaks of EM samples, however, do not much resemble the profile of CuO. Two attached reduction peaks could be observed for EM samples, the first with relatively higher intensity. A small shoulder, at about 196 °C, can be found in Ce-Cu EM 1:1, but not in the corresponding 1:2 sample. This small shoulder could be ascribed to the reduction of highly dispersed CuO species, which had stronger interaction with the $CeO_2$ phase in the material [67], therefore forming a small feature at a lower temperature. Despite this small feature, the reduction peaks of the EM 1:2 sample occurred at a reduction temperature approximately 4 °C and 9 °C lower than the reduction temperature in the 1:1 sample respectively, with an additional shoulder at nearly 20 °C above. The TPR spectra of EM 1:1 samples changed substantially when higher calcination temperatures were used. For the 600 °C sample, the shoulder was stretched to a 30 °C lower temperature than in the EM 1:1 material calcined at 300°C. A single main peak appeared at about 230 °C, instead of two peaks, with a small shoulder approximately 10 °C higher. For the sample calcined at 800 °C, a tiny shoulder could be seen at about 161 °C. However, the main reduction peak in this sample was saturated between 230 °C and 250 °C.

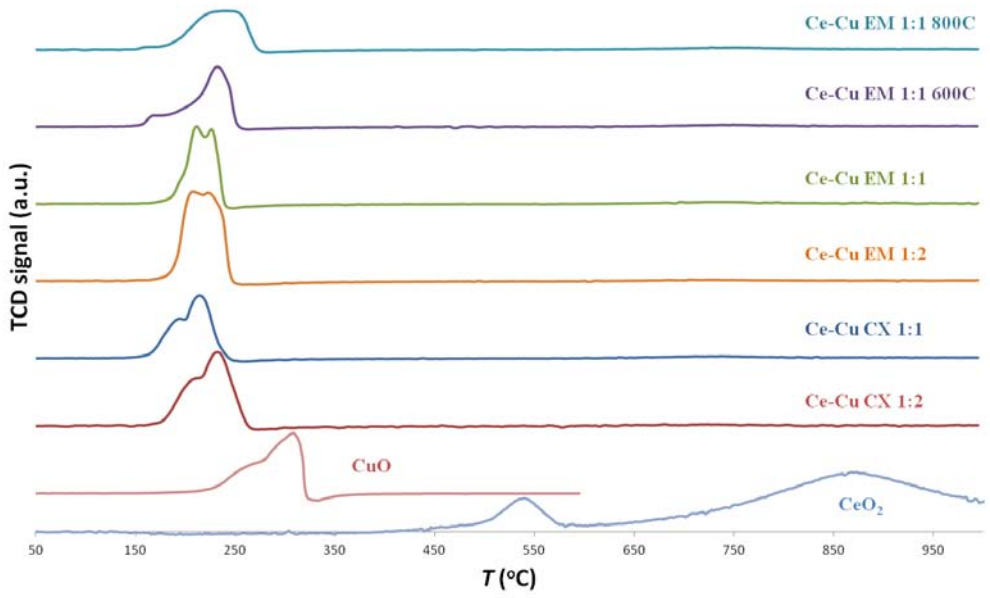


Figure 41: TPR spectra of Ce-Cu samples with commercial CuO and $CeO_2$ for comparison.

For the Ce-Ni system, the TPR spectra of the series of the EX and EM samples are shown in Figure 42. Similar profiles were found in all EX materials. Generally, two small peaks appeared at a lower reduction temperature followed by a broad saturated peak. The lowest reduction temperatures corresponding to the occurrences of the peaks were obtained with Ce-Ni CX2 1:1, at 213 $^{o}$C and 262 $^{o}$C as well as between 296 and 353 $^{o}$C respectively. This sample also had the second largest BET surface area among EX materials. The EM samples also followed a three-step reduction as three peaks could be seen in each of the spectrum, however, with different shape from the EX samples: the 1$^{st}$ reduction peak grew larger and the 3$^{rd}$ became less saturated. The 3$^{rd}$ peak probably is related to the reduction of NiO in the material, as the intensity increased with the presence of larger portion of nickel precursor used in material preparation. If the EX samples are also taken into consideration, it seems that the 2$^{nd}$ reduction peak could also be attributed to the NiO reduction as a broad peak with a shoulder were detected in the TPR spectrum of commercial NiO. And the shoulder in NiO reduction, possibly resulted from the reduction of surface oxygen, was split from the main peak in mixed oxides. Then consequently the 1$^{st}$ reduction peak could be related to some transformation in the $CeO_2$ phase.

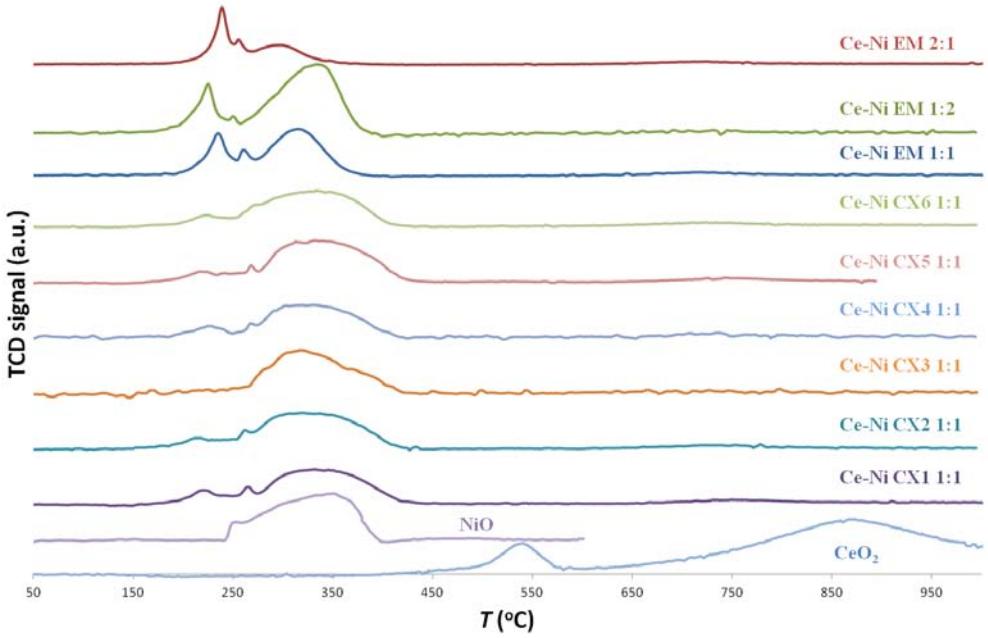


Figure 42: TPR spectra of Ce-Ni samples with commercial NiO and $CeO_2$ for comparison.

The reduction temperatures for EM samples are listed in Table 14. The 1$^{st}$ and 2$^{nd}$ reduction peaks of the 1:2 sample appeared at relatively lower temperatures. However,

for the 3rd step, only 298 °C was required for the 2:1 sample, whereas 335 °C (the highest temperature) was needed for the 1:2 sample.

Table 14: Reduction temperatures of Ce-Ni EM samples.

| Samples | 1st peak (°C) | 2nd peak (°C) | 3rd peak (°C) |
|---|---|---|---|
| Ce-Ni EM 1:1 | 234 | 260 | 314 |
| Ce-Ni EM 1:2 | 225 | 250 | 335 |
| Ce-Ni EM 2:1 | 239 | 255 | 298 |

As for Ce-Co samples, their TPR spectra contained more complicated features (Figure 43). That might come from the $Co_3O_4$, which potentially can go through a three-step reduction, as the reduction of surface oxygen happens first and then is followed by transitions of $Co_3O_4 \rightarrow CoO$ and $CoO \rightarrow Co$ [68]. Similar profiles were obtained for EX samples with CX and CXN, with the reduction peaks of Ce-Co CXN 1:2 appearing at slightly lower temperatures than the peaks of the CX sample. However, larger variations could be found in the TPR spectra of EM samples. The differences diminished with the calcination temperature increase as the two EM samples calcined at 800 °C resembled each other although a larger shoulder could be observed in the Ce-Co EM 1:2 800 ºC material, which might be ascribed to the higher Co content of this material. Two main peaks were seen in 600 ºC samples, with a concave profile for the 1:2 material. For EM materials calcined at 300 °C, the TPR spectrum of the 1:2 sample followed a similar tendency as for the EX materials, yet with a larger peak at approximately 330 °C, and a smaller one at 490 °C. This phenomenon was aggravated in the EM 1:1 sample. If the explanation for the larger shoulder drawn for the 800 ºC sample is valid, then the larger peak in Ce-Co EM 1:1 could be related to the reduction of $CeO_2$. That is, the energetic effect in the Ce-Co binary oxide system improved significantly the reducibility of $CeO_2$. It can also be observed that higher calcination temperatures brought the reduction of cobalt oxide to lower temperatures.

Unlike in EX samples, EM led to two small peaks below 250 °C for materials prepared at 300 °C: about 171 °C and 204 °C for Ce-Co EM 1:2 and about 173 °C and 205 °C for Ce-Co EM 1:1. As shown in Figure 43, with the exception of the last reduction, the TPR profile of Ce-Co EM samples was shifted to higher temperatures, with the calcination temperature increase for both EM 1:1 and EM 1:2 materials. This is probably related to

material sintering. In fact, the information on the reducibility matches well with the BET surface areas and XRD results. Upon higher calcination temperatures, BET surface area and the reducibility of the material tend to decrease, and the crystallite size tends to increase.

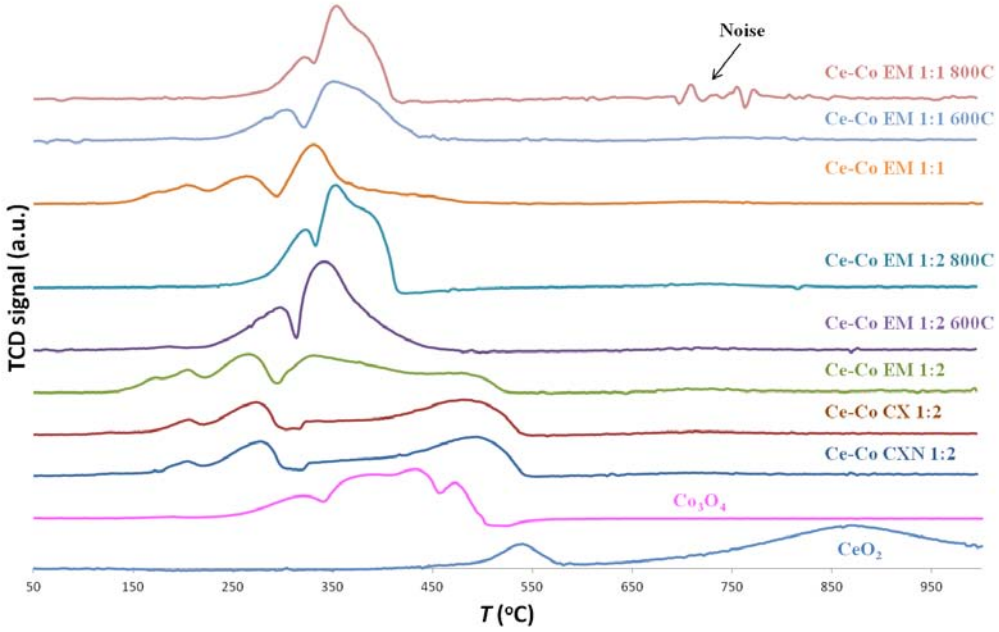


Figure 43: TPR spectra of Ce-Co samples with commercial $Co_3O_4$ and $CeO_2$ for comparison.

### 3.2.1.4.2. Lanthanum-Containing Mixed Oxides

The TPR spectrum of exotemplated $La_2O_3$ was presented in Figures 44 and 47 to 48 for comparison, instead of that of commercial $La_2O_3$. The reason is that a hydroxyl phase of lanthanum was obtained for the commercial sample, resulting in the detection of a negative TCD signal [53]. Lanthanum oxide can be potentially hydrated even at room temperature [53]. More information on this matter can be found in Appendix 1.

#### 3.2.1.4.2.1. La-Cu System

The TPR spectra of all La-Cu samples are shown in Figure 44. The PC samples showed the lowest reducibility as the reduction peaks appeared at higher temperatures than in EX and EM samples. Also a tendency of an increase in the reducibility could be seen with different material preparation methods for both 1:1 and 1:2 samples with the

following trend: EM>EX>PC. Among all samples, the reduction peaks of La-Cu PC 1:1 appeared at the highest temperatures, corresponding to the lowest reducibility.

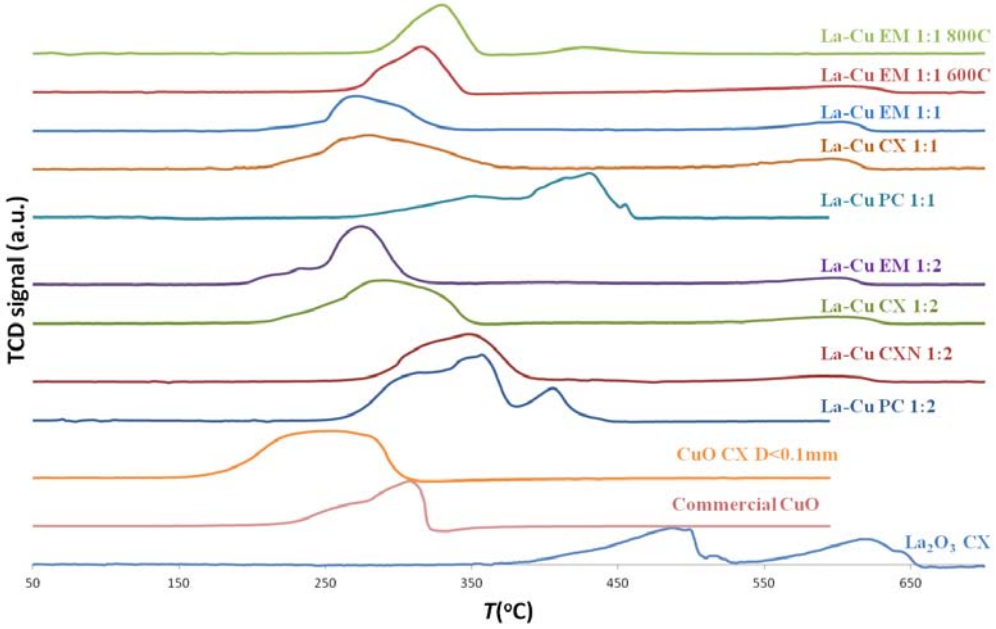


Figure 44: TPR spectra of La-Cu samples with exotemplated CuO and $La_2O_3$ and commercial CuO for comparison.

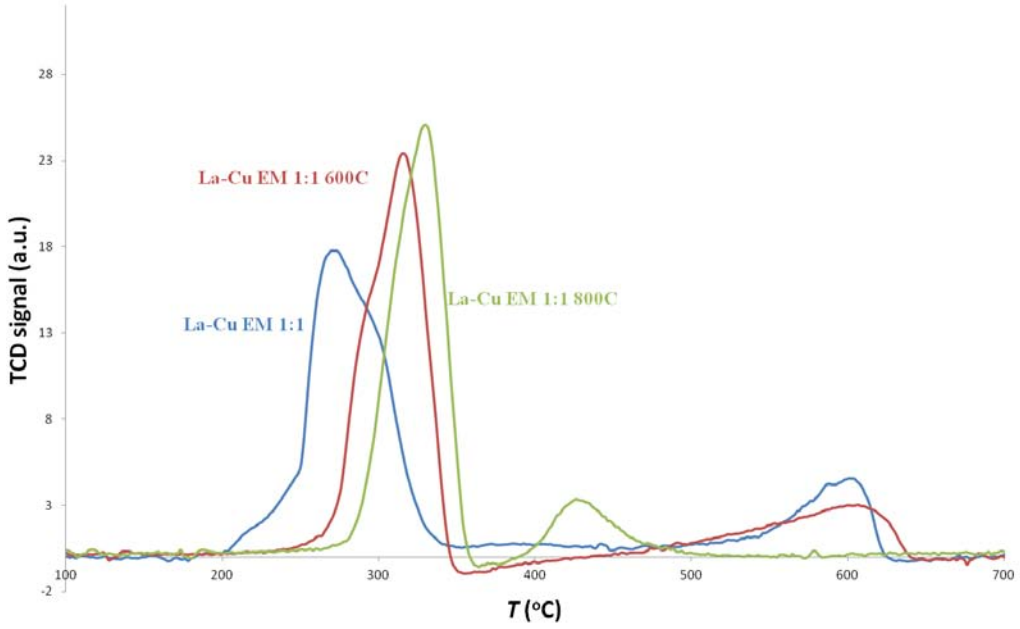


Figure 45: TPR spectra of LaCu 1:1 samples prepared by EM using different calcination temperatures.

Figure 45 presents the TPR spectra of La-Cu EM 1:1 samples obtained with different calcination temperatures. The first reduction peak was shifted to higher temperature

with calcination temperature increase. This could be resulted from the formation of $La_2CuO_4$ in materials calcined at higher temperature. Merino et al. [69] presented two reduction mechanisms of perovskite-type materials, with a typical formula of $ABO_3$, one proposed by Nakamura et al. and the other by Wachowski et al.. In the former statement, the perovskite follows a four-step reduction: formation of an oxide of the B cation, followed by a formation of a spinel structure, then the reduction of the B cation and, finally, transformation to $La_2O_3$ and metallic Co. However, Wachowski et al. interpreted it as a two-step reduction, with a partial reduction to an intermediate perovskite and then to metallic Co and $La_2O_3$. Arakawa et al. [70] reported a similar reduction process as that of Wachowski et al., with reduction proceeding through the formation of a series of oxygen-deficient structures to keep the perovskite structure. According to the XRD results, $La_2CuO_4$ phase presented in the 600 $^oC$ and 800 $^oC$ samples, which is regarded as the partial reduction product of the corresponding $ABO_3$ (perovskite-type oxides), with a $K_2NiF_4$-type structure [71], but not spinel [72]. Also a small amount of CuO was detected. Therefore, this peak in the TPR spectra of La-Cu samples calcined at higher temperatures can be attributed to the reductions of CuO and $La_2CuO_4$, its shape resembling the reduction profile of commercial CuO.

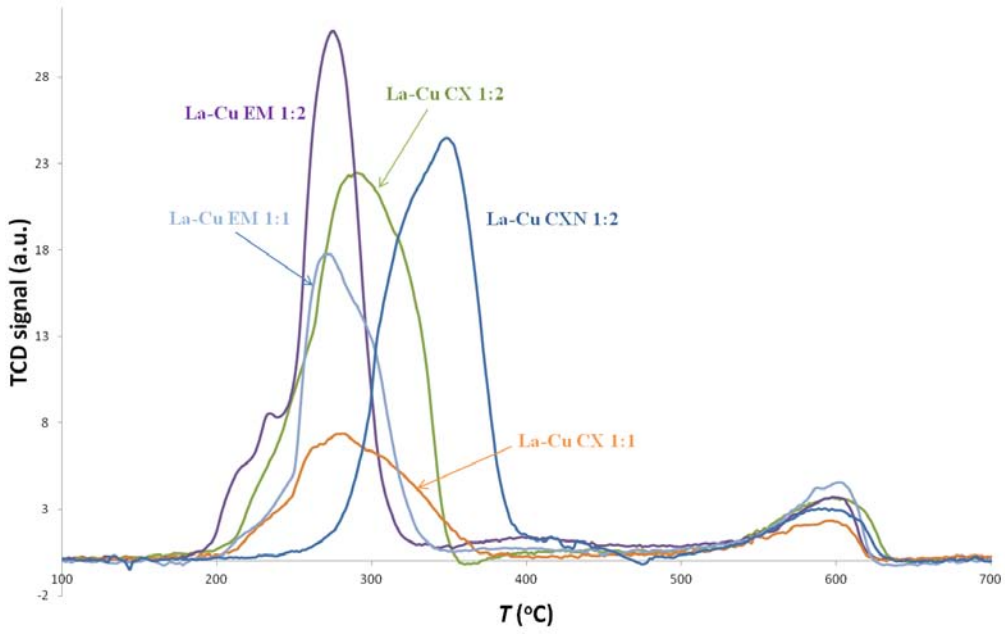


Figure 46: TPR spectra of LaCu 1:1 and 1:2 samples prepared by EX and EM.

For EX samples shown in Figure 44, the appearance of this peak (broader and more saturated) is more similar to that of the CuO CX. The second peak at a higher

temperature probably is due to the reduction of $La_2O_3$ formed after the first stage of the reduction, being its position in the spectra similar to that of the second reduction peak in the CX templated $La_2O_3$, with the exception of the 800 ºC sample, in which the second reduction peak appeared at a temperature around 150 $^oC$ lower than in the other two samples. A shoulder in the reduction profile of La-Cu EM 1:1 was lying on the higher temperature side after the main peak, with some flatter features before the main peak at lower temperature, whereas only a small shoulder could be observed in samples calcined at higher temperature. This could be related to the phase transformation from the physical mixture of CuO and $La_2O_2CO_3$ to a material mainly containing $La_2CuO_4$.

The reduction profiles of EM and EX samples can be compared in Figure 46. The reduction peaks in EM samples appeared at lower temperatures, 268 $^oC$ for EM 1:1 and 271 $^oC$ for EM 1:2. The highest reduction temperature was observed for the CXN templated sample, around 60 $^oC$ higher than in CX templated material. La-Cu CX 1:1 had the lowest reduction temperature (278 $^oC$) among all exotemplated samples.

3.2.1.4.2.2. La-Ni System

For La-Ni samples, the reduction profiles look very similar to that of the single exotemplated NiO as exhibited in Figure 47. The first two peaks can be assigned to the reduction of NiO and the peak appearing at higher temperature is due to $La_2O_3$ reduction. Two shoulders can be observed in La-Ni EM 1:1, which, however, change into small peaks for the 1:2 sample. The whole reduction spectrum was shifted to lower temperature when two portions of nickel were used in material preparation.

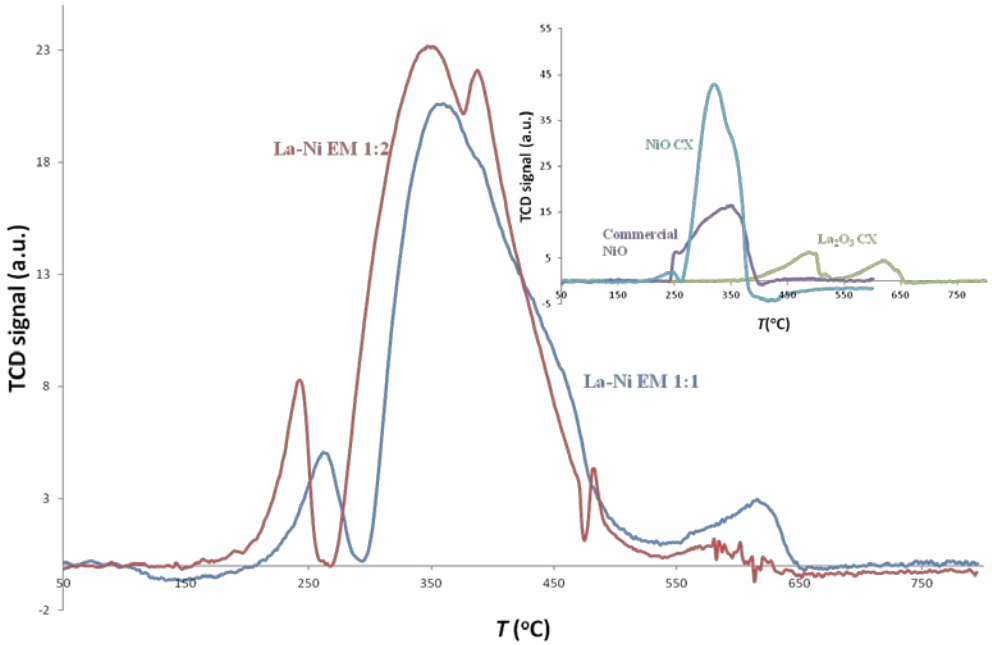


Figure 47: TPR spectra of La-Ni EM samples.

### 3.2.1.4.2.3. La-Co System

The TPR spectra of all La-Co samples are plotted in Figure 48 and reduction profiles with similar shapes can be seen. Enlarged detailed representations of the TPR spectra of samples obtained by different preparation methods are shown in Figures 49 to 52, and the TPR spectra of samples by different calcination temperatures are presented in Figures 53 to 55.

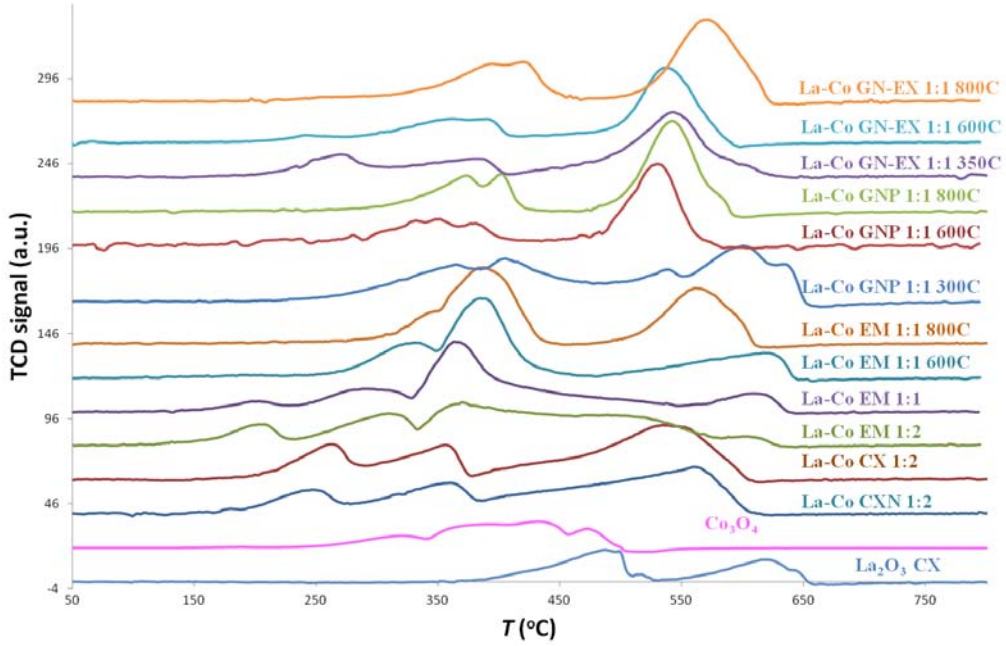


Figure 48: TPR spectra of La-Co samples with EX $La_2O_3$ and commercial $Co_3O_4$ for comparison.

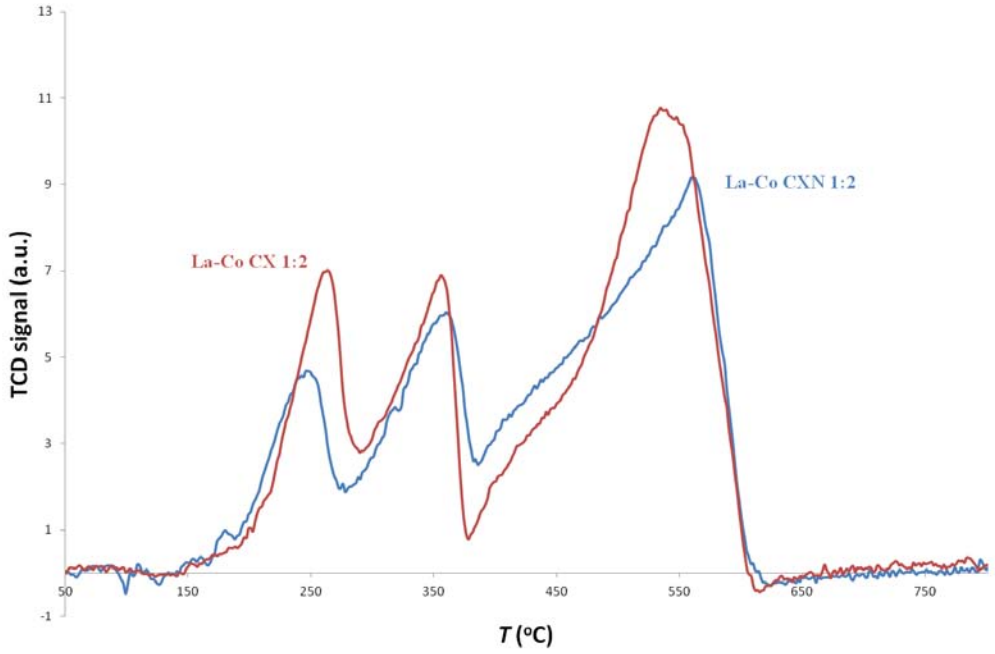


Figure 49: TPR spectra of La-Co EX samples.

Figure 49 shows the comparison of exotemplated La-Co samples. Three reduction peaks could be observed in both CX and CXN template materials, with a shoulder on the 3rd peak to the lower temperature side. The first peak could be assigned to the reduction of cobalt oxides, as the reduction of $Co^{3+} \rightarrow Co^{2+}$ occurs in the temperature range of 150 °C to about 450 °C [30]. The last peak may be resulted from the

transition of $La^{2+} \rightarrow La^{0}$, as no further reduction was observed even till 1000 $^{o}$C (the TPR analyses were carried out till 1000 $^{o}$C). The first reduction step in $La_2O_3$ ($La^{2+} \rightarrow La^{0}$) and the second in $Co_3O_4$ ($Co^{2+} \rightarrow Co^{0}$) possibly overlapped, which appeared as the 2$^{nd}$ reduction peaks in the TPR spectra shown in Figure 49.

EM samples are presented in Figure 50. The lowest reduction temperature was found for the La-Co EM 1:2. Four reduction peaks are seen in La-Co EM 1:1, whereas in the 1:2 sample, a shoulder additionally appeared after the third peak, its intensity being much lower than that of the 1:1 sample and the size of the last peak also reduced in the 1:2 sample. The new shoulder occurring after the third peak might be related to the reduction of $Co_3O_4$, together with the first two peaks with higher intensities in the 1:2 sample than in the 1:1 sample. The third peak, on the other hand, perhaps is due to the reduction of $La_2O_3$. Figure 50 also shows that the first three peaks gradually merged into one with the increasing calcination temperature and, in the end, for the La-Co EM 1:1 800C, only a small shoulder could be observed on the lower temperature side of the main peak. This could be attributed to the formation of some perovskite-type structure in the materials calcined at 600 $^{o}$C and 800 $^{o}$C. The shoulder in the 800 $^{o}$C sample and, partially, the small peak in the 600 $^{o}$C material could be ascribed to the partial reduction of perovskite $LaCoO_3$ to an intermediate perovskite with oxygen-deficient structures. And similarly, as in the La-Cu system, the last reduction peak of the 800 $^{o}$C sample, possibly due to the reduction of $La^{2+} \rightarrow La^{0}$, was shifted to a lower temperature.

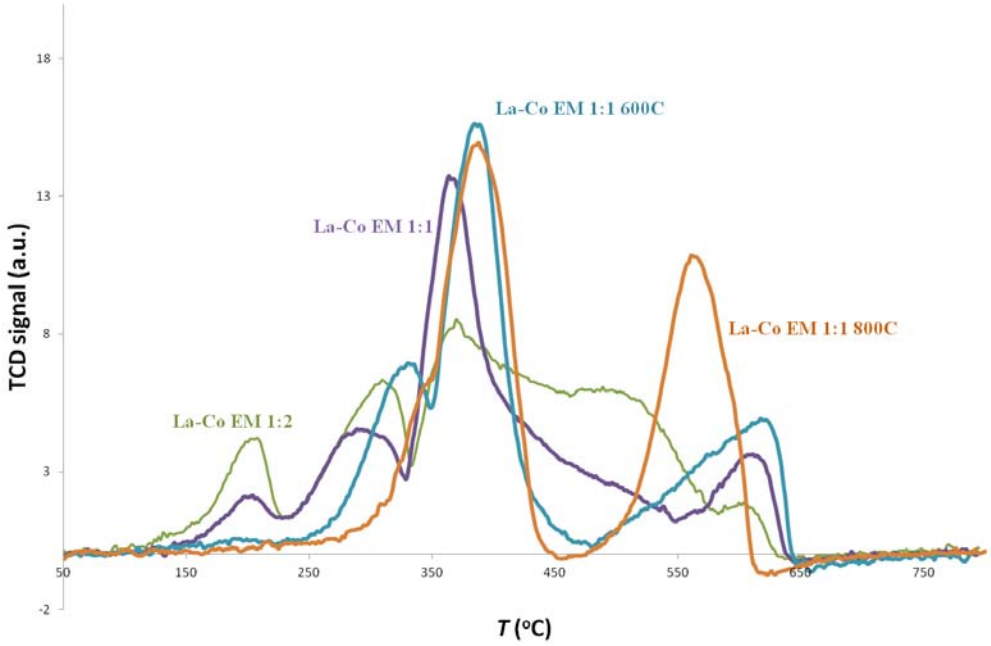


Figure 50: TPR spectra of La-Co EM samples.

For GNP samples, XRD shows that pure perovskite $LaCoO_3$ was formed in the 800 °C sample. However, very amorphous XRD profiles were obtained with the other two materials calcined at lower temperature, with some elusive peaks detected in the 600 °C sample, corresponding to the presence of the $Co_3O_4$ phase. Although some noisy patterns were found in the TPR spectrum of the 600 °C sample, perhaps due to some instrumental errors, the reduction profile followed a similar curve as the perovskite $LaCoO_3$ calcined at 800 °C, with two adjacent peaks between 350 °C and 400 °C and one single peak at around 540 °C, although the whole spectrum of the 600 °C sample appeared at a slightly lower temperature. The reduction spectrum of La-Co GNP 1:1 800C resembled the TPR results reported in literature [30, 69]. In the 300 °C sample, however, besides the two adjacent peaks below 450 °C and a small peak at around 540 °C, another peak with high intensity occurred at about 600 °C with a shoulder at around 640 °C.

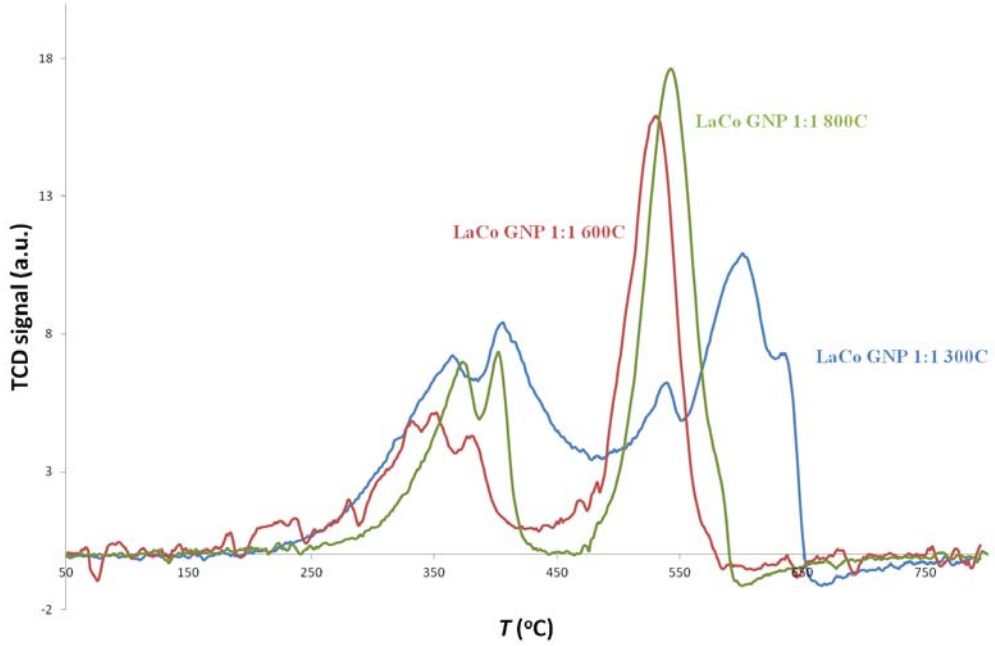


Figure 51: TPR spectra of La-Co GNP samples.

For GN-EX materials presented in Figure 52, perovskite-type reduction profile as in literature [30, 69] could be observed in the 600 $^{o}$C and 800 $^{o}$C samples, which aligned well with the XRD results. However, a small feature at around 250 $^{o}$C can be additionally seen in these materials, which was also present in the 350 $^{o}$C sample with higher intensity. As it can be seen in the Figure 52, the reduction profile tends to shift to higher temperature with an increase in the calcination temperature during material preparation.

The TPR spectra of La-Co samples prepared using different calcination temperatures are presented in Figures 53 to 55. The reduction profiles of the La-Co oxides prepared at lower temperature (300 $^{o}$C and 350 $^{o}$C) were very different from each other. However, these deviations diminished with the calcination temperature increase. In the 800 $^{o}$C samples synthesized by different methods, as demonstrated in Figure 55, the reduction peaks occurred at very similar temperatures. This could result from phase transformations in the material, that is, a change from a physical mixture of $Co_3O_4$ and $La_2O_3$ to a La-Co solid solution.

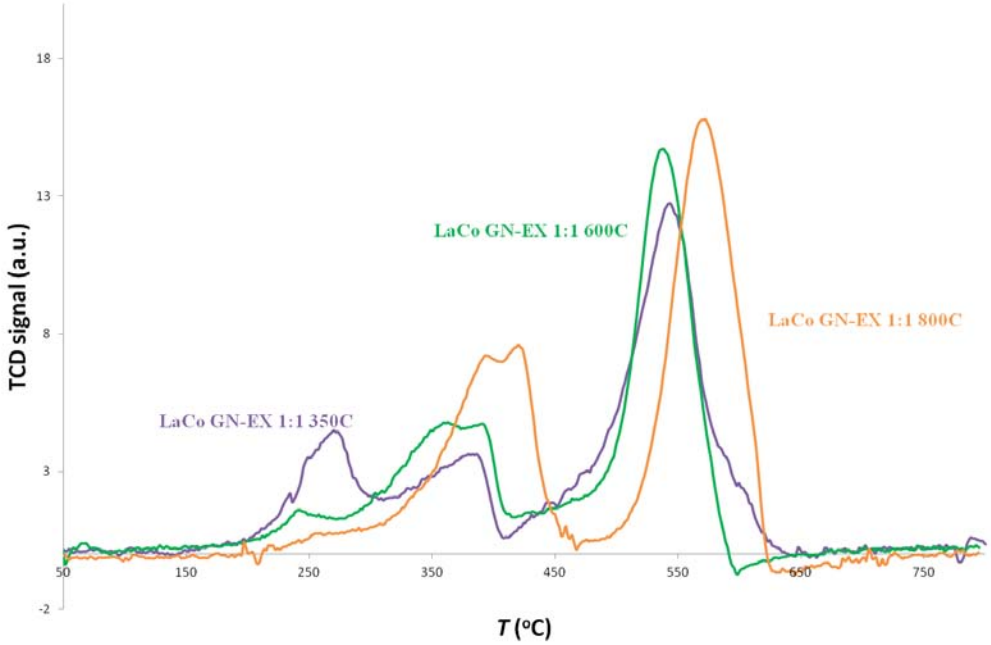


Figure 52: TPR spectra of La-Co GN-EX samples.

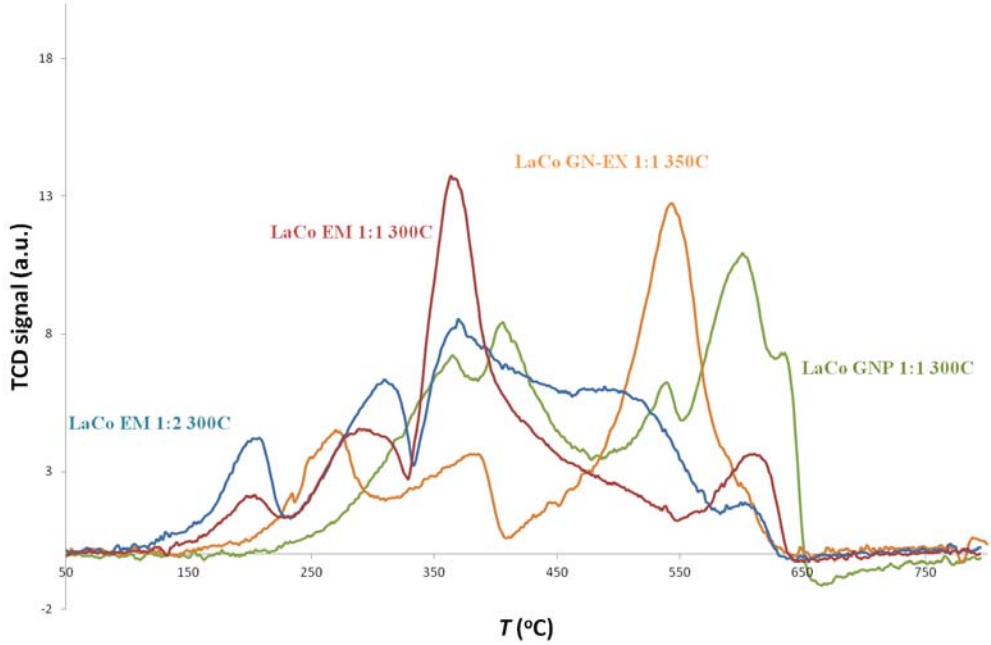


Figure 53: TPR spectra of La-Co samples calcined at 300 °C and 350 °C.

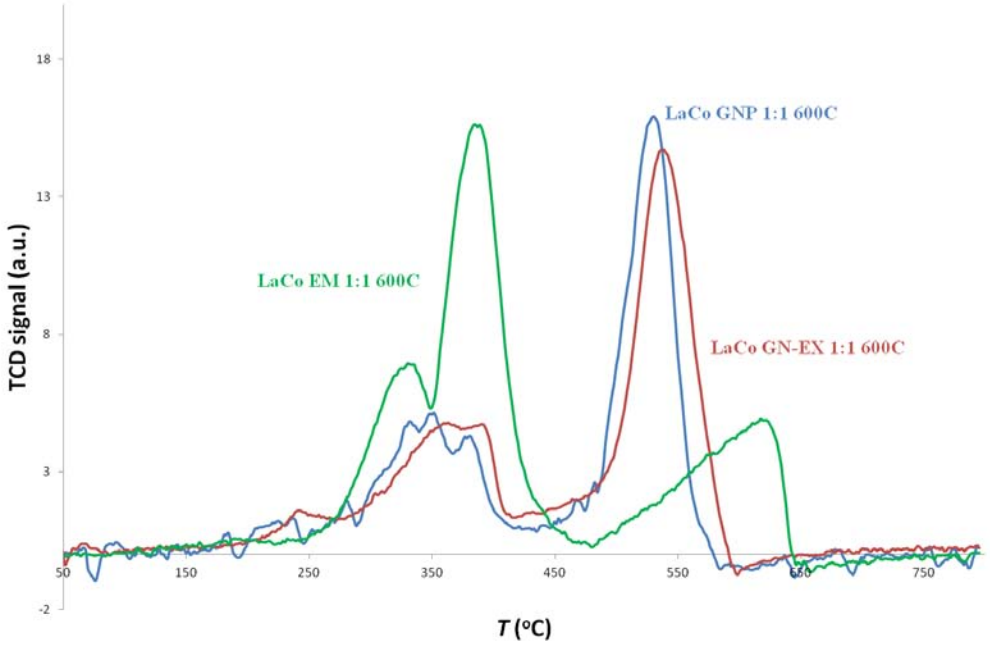


Figure 54: TPR spectra of La-Co samples calcined at 600 °C.

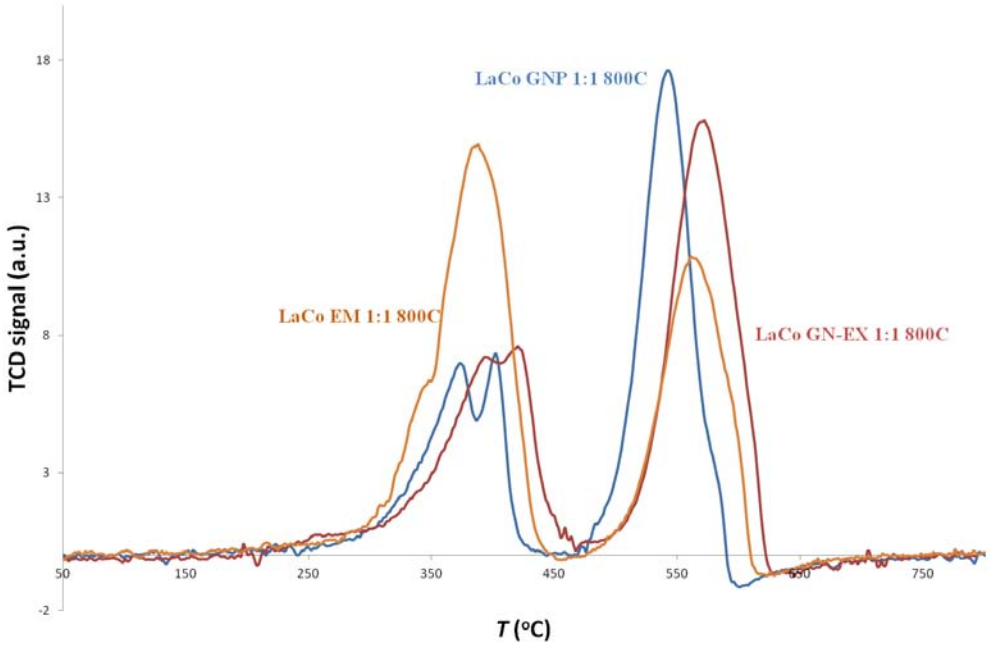


Figure 55: TPR spectra of La-Co samples calcined at 800 °C.

### 3.2.2. Catalytic Performance Tests

The prepared materials were tested as catalysts on the oxidation of ethyl acetate. The catalytic results for cerium-containing samples are presented separately in Section 3.2.2.1 and the catalytic results for lanthanum-containing samples in Section 3.2.2.2. A

comparison of the catalytic performances of selected samples can be found in Section 3.2.2.3.

### 3.2.2.1. Cerium-Containing Mixed Oxides

The catalytic performances of Ce-Cu samples are shown in Figure 56. The EM 1:2 sample had the lowest onset temperature. However, it achieved the full conversion of ethyl acetate to $CO_2$ and $H_2O$ at a slightly higher temperature than the EM 1:1 sample. This is probably due to the larger BET surface area and smaller phase crystallite sizes in the EM 1:1 material and its higher reducibility at lower temperature. A similar tendency can be observed for the exotemplated materials although slightly higher temperatures (7-9 $^{o}$C) were required for the complete oxidation of ethyl acetate. A decrease in the catalytic activities of the prepared materials could be found for the EM samples, with the calcination temperature increase.

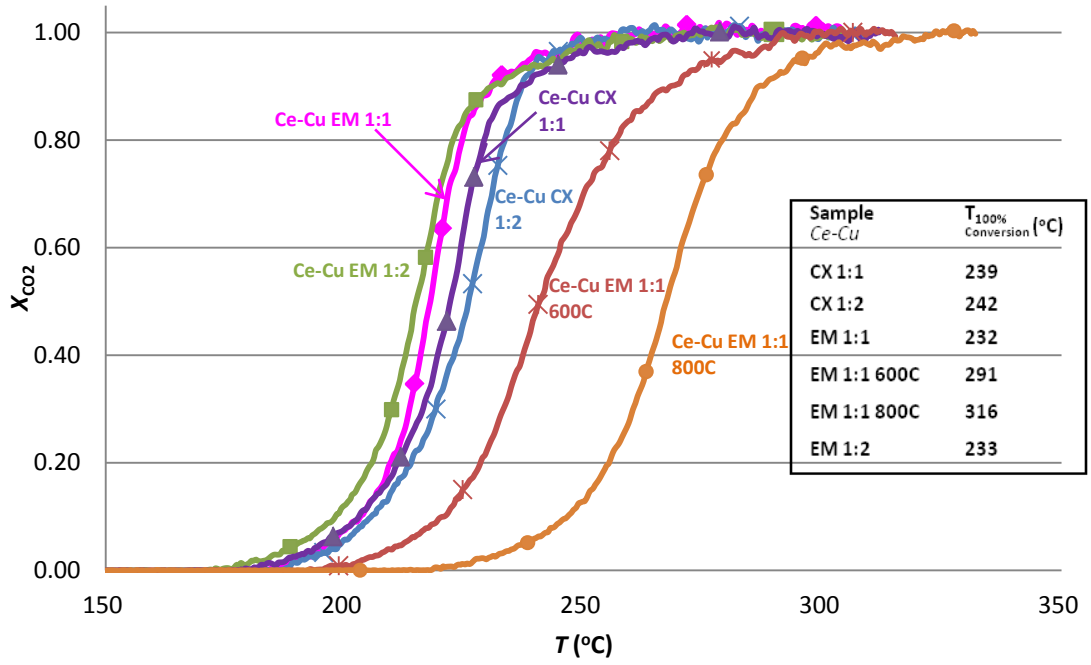


Figure 56: Catalytic performances of Ce-Cu samples.

For the Ce-Ni samples, shown in Figure 57, the EX materials needed higher temperatures for achieving the 100% conversion of ethyl acetate to $CO_2$, than the EM samples, with the exception of the Ce-Ni EM 2:1 material. Full conversion at the lowest

temperature (250 °C) was achieved by the EM 1:1 sample, whereas 10 °C more were required for the EM 1:2 sample.

Figure 58 shows the catalytic results of Ce-Co samples for the oxidation of ethyl acetate. EM 1:1 and EM 1:2 were the most active samples among all tested materials, as they catalyzed the reaction to full conversion at just 225 °C. This could be attributed to the slightly smaller surface area and larger phase crystallite sizes found in the EM 1:1 sample. As observed above with the Ce-Cu and Ce-Ni samples, EX Ce-Co materials also had lower activities than the EM samples. Even though higher temperatures were generally needed by the EX oxides, CXN showed a better performance as templating material. With higher calcination temperature, the catalytic activity of the EM materials dropped significantly, which is in agreement with the results obtained for the BET surface area, crystallite size and reducibility of the samples.

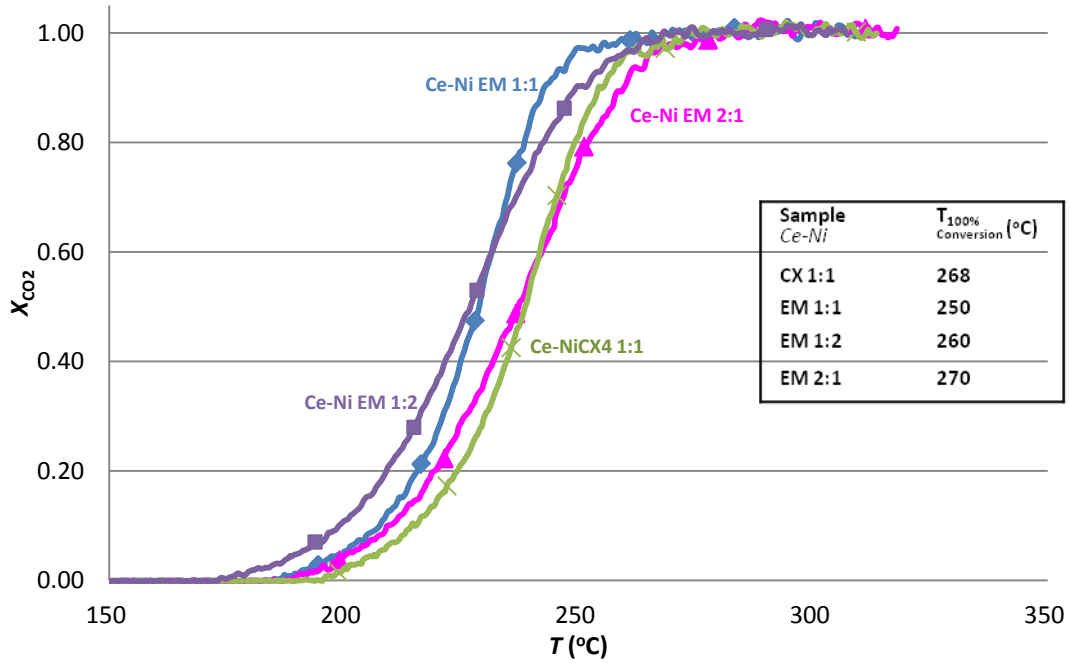


Figure 57: Catalytic performances of Ce-Ni samples.

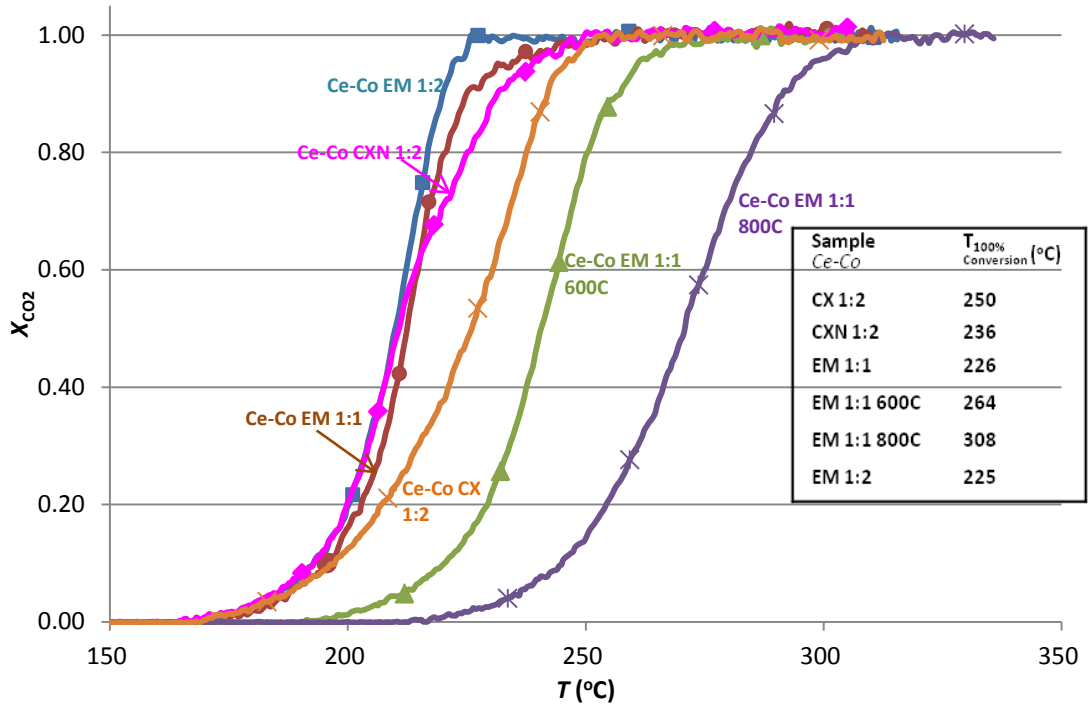


Figure 58: Catalytic performances of Ce-Co samples.

The most active material within cerium-containing samples was Ce-Co 1:2 EM, which catalyzed the oxidation reaction of ethyl acetate to 100% conversion to water and carbon dioxide at 225 °C. In general, EM samples showed better catalytic performances than the corresponding EX materials. The 1:1 samples in Ce-Cu and Ce-Ni systems showed higher catalytic activities than the corresponding 1:2 samples for the same preparation method. However, the opposite happens with Ce-Co mixed oxides, with merely a 1 °C difference in the full conversion temperature. For both Ce-Cu and Ce-Co systems, higher calcination temperatures were found to have adverse effects on the catalytic activity of the materials. The tested cerium-containing samples followed the following sequence: Ce-Co EM 1:2 > Ce-Co EM 1:1 > Ce-Cu EM 1:1 > Ce-Cu EM 1:2 > Ce-Co CXN 1:2 > Ce-Cu CX 1:1 > Ce-Cu CX 1:2 > Ce-Co CX 1:2 = Ce-Ni EM 1:1 > Ce-Ni EM 1:2 > Ce-Co EM 1:1 600C > Ce-Ni CX 1:1 > Ce-Ni EM 2:1 > Ce-Cu EM 1:1 600C > Ce-Co EM 1:1 800C > Ce-Cu EM 1:1 800C. The CXN templated Ce-Co material had better catalytic result than the CX sample, showing that CXN was a better templating material for the Ce-Co mixed oxides. Ce-Ni was less active than the Ce-Co and Ce-Cu systems.

3.2.2.2. Lanthanum-Containing Mixed Oxides

The onset of the $CO_2$ conversion in the catalytic oxidation of ethyl acetate catalyzed by La-Cu samples occurred approximately at a 30 $^oC$ higher temperature (Figure 59) than in the case of Ce-Cu mixed oxides (Figure 56). A sample prepared by PC was tested for comparison, but it failed in catalyzing the oxidation reaction to full conversion in the studied temperature range. Low catalytic activities were also observed for CXN 1:2 EM 1:1 and EM 1:1 800ºC.

Unlike the cerium-containing materials, in which higher calcination temperatures led to samples with lower catalytic activities, a drastic improvement was shown for the Ce-Cu EM 1:1 600C sample, in comparison with the EM 1:1 oxide prepared at 300 $^oC$. This is probably attributed to the formation of $La_2CuO_4$ phase with a $K_2NiF_4$-type structure in the 600 $^oC$ sample, corresponding to a larger BET surface area. $La_2CuO_4$ phase was also detected for LaCu EM 1:1 800C, however, this sample was far less active than the 600 $^oC$ sample. The reason for this, might be related to the unidentified phase in Ce-Cu EM 1:1 600C, which could be $La_2O_2CO_3$ according to Abboudi et al. [65]. Appropriate amount of $La_2O_2CO_3$ in catalyst can enhance the catalytic activity, whereas too high content of $La_2O_2CO_3$ hinders the catalytic performance [73, 74]. This possibly also explains the poor catalytic activity of La-Cu EM 1:1, where mainly $La_2O_2CO_3$ monoclinic phase and CuO phase were detected. In comparison with the CX templated materials, the La-Cu EM 1:2 sample, however, was capable of catalyzing the oxidation reaction to full conversion, but a higher temperature was needed. Slightly higher temperature was needed for the CX 1:1 sample than for the corresponding 1:2 material.

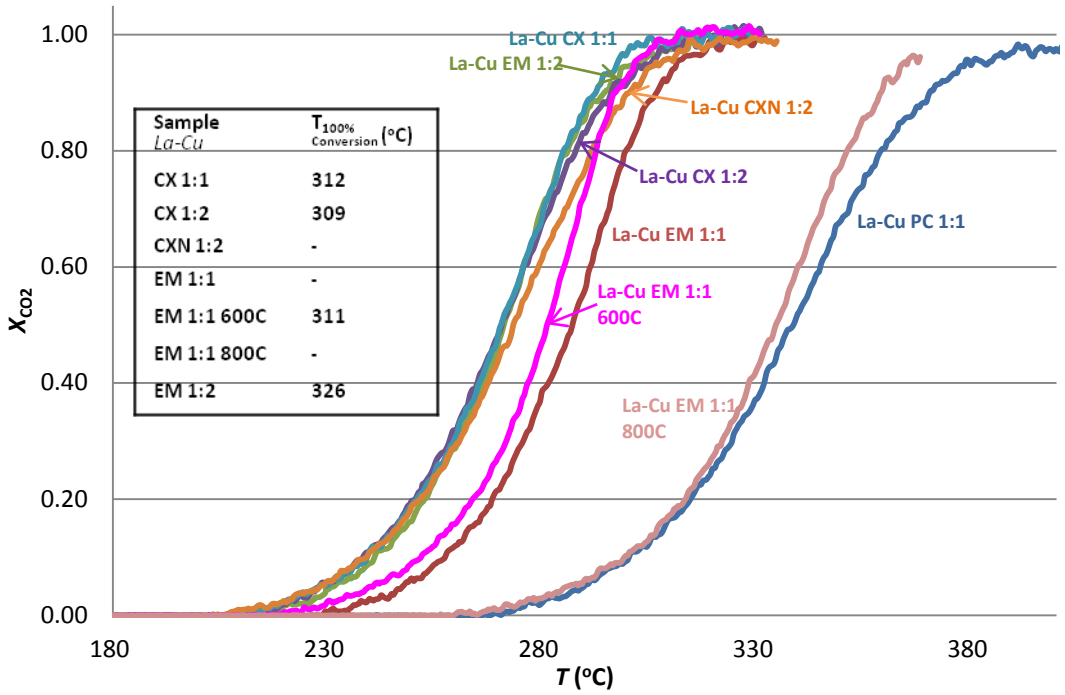


Figure 59: Catalytic performances of La-Cu samples.

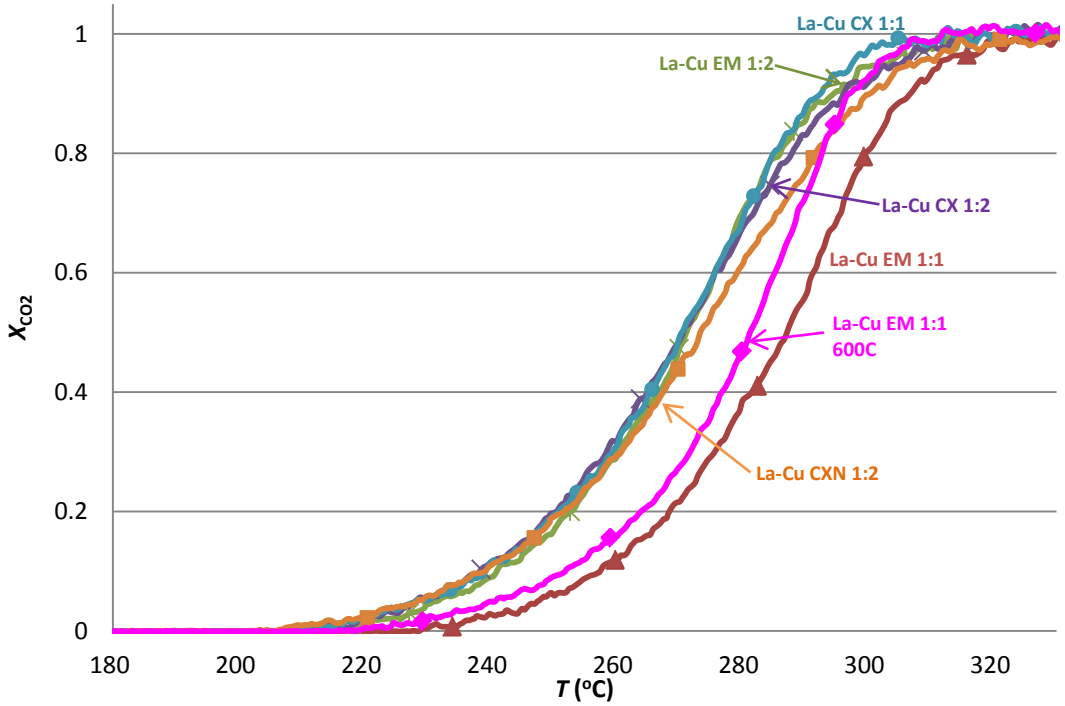


Figure 60: Catalytic performances of selected La-Cu samples.

The two La-Ni samples prepared by EM were also tested. Contrary to the trend shown in the Ce-Ni system, a lower temperature was needed for the 1:2 than for the 1:1

sample (Figure 61) for the conversion of VOC. 100% conversion was achieved at 260 °C by both Ce-Ni EM 1:2 and La-Ni EM 1:2.

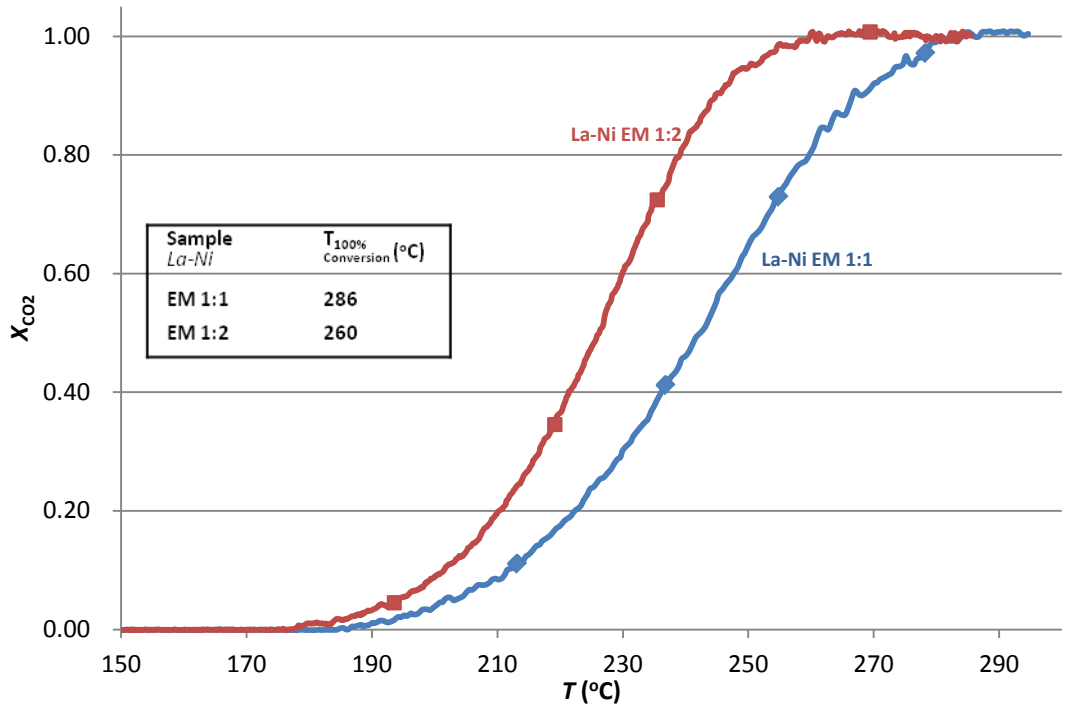


Figure 61: Catalytic performances of La-Ni samples.

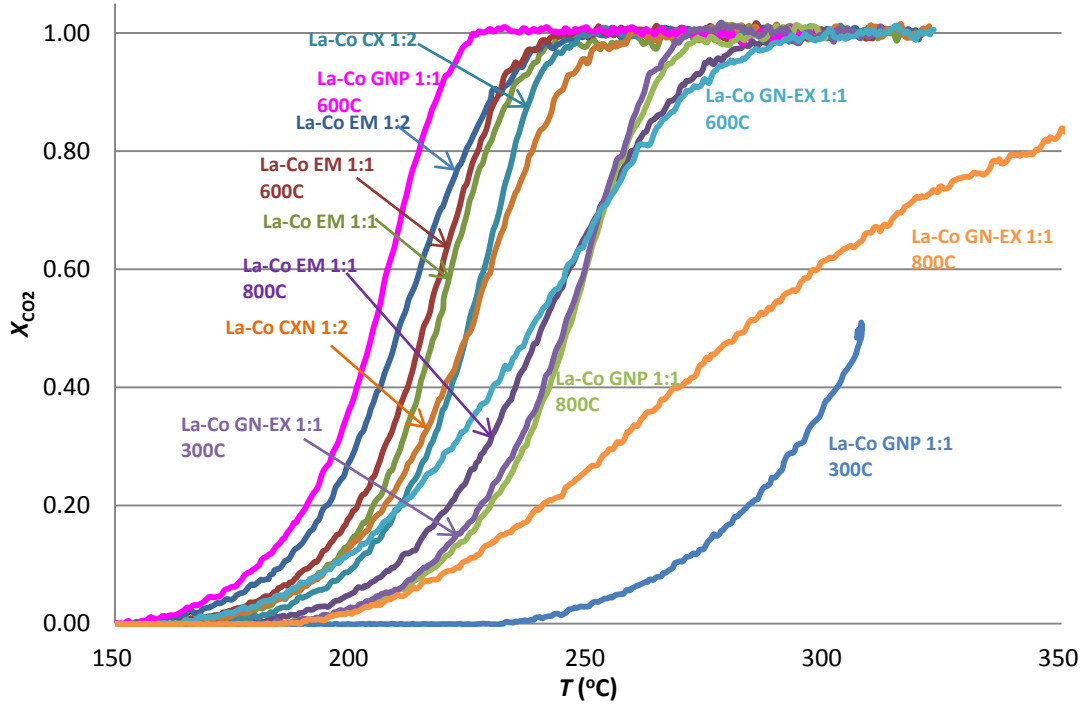


Figure 62: Catalytic performances of La-Co samples.

Figure 62 shows the catalytic results of all tested La-Co samples. Samples, La-Co GNP 1:1 300C and La-Co GN-EX 1:1 800ºC, showed unsatisfactory catalytic performances below 350 ºC.

With the exceptions of these samples, all other tested materials could catalyze the oxidation reaction of ethyl acetate to full conversion, as shown in Figure 63.

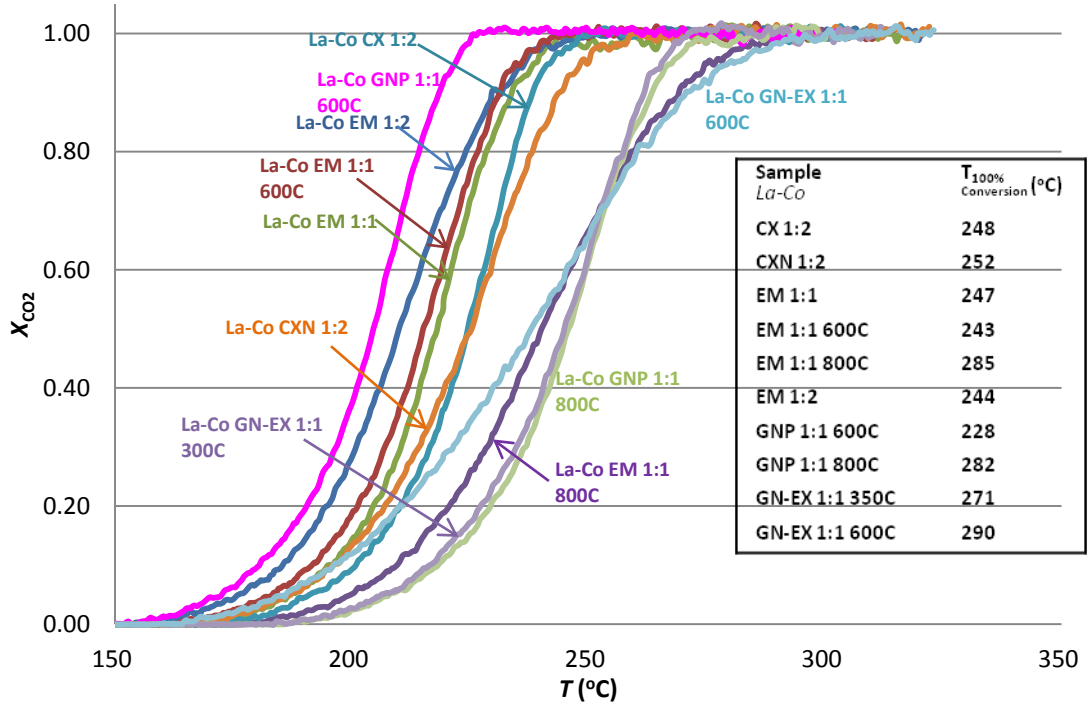


Figure 63: Catalytic performances of selected La-Co samples.

Samples prepared at higher temperatures showed relatively lower activities, however, exceptions were observed with La-Co GNP 1:1 600C and La-Co EM 1:1 600C. In fact, the best catalytic performance of La-Co samples was found for the GNP 1:1 material calcined at 600 ºC, being full conversion achieved at 228 ºC. La-Co EM 1:1 600C, resembling the La-Cu system, also had better catalytic activity than the corresponding EM sample calcined at 300 ºC. These could possibly be due to the phase transformation into perovskite-type oxides, as detected by XRD and TPR. The EM 1:2 sample could catalyze the oxidation reaction to full conversion at a lower temperature than the 1:1 sample. Unlike in Ce-Co system, the material prepared with CXN was less active than the material prepared with CX. Although larger BET surface areas were obtained in the GN-EX 1:1 350 ºC and 600 ºC samples, and although the $LaCoO_3$ perovskite structure was formed at 600 ºC, the catalytic activities of these two samples

were far less competitive than those of the EX, GNP or EM samples. The catalytic performances of La-Co samples could be ranked in the following order: GNP 1:1 600C > EM 1:1 600C > EM 1:2 > EM 1:1 > CX 1:2 > CXN 1:2 > GN-EX 1:1 350C > GNP 1:1 800C > EM 1:1 800C > GN-EX 1:1 600C.

The best catalytic performance of lanthanum-containing materials was found for the La-Co GNP 1:1 600C, with 100% conversion being achieved at 228 $^{o}$C. EM led to more active materials than EX in the La-Co system, whereas a different trend was found for the La-Cu system. In EM samples, materials with a higher content of transition metal showed better catalytic results than the mixed oxides consisting of equal portions of lanthanum and transition metal. A similar tendency was also observed with the exotemplated La-Cu samples. In both La-Co and La-Cu EM, the materials prepared at 600 $^{o}$C showed better catalytic activities than the oxides synthesized at 300 $^{o}$C, probably due to the presence of the perovskite phase. A similar phenomenon could be observed for the La-Co GNP samples, where the 300 ºC material failed to catalyze ethyl acetate oxidation to full conversion, while the 600 ºC sample was the best lanthanum-containing catalyst among all tested materials. No attractive catalytic performance was shown for the 800 ºC samples. Also poor activity was observed for the GN-EX samples although a perovskite structure was found for these materials. The catalytic performances of the lanthanum-containing samples can be arranged in the following order: La-Co GNP 1:1 600C > La-Co EM 1:1 600C > La-Co EM 1:2 > La-Co EM 1:1 > La-Co CX 1:2 > La-Co CXN 1:2 > La-Ni EM 1:2 > La-Co GN-EX 1:1 350C > La-Co GNP 1:1 800C > La-Co EM 1:1 800C > La-Ni EM 1:1 > La-Co GN-EX 1:1 600C > La-Cu CX 1:2 > La-Cu EM 1:1 600C > La-Cu CX 1:1 > La-Cu EM 1:2 > La-Cu EM 1:1.

#### 3.2.2.3. Comparison of Selected Samples

In both cerium-containing and lanthanum-containing systems, coupling with cobalt led to most active and selective materials. In all binary metal systems, cerium-containing samples tend to have better catalytic performances than the respective lanthanum-containing materials. Ni was a less attractive option of coupling transition metal in the cerium-containing system, whereas it was more compatible with lanthanum than with copper. With the exception of the La-Cu system, all EM materials showed higher activities than the corresponding EX samples. For both EM and EX materials, the 1:2

samples could catalyze the oxidation reaction of ethyl acetate to full conversion at a lower temperature than their corresponding 1:1 samples, with the exceptions of the Ce-Cu and Ce-Ni systems where the 1:1 samples showed higher catalytic activities. These two differences might be due to the enhancement of the reducibility of the transition metal species caused by $CeO_2$. Higher calcination temperature in material synthesis tends to decrease the catalytic activity of the material, however, reversed cases were observed in La-Cu and La-Co systems, which may be attributed to the possible phase transformation, with the presence of $La_2CuO_3$ detected by XRD in La-Cu EM 1:1 600C and $LaCoO_3$ with distorted perovskite structure in La-Co EM 1:1 600C. Fifteen samples in total were obtained, with ability to catalyze the oxidation reaction of ethyl acetate to 100% conversion below 260 $^oC$; their catalytic activities follow the sequence shown below:

Ce-Co EM 1:2 (225 $^oC$) > Ce-Co EM 1:1 (226 $^oC$) > La-Co GNP 1:1 600C (228 $^oC$)> Ce-Cu EM 1:1 (232 $^oC$)> Ce-Cu EM 1:2 (233 $^oC$)> Ce-Co CXN 1:2 (236 $^oC$)> Ce-Cu CX 1:1 (239 $^oC$)> Ce-Cu CX 1:2 (242 $^oC$)> La-Co EM 1:1 600C (243 $^oC$)> La-Co EM 1:2 (244 $^oC$)> La-Co EM 1:1 (247 $^oC$)> La-Co CX 1:2 (248 $^oC$)> Ce-Co CX 1:2 = Ce-Ni EM 1:1 (250 $^oC$)> La-Co CXN 1:2 (252 $^oC$).

### 3.2.3. Conclusions

The largest BET surface area obtained among all mixed-oxide materials prepared in this work was 211 $m^2/g$ for the Ce-Ni EM 1:2 sample. However, this material did not show much catalytic activity in the oxidation of ethyl acetate. With the exception of this sample, materials with larger surface areas were achieved by EX. In general, cerium-containing materials had larger BET values than lanthanum-containing samples. Apart from the Ce-Cu system, the 1:2 samples had larger surface areas than the corresponding 1:1 samples. The use of higher calcination temperatures in material preparation process tends to decrease the surface area, with the exceptions in La-Cu EM 1:1 600C and La-Co GNP 1:1 600C. This could be due to the formation of different phases in the 600 $^oC$ samples as the presence of $La_2CuO_4$ phase was confirmed by XRD and possible phase transformation could occur in La-Co GNP 1:1 600C although XRD showed a very amorphous spectrum for this sample. $La_2CuO_4$ with CuO and perovskite $LaCoO_3$ were detected by XRD in the corresponding samples calcined at higher temperature. However, lower catalytic activities were observed in these two samples

prepared at 800 $^{o}$C. This is probably ascribed to the presence of a small amount of $La_2O_2CO_3$ as a catalytic promoter in the 600 $^{o}$C materials, although its presence could not be proved by XRD in the La-Co sample, due to the amorphous spectrum. However, $La_2O_2CO_3$ is a common impurity found in perovskite materials by many scientists [65, 74-76]. In spite of the formation of $La_2CuO_4$ in La-Cu EM samples, no exceptional catalytic activities were found in these oxides. However, as reported in literature [77-79], the thermal, electrical and magnetic properties of these materials are still worth further investigation. The best catalytic performance for ethyl acetate oxidation was found in Ce-Co samples prepared by EM. La-Co GNP 1:1 600C also showed a competitive catalytic activity for this reaction although no remarkable BET value was obtained in this material.

Solid solutions, namely perovskite-type ($ABO_3$) and $K_2NiF_4$-type structures were observed in lanthanum-containing samples, but not in cerium-containing samples. The reason for this could be explained by the following equation:

$$t = \frac{R_A + R_O}{\sqrt{2}(R_B + R_O)},$$

where *R* represents the ionic radius of the A, B, or oxide ion and *t* is the tolerance factor.

The perovskite structure can be formed if the tolerence factor, *t*, falls in the range between 0.8 and 1.0 [80]. As perovskite structure requires the occupation of a larger ion on the A site-usually rare earth, alkaline earth, alkali and other large ions such as $Pb^{2+}$ and $Bi^{3+}$ that fit into the dodecahedral site of the framework-and a smaller one on the B site from 3d, 4d and 5d transitional metal ions which occupy the octahedral sites [80], a system with a tolerance factor closer to 1 is more comparable to such crystal structure. A tolerance factor equal to 1 corresponds to the formation of the ideal cubic perovskite with the best stability [81]. With a decrease in the tolerance factor, accordingly an increase in the structural distortion, stability of the material tends to drop, which, on the other hand, is related to the aggravation of obstruction in the formation of such structure.

The radii of the ions involved in this work for the preparation of mixed oxides are listed in Table 15.

Table 15: Ionic radii of selected ions.

| Ion | Ionic radius (Å) |
|---|---|
| $Ce^{4+}$ | 0.97 |
| $La^{3+}$ | 1.32 |
| $Cu^{2+}$ | 0.73 |
| $Ni^{2+}$ | 0.60 |
| $Co^{3+}$ | 0.56 |
| $O^{2-}$ | 1.40* |

All data are taken from [80], with the exception of data marked with * that was taken from [82].

The obtained tolerance factors are 0.83 for both Ce-Co and Ce-Ni systems, 0.79 for Ce-Cu system, 0.90 for La-Cu system and 0.96 for La-Co system. Thus, perovskite-type structure can be formed more easily in lanthanum-containing materials than in cerium-containing system. This can also provide the possible explanation why $ABO_3$ perovskite was found in the La-Co system, whereas a $K_2NiF_4$-type structure was formed in the La-Cu system, as $La_2CuO_4$ is more stable than $LaCuO_3$ [71].

### 3.3. Toluene Oxidation

Ten out of the fifteen samples with the capability of catalyzing the oxidation reaction of ethyl acetate to 100% conversion below 260 $^oC$ were selected for further tests in toluene oxidation: Ce-Co EM 1:2, Ce-Co CX 1:2, Ce-Co CXN 1:2, Ce-Cu EM 1:1, Ce-Cu CX 1:1, La-Co EM 1:1, La-Co EM 1:1 600C, La-Co GNP 1:1 600C, La-Co CX 1:2, and La-Co CXN 1:2. No significant differences were observed between the two cycles of catalytic tests for each sample, except in exotemplated La-Co materials, where catalytic deactivation occurred after the increasing step in the 1$^{st}$ cycle. Figure 64 illustrates the example of CX templated La-Co. The full conversion of toluene to water and carbon dioxide, catalyzed by this sample in the 1$^{st}$ increasing step, was achieved at about 363 $^oC$; however, it was 388 $^oC$ in the 2$^{nd}$ cycle.

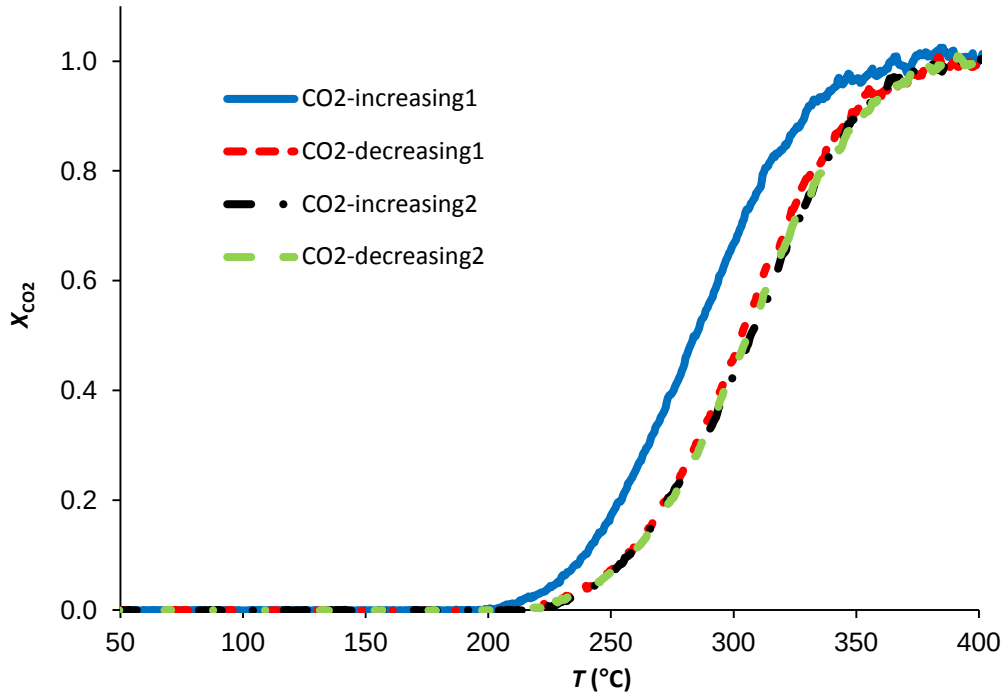


Figure 64: Two cycles of catalytic performance of La-Co CX 1:2 for toluene oxidation.

The Ce-Co mixed oxides had the best catalytic performances in toluene oxidation among all ten samples (Figure 65). Surprisingly, unlike in ethyl acetate oxidation, both EX Ce-Co materials were more active than the EM sample in the oxidation of toluene. Ce-Co made with CXN achieved the full conversion of toluene into $H_2O$ and $CO_2$ almost at a 10 $^oC$ lower temperature than the corresponding EM material. As for ethyl acetate oxidation, La-Co GNP 1:1 600$^oC$ had higher catalytic activity than the other La-Co samples. However, the La-Co prepared by EM at 600 $^oC$ lost its advantage over the corresponding material calcined at 300 $^oC$ in the catalytic oxidation reaction of toluene, which may have resulted from some rupture in the distorted perovskite structure in the 600 $^oC$ sample. La-Co EM 1:1 was found out to have even better activity than the EX Ce-Cu 1:1 sample. However, the EX La-Co samples required much higher temperatures for the oxidation of toluene, with the failure of CXN templated sample in catalyzing the reaction to full conversion within the temperature range studied. With the exception of La-Co prepared with CX, all other materials showed good $CO_2$ selectivity in redox catalysis for toluene oxidation.

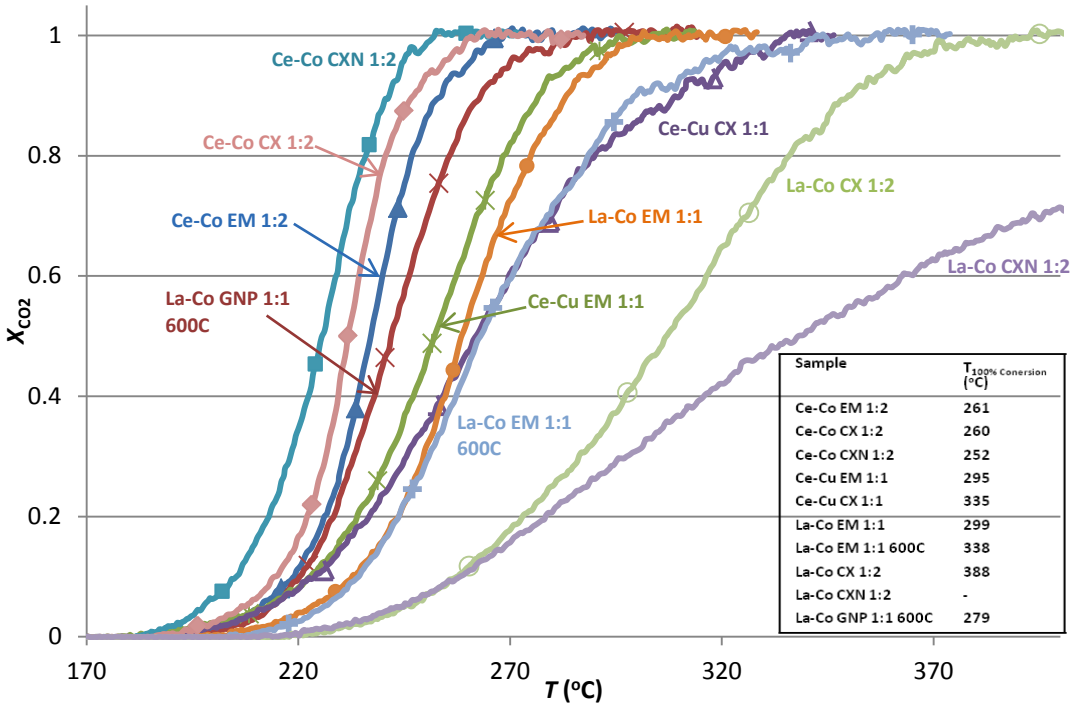


Figure 65: Catalytic performances of selected samples for toluene oxidation.

Therefore, the catalytic performances of the ten selected samples for toluene oxidation showed the following ranking:

Ce-Co CXN 1:2 > Ce-Co CX 1:2 > Ce-Co EM 1:2 > La-Co GNP 1:1 600C > Ce-Cu EM 1:1 > La-Co EM 1:1 > Ce-Cu CX 1:1 > La-Co EM 1:1 600C > La-Co CX 1:2 > La-Co CXN 1:2.

## 4. General Conclusions

This work aimed at the preparation of catalytically active metal oxides for VOCs abatement. Results showed that loading with gold nanoparticles or exotemplating with CX could improve the catalytic activity of single metal oxides. Due the absence of ashes, CX was found to be a better templating material than CROX. The best catalytic performance of single oxides on ethyl acetate oxidation was found for CX templated CuO. Lower temperatures were substantially required for the mixed metal oxides to catalyse the oxidation reactions, in comparision to the single oxides. Extraordinary catalytic activity was observed for Ce-Co samples on both ethyl acetate and toluene oxidations: EM samples showed better performance in the oxidation of ethyl acetate

(full conversion achieved at about 225 $^{o}$C), whereas EX materials were more suitable for toluene (full conversion achieved at about 252 $^{o}$C). Generally, better reactivity was observed in ethyl acetate than in toluene. La-Co oxide prepared by GNP at 600 $^{o}$C also had a competitive activity in the oxidation reaction of these two VOCs, which may result from the presence of a different phase; however, this could not be confirmed as an amorphous spectrum was obtained by XRD. Perovskite $LaCoO_3$ was successively obtained and confirmed by XRD in samples calcined at 800 $^{o}$C, also in EM and GN-EX materials prepared at 600 $^{o}$C. All materials required a temperature higher than 250 $^{o}$C for ethyl acetate oxidation, with the exception of La-Co EM 1:1 600C. This probably is due to the presence of $La_2O_2CO_3$ in La-Co EM 1:1 600C, which enhanced the catalytic performance of this sample, whereas nearly pure perovskite $LaCoO_3$ was detected in the other samples. A solid solution, $La_2CuO_4$ with $K_2NiF_4$-type structure, was obtained in La-Cu EM sample. Even though no exceptional catalytic performances were observed for the obtained perovskite-type $LaCoO_3$ and $K_2NiF_4$-type $La_2CuO_4$, the thermal, electrical and magnetic properties of these materials are still worth further investigation.

In this work, prepared materials were only tested on the catalytic oxidation of a single VOC. However, industrial effluents in real life commonly are mixtures of several substances. Therefore, further study of the catalytic activities of these materials on the binary- or ternary-VOC system would be necessary for future work.

## References


1. Tucker, W.G., Volatile Organic Compounds, in Indoor Air Quality Handbook. 2004, Digital Engineering Library @ McGraw-Hill.
2. Council Directive1999/13/EC on limitation of emissions of volatile organic compounds due to the use of organic solvents in certain activities and installations. 1999: Official Journal of the European Communities.
3. Khan, F.I. and A.K. Ghoshal, Removal of Volatile Organic Compounds from polluted air. Journal of Loss Prevention in the Process Industries, 2000. **13**: p. 527-545.
4. The Clean Air for Europe (CAFE) Programme: Towards a Thematic Strategy for Air Quality. 2001, Comission of the European Communities: Brussels.
5. Forster, P., et al., Changes in Atmospheric Constituents and in Radiative Forcing. In: Climate Change 2007: The Physical Science Basis. Contribution of Working Group I to the Fourth Assessment Report of the Intergovernmental Panel on Climate Change [Solomon, S., D. Qin, M. Manning, Z. Chen, M. Marquis, K.B. Averyt, M.Tignor and H.L. Miller (eds.)]. Cambridge University Press, Cambridge, United Kingdom and New York, NY, USA. 2007.
6. Commission, E. The Montreal Protocol, Office for Official Publications of the European Communities, 2007, European Communities: Luxembour.
7. Carabineiro, S.A.C. and D.T. Thompson, Catalytic Applications for Gold Nanotechnology, in Nanocatalysis, U. Heiz and U. Landman, Editors. 2007, Springer Berlin Heidelberg. p. 377-489.
8. Directive 2001/81/EC on national emission ceilings for certain atmospheric pollutants. Official Journal of the European Communities, 2001.
9. Thematic Strategy on air pollution, in Communication from the Commission to the Council and the European Parliament. 2005, Commission of the European Communitie: Brussels.
10. National Emission Ceilings. February 23, 2012 [cited 2012 April 1]; Available from: http://ec.europa.eu/environment/air/pollutants/ceilings.htm.
11. Moretti, E.C., Reduce VOC and HAP Emissions, in CEP magazine. 2002, CEP magazine. p. 30-40.

12. Integrated Pollution Prevention and Control, in Reference Document on Best Available Techniques in Common Waste Water and Waste Gas Treatment / Management Systems in the Chemical Sector. 2003, European Commission.
13. Bastos, S.S.T., et al., Total oxidation of ethyl acetate, ethanol and toluene catalyzed by exotemplated manganese and cerium oxides loaded with gold. Catalysis Today, 2012. **180**(1): p. 148-154.
14. Ojala, S., et al., Durability of VOC catalysts in solvent emission oxidation. Chemical Engineering Journal, 2006. **120**(1-2): p. 11-16.
15. Solsona, B., et al., Promoting the activity and selectivity of high surface area Ni–Ce–O mixed oxides by gold deposition for VOC catalytic combustion. Chemical Engineering Journal, 2011. **175**: p. 271-278.
16. Minicò, S., et al., Catalytic combustion of volatile organic compounds on gold/iron oxide catalysts. Applied Catalysis B: Environmental, 2000. **28**: p. 245-251.
17. Centeno, M.A., et al., Catalytic combustion of volatile organic compounds on Au/CeO2/Al2O3 and Au/Al2O3 catalysts. Applied Catalysis A: General, 2002. **234**(1-2): p. 65-78.
18. Huang, Y.-C., et al., Improved Removal of Indoor Volatile Organic Compounds by Activated Carbon Fiber Filters Calcined with Copper Oxide Catalyst. CLEAN - Soil, Air, Water, 2010. **38**(11): p. 993-997.
19. Pooperasupong, S., B. Caussat, and S. Damronglerd, Air Pollution Control by Oxidation of Aromatic Hydrocarbon over Supported Metal Oxide. ScienceAsia, 2008. **34**(1): p. 119.
20. Albonetti, S., et al., Catalytic combustion of toluene over cluster-derived gold/iron catalysts. Applied Catalysis A: General, 2010. **372**(2): p. 138-146.
21. Heynderickx, P.M., et al., The total oxidation of propane over supported Cu and Ce oxides: A comparison of single and binary metal oxides. Journal of Catalysis, 2010. **272**(1): p. 109-120.
22. Garcia, T., B. Solsona, and S.H. Taylor, The oxidative destruction of hydrocarbon volatile organic compounds using palladium–vanadia–titania catalysts. Catalysis Letters 2004. **97**: p. 99-103.
23. Wyrwalski, F., et al., Influence of the Ethylenediamine Addition on the Activity, Dispersion and Reducibility of Cobalt Oxide Catalysts Supported over ZrO2 for Complete VOC Oxidation. Catalysis Letters, 2006. **108**(1-2): p. 87-95.

24. Bastos, S.S.T., et al., Manganese oxide catalysts synthesized by exotemplating for the total oxidation of ethanol. Applied Catalysis B: Environmental, 2009. **93**(1-2): p. 30-37.
25. Heneghan, C.S., G.J. Hutchings, and S.H. Talor, The destruction of volatile organic compounds by heretoheneous catalytic oxidation. Catalysis 2004. **17**: p. 105-151.
26. Delimaris, D. and T. Ioannides, VOC oxidation over CuO–CeO2 catalysts prepared by a combustion method. Applied Catalysis B: Environmental, 2009. **89**(1-2): p. 295-302.
27. Delimaris, D. and T. Ioannides, VOC oxidation over MnOx–CeO2 catalysts prepared by a combustion method. Applied Catalysis B: Environmental, 2008. **84**(1-2): p. 303-312.
28. Zengjian, Z., W. Hui, and G. Guofeng, Catalytic Combustion of Methyl Acetate over Cu-Mn Mixed Oxide Catalyst. 2011: p. 1994-1997.
29. Kieûlinga, D., et al., Perovskite-type oxides - catalysts for the total oxidation of chlorinated hydrocarbons. Applied Catalysis B: Environmental, 1998(19): p. 143-151.
30. Merino, N.A., et al., Synthesis, characterisation, catalytic activity and structural stability of LaCo1−yFeyO3±λ perovskite catalysts for combustion of ethanol and propane. Journal of Catalysis, 2006. **240**(2): p. 245-257.
31. Seiyama, T., Total Oxidation of Hydrocarbons on Perovskite Oxides. Catalysis Reviews, 1992. **34**(4): p. 281-300.
32. Santos, V.P., et al., Stability of a cryptomelane catalyst in the oxidation of toluene. Catalysis Today, 2010. **154**(3-4): p. 308-311.
33. Brown, M.E. and P.K. Gallagher, eds. Applications to Inorganic and Miscellaneous Materials. Handbook of Thermal Analysis and Calorimetry, ed. P.K. Gallagher. Vol. 2. 2003, Elsevier B.V.: Amsterdam.
34. Klabunde, K.J., et al., Nanocrystals as Stoichiometric Reagents with Unique Surface Chemistry. Journal of Physical Chemistry 1996. **100**(30): p. 12142-12153.
35. Jackson, S.D. and J.S.J. Hargreaves, eds. Metal oxide catalysis. Vol. 2. 2009, WILEY-VCH Verlag GmbH & Co. KGaA, Weinheim.

36. Schüth, F., Endo- and Exotemplating to Create High-Surface-Area Inorganic Materials. Angewandte Chemie International Edition, 2003. **42**(31): p. 3604-3622.
37. Carp, O., L. Patron, and E. Segal, Thermal Properties of Solid Coordination Compounds. IV. Revue Roumaine de Chimie, 2006. **51**(1): p. 5-12.
38. Yang, Y.-J., et al., Characteristics of lanthanum strontium chromite prepared by glycine nitrate process. Solid State Ionics, 2000(135): p. 475-479.
39. Perry, R.H., D.W. Green, and J.O. Maloney, eds. Perry's Chemical Engineers' Handbook. 7 ed. 1999, McGraw-Hill: New York.
40. Brown, M.E., ed. Principles and Practice. Handbook of Thermal Analysis and Calorimetry, ed. P.K. Gallargher. Vol. 1. 1998, Elsevier Science B.V.: Amsterdam.
41. Sing, K.S.W., et al., Reporting Physisorption Data for Gas/Solid Systems with Special Reference to the Determination of Surface Area and Porosity. Pure & Appl. Chem., 1985. **57**(4): p. 603-619.
42. Fierro, J.L.G., ed. Metal Oxides Chemistry and Applications Chemical Industries, ed. H. Heinemann. 2006, CRC Press,Taylor & Francis Group: Berkeley.
43. Niemantsverdriet, J.W., Spectroscopy in Catalysis 3ed. 2007: WILEY-VCH Verlag GmbH & Co. KGaA.
44. Fitzpatrick, L.E., et al., eds. Encyclopedia of Materials Characterization. Materials Characterisation Series, ed. C.R. Brundle and J. Charles A. Evans. 1992, Butxetworch-Heinemann, a division of Reed Publishing (USA) Inc.
45. Schwickardi, M., et al., High-Surface-Area Oxides Obtained by an Activated Carbon Route. Chemistry of Materials, 2002. **14**(9): p. 3913-3919.
46. Job, N., et al., Porous carbon xerogels with texture tailored by pH control during sol-gel process. Carbon, 2004. **42**(3): p. 619-628.
47. Gobin, O.C., High-Throughput Reactor Automatization and Multi-objective Optimization of deNOx Catalysts, in Chemical Engineering. 2007, Munich University of Technology: Munich.
48. Carabineiro, S.A.C., et al., Adsorption of ciprofloxacin on surface-modified carbon materials. Water Research, 2011. **45**(15): p. 4583-4591.
49. Bowker, M., A. Nuhu, and J. Soares, High activity supported gold catalysts by incipient wetness impregnation. Catalysis Today, 2007. **122**(3-4): p. 245-247.
50. Carabineiro, S.A.C., et al., Nanostructured iron oxide catalysts with gold for the oxidation of carbon monoxide. RSC Advances, 2012. **2**(7): p. 2957.

51. Bastos, S.d.S.T., Preparação de Catalisadores por Exotemplating para a Oxidação de Compostos Orgânicos Voláteis. 2009, Instituto Superior de Engenharia do Porto.
52. Carabineiro, S.A.C., et al., Comparison between activated carbon, carbon xerogel and carbon nanotubes for the adsorption of the antibiotic ciprofloxacin. Catalysis Today, 2012(in press).
53. Carabineiro, S.A.C., et al., Gold supported on metal oxides for carbon monoxide oxidation. Nano Research, 2010. **4**: p. 180-193.
54. Carabineiro, S.A.C., et al., Exotemplated ceria catalysts with gold for CO oxidation. Applied Catalysis A: General, 2010. **381**(1-2): p. 150-160.
55. Lau, H.H., Characterisation of Copper (II) Oxide Synthesised by Precipitation Method, in Faculty of Science. 2005, Universiti Putra Malaysia.
56. Iheva, L.I., D.H. Andreeva, and A.A. Andreev, TPR and TPD investigation of Au/o~-Fe203. Thermochimica Acta, 1997. **292**: p. 169-174.
57. Neri, G., et al., Au/iron oxide catalysts: temperature programmed reduction and X-ray diffraction characterization. Thermochimica Acta, 1999. **329**: p. 39-46.
58. Milone, C., et al., Selective hydrogenation of α,βα,β-unsaturated ketone to α,βα,β-unsaturated alcohol on gold-supported iron oxide catalysts: Role of the support. Journal of Catalysis, 2005. **236**(1): p. 80-90.
59. Milone, C., et al., A comparative study on the selective hydrogenation of α,β unsaturated aldehyde and ketone to unsaturated alcohols on Au supported catalysts. Catalysis Today, 2007. **122**(3-4): p. 341-351.
60. Solsona, B., et al., Supported gold catalysts for the total oxidation of alkanes and carbon monoxide. Applied Catalysis A: General, 2006. **312**: p. 67-76.
61. Aeijeltsaverinksilberova, B., et al., DRIFTS study of the water–gas shift reaction over Au/Fe2O3. Journal of Catalysis, 2006. **243**(1): p. 171-182.
62. Khoudiakov, M., M.C. Gupta, and S. Deevi, Au/Fe2O3 nanocatalysts for CO oxidation: A comparative study of deposition–precipitation and coprecipitation techniques. Applied Catalysis A: General, 2005. **291**(1-2): p. 151-161.
63. Forzatti, P. and L. Lietti, Catalyst deactivation. Catalysis Today, 1999. **52**: p. 165-181.
64. Ivas, T., et al., Phase diagram of CeO2–CoO for nano-sized powders. Calphad, 2012. **36**: p. 57-64.

65. Abboudi, M., et al., Synthesis of CuO, La2O3, and La2CuO4 by the Thermal-Decomposition of Oxalates Precursors Using a New Method. Synthesis and Reactivity in Inorganic, Metal-Organic, and Nano-Metal Chemistry, 2011. **41**(6): p. 683-688.
66. Bakiz, B., et al., Carbonatation and Decarbonatation Kinetics in the La2O3-La2O2CO3 System under CO2 Gas Flows. Advances in Materials Science and Engineering, 2010. **2010**: p. 1-6.
67. Hue, H.T.H. and N.D. Bang, Preparation and Characterization of Nanosized CuO-CeO2 Mixed Oxide with High Surface Area. e-Journal of Surface Science and Nanotechnology, 2011. **9**: p. 463-465.
68. Teng, F., et al., High combustion activity of CH4 and catalluminescence properties of CO oxidation over porous Co3O4 nanorods. Applied Catalysis B: Environmental, 2011. **110**: p. 133-140.
69. Merino, N., et al., LaCaCoO perovskite-type oxides: preparation, characterisation, stability, and catalytic potentiality for the total oxidation of propane. Journal of Catalysis, 2005. **231**(1): p. 232-244.
70. Arakawa, T., N. Ohara, and J. Shiokawa, Reduction of perovskite oxide LnCoO3(Ln=La-Eu) in a hydrogen atmosphere. Journal of Materials Science, 1986. **21**: p. 1824-1827.
71. Al Daroukh, M., Oxides of the AMO3 and A2MO4-type: structural stability, electrical conductivity and thermal expansion. Solid State Ionics, 2003. **158**(1-2): p. 141-150.
72. Tanaka, Y., et al., Water gas shift reaction over Cu-based mixed oxides for CO removal from the reformed fuels. Applied Catalysis A: General, 2003. **242**(2): p. 287-295.
73. Wei, Z.-X., et al., Combustion Synthesis and Catalytic Activity of LaCoO3for HMX Thermal Decomposition. Propellants, Explosives, Pyrotechnics, 2009. **34**(5): p. 394-399.
74. Wang, L., et al., Efficient synthesis of glycerol carbonate from glycerol and urea with lanthanum oxide as a solid base catalyst. Catalysis Communications, 2011. **12**(15): p. 1458-1462.
75. Lee, M.-J., et al., Catalytic Activities of Perovskite-type LaBO3 (B = Fe, Co, Ni) Oxides_La2O2CO3. Bull. Korean Chem. Soc., 2005. **26**(10).

76. Musialik-Piotrowska, A. and H. Landmesser, Noble metal-doped perovskites for the oxidation of organic air pollutants. Catalysis Today, 2008. **137**(2-4): p. 357-361.

77. Takamatsu, T., et al., Low-temperature synthesis of T′-La2CuO4 using CaH2 as reductant. Physica C: Superconductivity, 2011. **471**(21-22): p. 679-681.

78. Hess, C. and B. Buchner, Thermal conductivity of doped La2CuO4 as an example for heat transport by optical phonons in complex materials. The European Physical Journal B - Condensed Matter, 2004. **38**(1): p. 37-41.

79. Okajima, Y., M. Yamada, and K. Yamaya, Magnetic properties of La2CuO4 with slight amounts of excess oxygen. Physica C, 1997. **282-287**: p. 1319-1320.

80. Tejuca, L.G. and J.L.G. Fierro, eds. Properties and Applications of Perovskite-type Oxides. 1 ed. 1992, CRC Press.

81. Su, W.-F.A., Effects of additives on perovskite formation in sol-gel derived lead magnesium niobate. Materials Chemistry and Physics, 2000. **62**: p. 18-22.

82. Kityakarn, S., Preparation and Characterization of Nano-LaCoO3 Perovskite Oxidative Catalyst, in Department of Chemistry. 2005, Kasetsart University.

83. Carabineiro, S.A.C., et al., Gold nanoparticles supported on magnesium oxide for CO oxidation. Nanoscale Research Letters, 2011. **6**(1): p. 435-440.

# Appendices

## Appendix 1

1. Exotemplated Zinc, Magnesium and Lanthanum Oxides

1.1. Synthesis

For zinc oxides, 3 different carbon materials were used as templates: CX, CROX and NORIT GAC activated carbon (CGAC). The preparation procedure was similar to that described in Section 2.1.1. The temperature programs used for different exotemplated materials are in Table A1.

Table A1: Temperature programs used for the different templated materials impregnated with zinc precursor.

| Template material | Heating rate (ºC/min) | Intermediate *T* (ºC) | Final *T* (ºC) |
|---|---|---|---|
| CX | 2 | 250 | 400,450,500* |
| CROX | 2 | 250 | 500,550* |
| CGAC | 2 | 250 | 450 |

*final temperature was increased in calcining the material.

For magnesium oxides and lanthanum oxides, the same procedure was followed. However, only CX with particle size less than 0.1 mm was employed. The temperature programs used are shown in Table A2.

Table A2: Temperature programs used for magnesium oxides and lanthanum oxides made with CX.

| | Heating rate (ºC/min) | Intermediate *T* (ºC) | Final *T* (ºC) |
|---|---|---|---|
| Magnesium oxides | 2 | 250 | 550 |
| Lanthanum oxides | 2 | 250 | 400 |

## 1.2. Results of BET Surface Area

Table A3 shows the BET surface areas of exotemplated ZnO, MgO and $La_2O_3$. The values of zinc and lanthanum oxides prepared by EX were not significant. Larger surface areas were obtained for magnesium oxides. EX improved the surface areas of MgO and $La_2O_3$, in comparison with the respective commercial samples. No obvious tendency could be observed in relation with one impregnation or two impregnations used in the synthesis of these oxides. However, it seems that surface area is lower when more calcination was applied in material preparation.

Table A3: BET surface areas of selected samples.

| sample | ID | BET surface area ($m^2/g$) |
|---|---|---|
| ZnO | ZnO CX 1IMP 500C | 19 |
| | ZnO CX 1IMP 450C | 13 |
| | ZnO CROX 1IMP 550C | 27 |
| | ZnO CROX 2IMP 500C | 32 |
| | ZnO CGAC 1IMP 450C | 28 |
| | ZnO CGAC 2IMP 450C | 17 |
| MgO | MgO CX 2IMP 1CALC | 71 |
| | MgO CX 2IMP 2CALC | 56 |
| | MgO commercial (Merck)** | 32 |
| La2O3 | La2O3_CX_1IMP_5CALC | 30 |
| | La2O3 commercial (Aldrich)* | 11 |

* - Values taken from [53]
**- Value taken from [83]

The resulted ZnO and MgO obtained by EX had a small particle size, which caused very high drop pressure on the VOC set-up during the catalytic tests, and therefore no catalytic results of these samples were obtained, neither further characterization was carried out.

## 2. Gold Loaded MgO, $La_2O_3$ and $Y_2O_3$ Samples

### 2.1. TPR

The following Figures show the TPR spectra of the commercial metal oxides (MgO, $La_2O_3$ and $Y_2O_3$) and the gold loaded samples, which were obtained by Dr. Sónia Carabineiro in previous works [50, 53]. The TPR curve of exotemplated $La_2O_3$ is also shown for comparison.

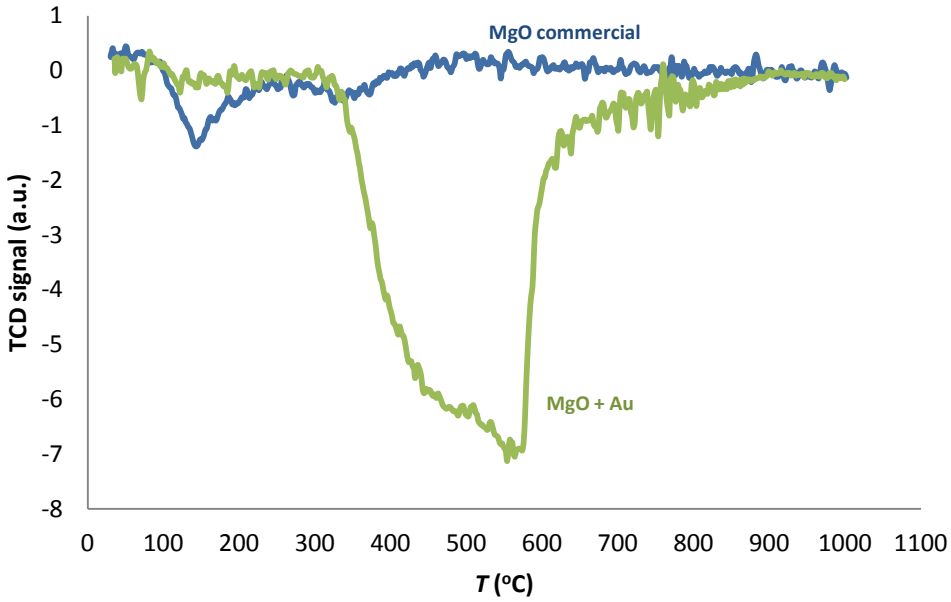


Figure A1: TPR of commercial MgO alone and loaded with Au.

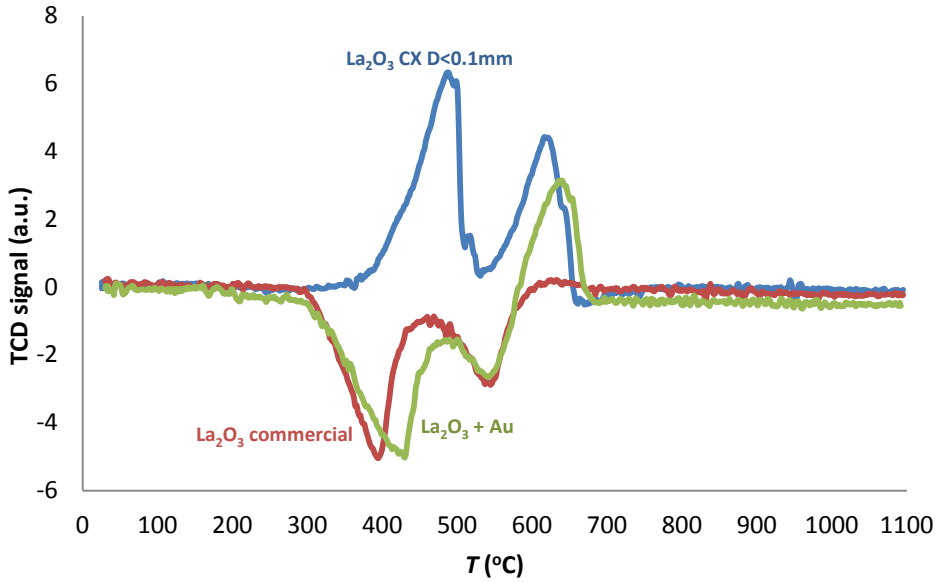


Figure A2: TPR of commercial La2O3 alone and loaded with Au, and prepared by EX.

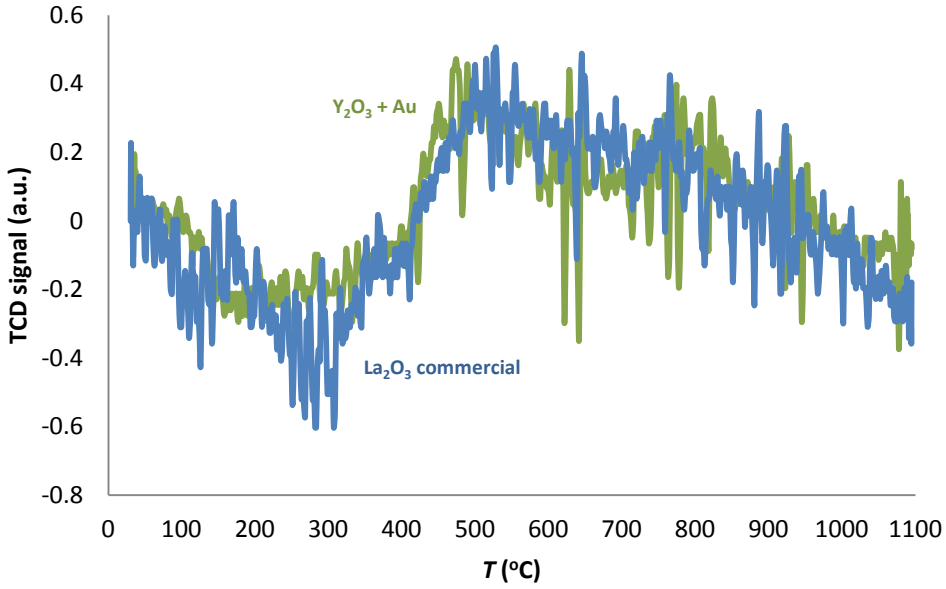


Figure A3: TPRs of commercial $Y_2O_3$ alone and loaded with Au..

Negative peaks appeared in the TPR spectra of commercial and gold loaded MgO and $La_2O_3$ (Figures A1 and A2), which resulted from the presence of corresponding hydroxides phases ($Mg(OH)_2$ and $La(OH)_3$, respectively) instead of desired oxides, as detected by XRD in previous works [53, 83]. This is the reason why the TPR profile of exotemplated $La_2O_3$ showed a completely different tendency from the other two samples. In the case of $Y_2O_3$, the TPR spectrum of the gold loaded oxide resembled that of the commercial sample.

## 2.2. Catalytic Performances

Figure A4 demonstrates the catalytic performances of gold loaded MgO, $La_2O_3$ and $Y_2O_3$ on the oxidation of ethyl acetate, together with the results of gold doped copper, nickel, iron and zinc oxides for comparison. Au/CuO showed the best catalytic performance. Full conversion of VOC into $CO_2$ was achieved for this catalyst at 289 °C, followed by Au/NiO at 327 °C, $Au/Y_2O_3$ at 369 °C and $Au/La_2O_3$ at 429 °C. However, reactions catalyzed by $Au/Fe_2O_3$ and Au/ZnO did not reach 100% conversion, as formation of CO was detected.

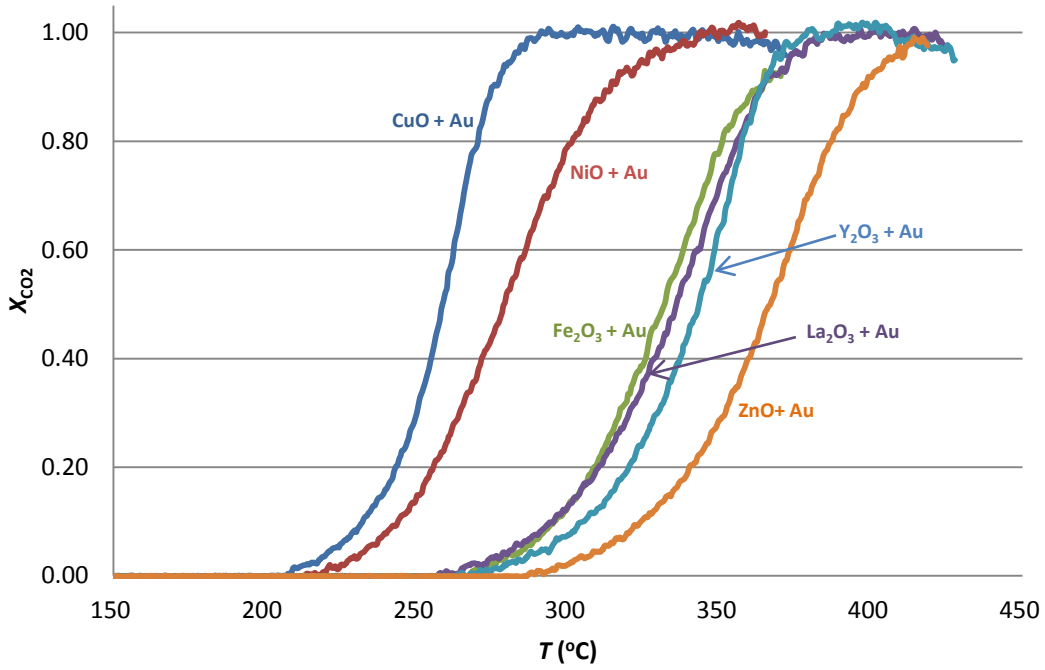


Figure A4: VOC conversion into $CO_2$ catalyzed by commercial oxides loaded with Au.

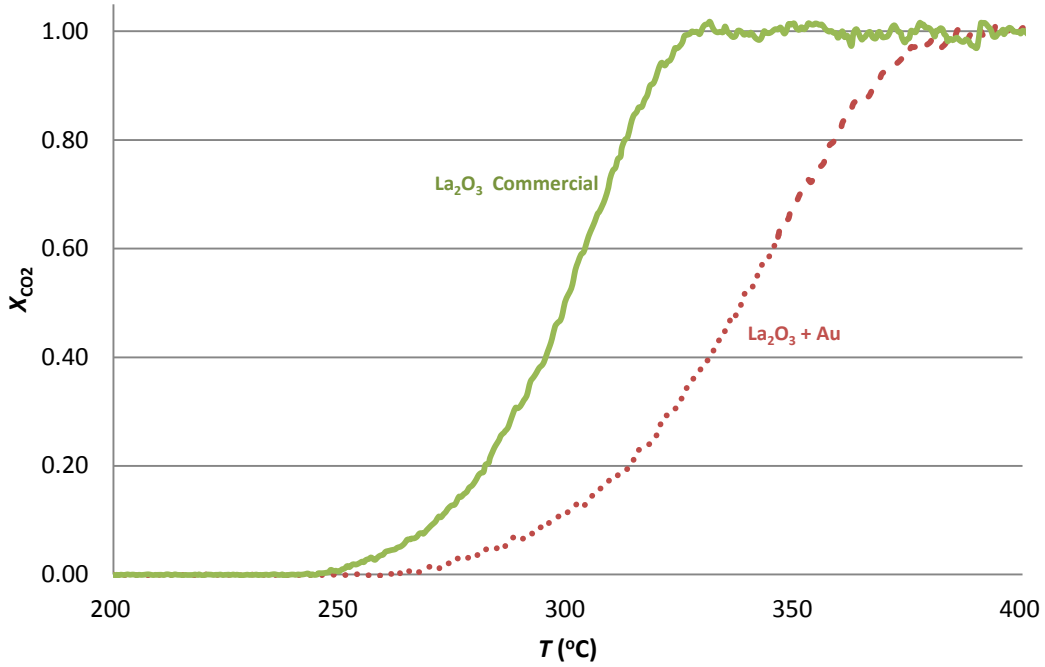


Figure A5: VOC conversion into $CO_2$ catalyzed by the $La_2O_3$ materials.

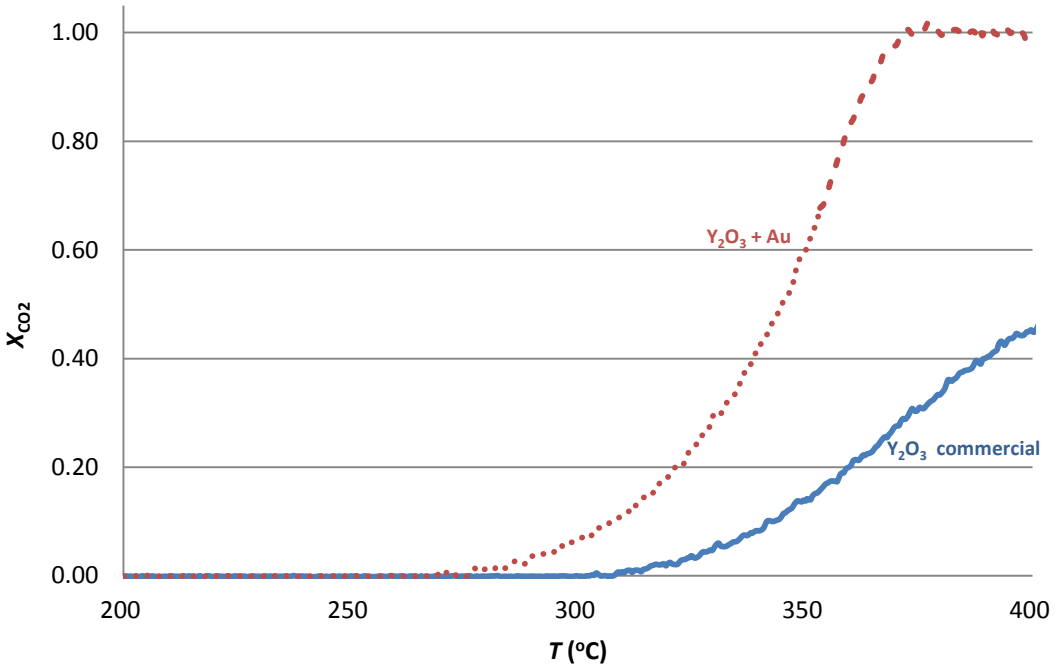


Figure A6: VOC conversion into $CO_2$ catalyzed by the $Y_2O_3$ materials.

Figures A5 and A6 show the comparison of the catalytic performances of commercial $La_2O_3$ and $Y_2O_3$ alone or loaded with gold. Au/oxides are expected to be more active in the oxidation reactions [7, 13, 50, 53, 54]. This occurred with the yttrium and lanthanum samples, although commercial lanthanum oxide could achieve full decomposition of ethyl acetate at lower temperatures than the gold loaded sample, however a small amount of CO was detected, which did not happen with the gold loaded sample, as 100% conversion of ethyl acetate to carbon dioxide, without CO formation was obtained.

## 3. La-Fe

The La-Fe 1:1 sample was prepared following the evaporation method described in Section 2.2.1.2., a BET surface area of 72 $m^2/g$ being obtained. The TPR spectrum of this sample is shown in Figure A7, together with commercial iron oxide and exotemplated lanthanum oxide, for comparison. The first peak in the La-Fe sample probably represents the reduction iron oxide, which appeared at a higher temperature in the TPR spectrum of the commercial iron oxide. The two small peaks after the main peak in the La-Fe sample might be related to the presence of $La_2O_3$ phase in the material, which also shifted the spectrum to slight higher temperatures, compared with

the exotemplated $La_2O_3$. However, the phase composition of this material should be confirmed by XRD analysis. All reduction peaks of this sample occurred at higher temperatures than in the single oxides. This might be due to the cetrimide additive present in the ethanol used in the preparation process.

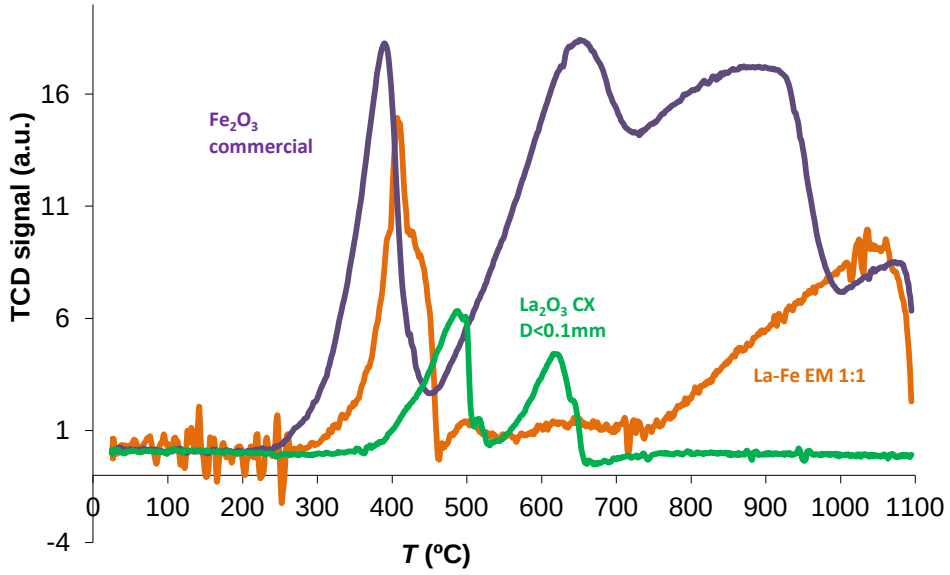


Figure A7: TPR of La-Fe 1:1 EM and of commercial iron oxide and exotemplated lanthanum oxide for comparison.

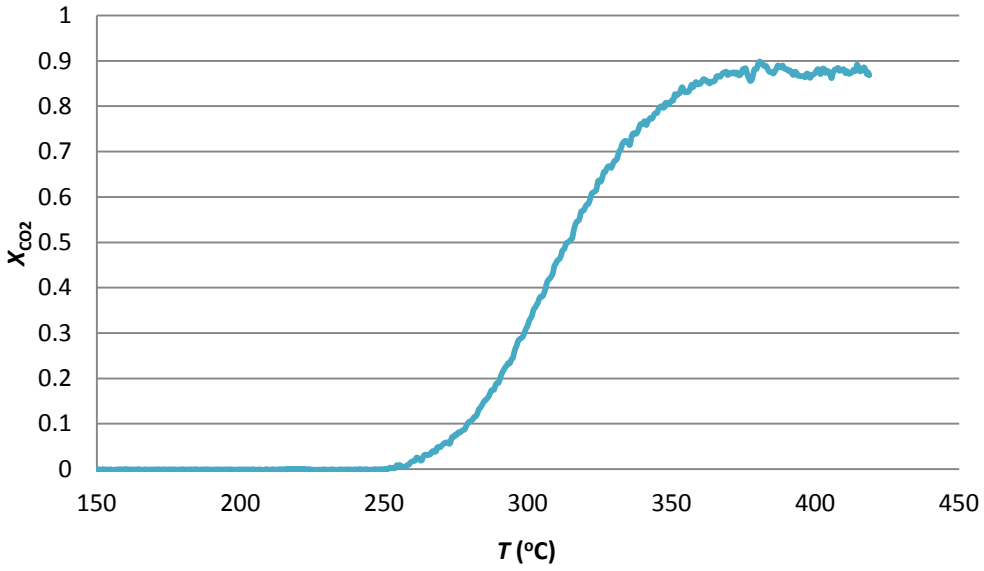


Figure A8: Catalytic performance of La-Fe EM 1:1.

The catalytic result on ethyl acetate oxidation of this material is shown in Figure A8. Contrary to expectations, the maximum conversion achieved was only about 88%.

## 4. Two Cycles of Catalytic Results of Prepared Materials

The results of two-cycle catalytic experiment of several EX and EM samples are shown here as examples. No significant variation between the these cycles of experiment was observed.

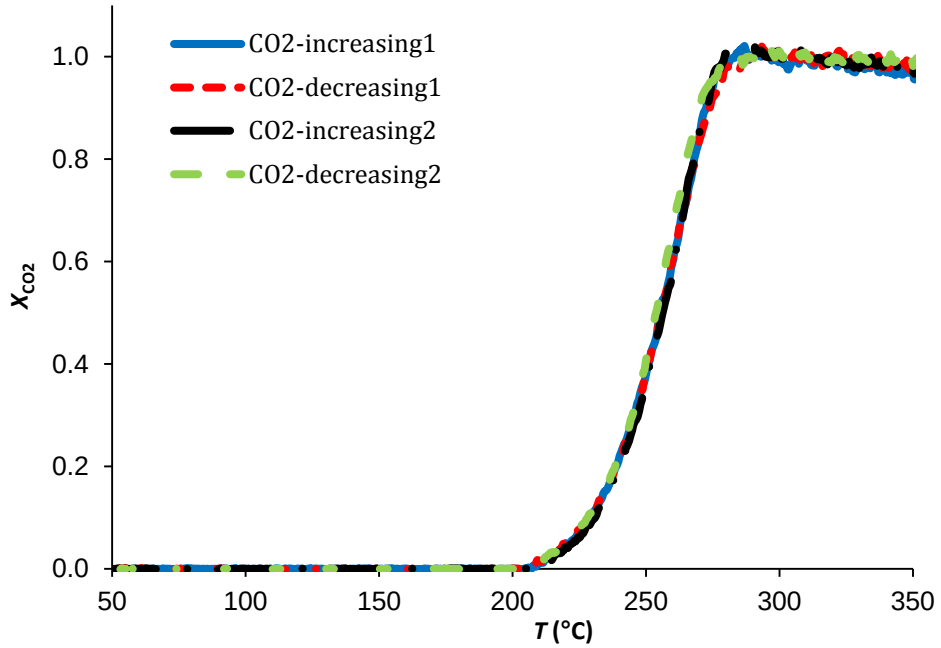


Figure A9: Catalytic performance of CuO CX D<0.1 mm for ethyl acetate oxidation (two cycles of increasing and decreasing temperature are shown).

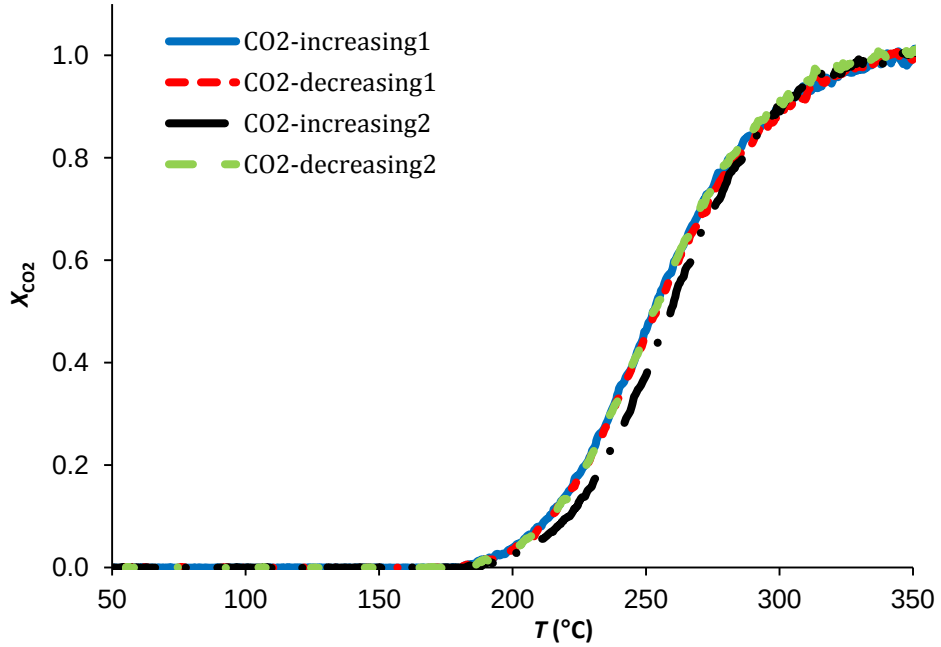


Figure A10: Catalytic performance of NiO CX for ethyl acetate oxidation (two cycles of increasing and decreasing temperature are shown).

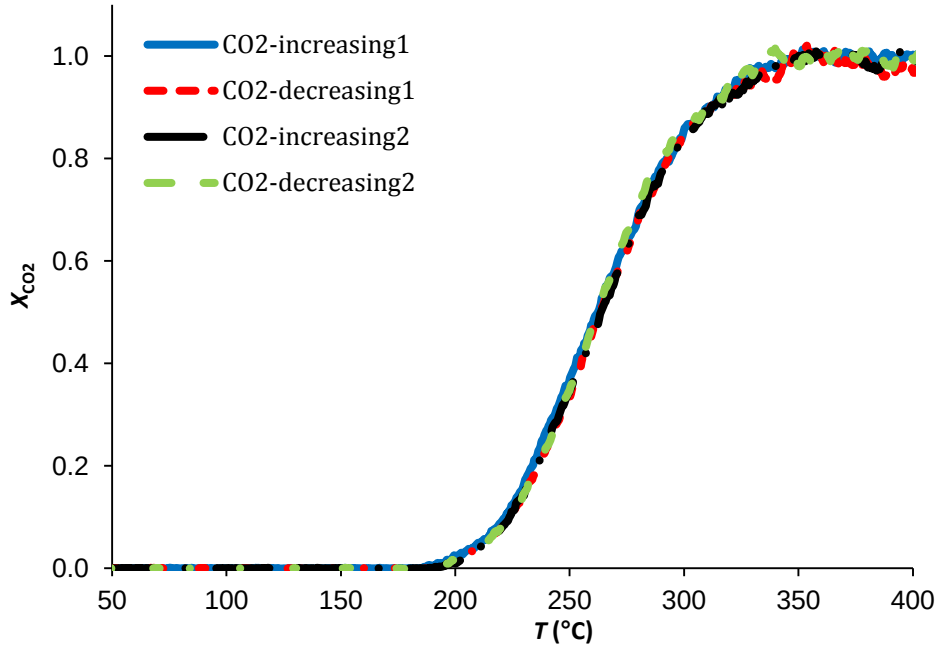


Figure A11: Catalytic performance of Ce-Cu CX 1:1 for toluene oxidation (two cycles of increasing and decreasing temperature are shown).

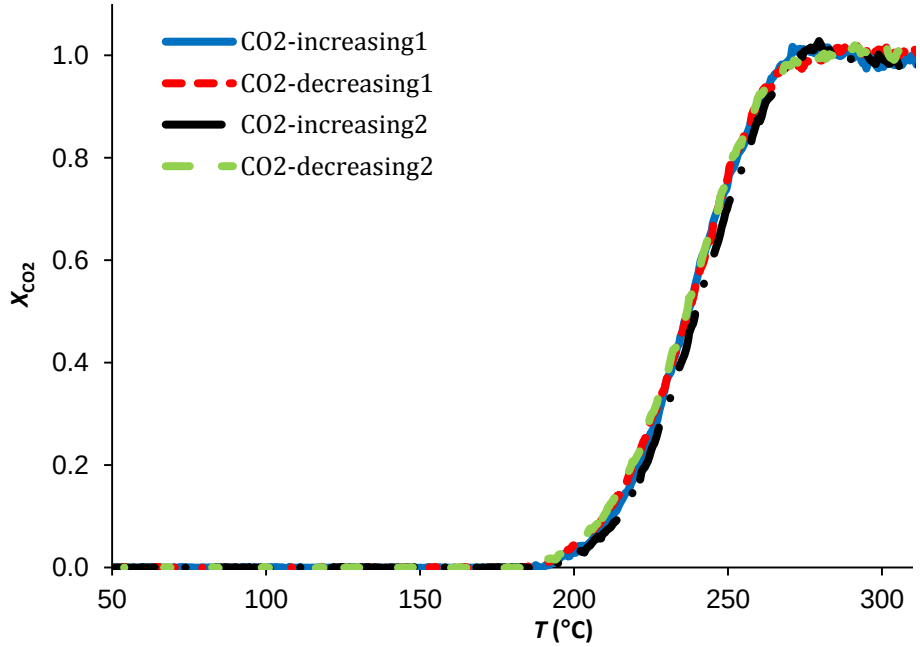


Figure A12: Catalytic performance of Ce-Ni EM 1:2 for ethyl acetate oxidation (two cycles of increasing and decreasing temperature are shown).

## Appendix 2: Impregnation Efficiency

The Spv-ratio expresses the relationship between added volume of the precursor solution and the available pore volume of the active carbon, given by:

$$Spv\text{-}ratio = \frac{V_{\text{solution}}}{m_{\text{AC}} \cdot v_{\text{pore}}},$$

where $V_{\text{solution}}$ is the volume of the precursor solution (ml), $m_{\text{AC}}$ is the mass of the activated carbon (g) and $v_{\text{pore}}$ the specific pore volume (ml/$g_{AC}$) of active carbon [47].

This relationship was used in the synthesis of exotemplated CuO, NiO and $Fe_2O_3$ in contrast to the common procedure used in [13, 24, 45] to study the impregnation efficiency. Based on Spv-ratio, 3.4 ml of precursor was used for CX templated material and 1.7 ml for CROX templated material, whereas following the literature proposed procedure, 7 ml of precursor was used in both CX and CROX templated samples.

Specific pore volume of CGAC is 0.98 ml/g [52]. This carbon material has a BET surface area of 736 $m^2$/g.

As mentioned in the thesis of O.C. Gobin, Martinez Joaristi found out that a small amount of isopropanol reduces significantly the surface tension of the nitrate solutions and thus improves the penetration of the precursor molecules into the pore system [47]. Therefore, 1 ml of isopropanol was added to selected parallel samples for copper oxides and nickel oxides for the impact study. Also the influence of filtration was investigated for impregnation efficiency. The effect of pre-drying was studied with the series of exotemplated Ce-Ni samples.

1. Effect of Addition of Isopropanol and Application of Filtration

As can be seen in Table B1, the amounts of copper oxide formed, compared with the theoretical amounts, are the same for CX1, CX2 and CX5, which were made without filtration. The addition of isopropanol made no difference on the amount of final oxide

obtained. For samples CX3 and CX4, 1 ml of isopropanol was added along with the application of filtration. The resulted amounts of CuO were lower than in CX5 which was prepared without filtration. The addition of isopropanl did not improve the impregnation efficiency of CX templated CuO. The combination of adding isoproanol with applying filtration reduces the resulted amount of product.

Table B1: Impregnation efficiency of CuO made by EX using CX. Theoretical amount of oxide was calculated assuming the formation of CuO in all samples.

| **Material** | **ID** | **Isopropanol** | **Filtration** | **SPV-ratio** | **Pre-drying** | **% of the theoretical amount of oxide** |
|---|---|---|---|---|---|---|
| CuO CX | 1 | - | - | + | + | 54 |
| | 2 | - | - | + | + | 54 |
| | 3 | + | + | + | + | 43 |
| | 4 | + | + | + | + | 47 |
| | 5 | + | - | + | + | 54 |

Table B2: Impregnation efficiency of NiO made by EX using CX. Theoretical amount of oxide was calculated assuming the formation of NiO in all samples.

| **Material** | **ID** | **Isopropanol** | **Filtration** | **SPV-ratio** | **Pre-drying** | **% of the theoretical amount of oxide** |
|---|---|---|---|---|---|---|
| NiO CX | 1 | - | - | + | + | 50 |
| | 2 | - | - | + | + | 37 |
| | 3 | + | + | + | + | 38 |
| | 4 | + | + | + | + | 27 |
| | 5 | + | - | + | + | 43 |

For nickel oxide, larger deviations were found in the oxide percentage of the actual amount and the theoretical value between the duplicate samples (Table B2). But it can be concluded, from the results of the irst four samples, that the combination of the addition of isopropanol and suction filtration lead to lower efficiency in impregnation.

No obvious promotion in the amount of product could be observed between the first two samples and CX5, in relation to the addition of isopropanol.

2. Procedure Based on Spv-Ratio

Table B3 shows the efficiency of impregnation calculated based on Spv-ratio and following the procedure described by Schwickardi et al [45]. Samples prepared with isopropanol during impregnation have relatively lower amount of CuO. Upon addition of 7 ml of precursor, higher quantities of oxide were obtained with and without isopropanol (CROX2 vs. CROX4 and CROX3 vs. CROX5). As for CROX3 (7 ml of precursor used), the efficiency of impregnation of 112% is theoretically impossible but, in practice, this could result from insufficient filtration time, insufficient filtration strength or failure in pressing out the excess precursor between the two pieces of filter paper. Filtration was applied in CROX2 to CROX5 samples, however not in CROX1, which probably is the reason why higher amounts of CuO were obtained than in the CROX5 sample, as potentially filtration can draw the impregnated precursor out of the pores of the carbon template, leading to lower amount of final oxide product.

Table B3: Impregnation efficiency of CuO made by EX using CROX. Theoretical amount of oxide was calculated assuming the formation of CuO in all samples.

| **Material** | **ID** | **Isopropanol** | **Filtration** | **SPV-ratio** | **Pre-drying** | **% of the theoretical amount of oxide** |
|---|---|---|---|---|---|---|
| CuO CROX | 1 | - | - | + | + | 91 |
| | 2 | + | + | + | + | 77 |
| | 3 | - | + | - | + | 112 |
| | 4 | + | + | - | + | 90 |
| | 5 | - | + | + | + | 68 |

For nickel oxides made with CROX, less amount of oxide was obtained upon addition of isopropanol (CX3 vs. CX4 in Table B4), as all samples were filtered. The use of 7 ml of precursor in impregnation did not increase much the resulting amount of oxide. The same tendency could be observed for the CROX templated iron oxides, as shown in

Table B5. Addition of isopropanol, especially with the application of filtration in sample preparation, was found to have an adverse effect on the impregnation efficiency.

Table B4: Impregnation efficiency of NiO made by EX using CROX. Theoretical amount of oxide was calculated assuming the formation of NiO in all samples.

| **Material** | **ID** | **Isopropanol** | **Filtration** | **SPV-ratio** | **Pre-drying** | **% of the theoretical amount of oxide** |
|---|---|---|---|---|---|---|
| NiO CROX | 1 | + | + | + | + | 89 |
| | 2 | - | + | - | + | 96 |
| | 3 | - | + | - | + | 97 |
| | 4 | + | + | - | + | 88 |

Table B5: Impregnation efficiency of $Fe_2O_3$ made by EX using CROX. Theoretical amount of oxide was calculated assuming the formation of $Fe_2O_3$ in all samples.

| **Material** | **ID** | **Isopropanol** | **Filtration** | **SPV-ratio** | **Pre-drying** | **% of the theoretical amount of oxide** |
|---|---|---|---|---|---|---|
| $Fe_2O_3$ CROX | 1 | - | - | + | + | 47 |
| | 2 | + | + | + | + | 52 |
| | 3 | - | + | - | + | 47 |
| | 4 | + | + | - | + | 43 |
| | 5 | + | - | + | + | 34 |
| | 6 | + | + | + | + | 23 |

According to the above data, addition of isopropanol along with filtration reduces the efficiency of impregnation. This phenomenon probably comes from the fact that isopropanol can reduce the surface tension of the precursor, and enhance the penetration of the precursor into the pores of the templates. On the other hand, the impregnated precursor with isopropanol in the pores of the templating materials can be more easily drawn off, especially when filtration is applied. Consequently, the amount of precursor impregnated is relatively lower than with the impregnation done without addition of isopropanol.

From the series of nickel and iron samples made with CROX, it can be seen that addition of 7 ml of precursor made no difference in the impregnation, compares to the method taking Spv-ratio into account. However, for copper samples presented in Table B3, those prepared with 7 ml of precursor had approximately 10% more amount of oxide than those made with 1.7 ml of precursor. A possible explanation for this could come from the uncertainties in the removal of excess precursor. As adequate filtration level is hard to define and control, while pressing out the excess of precursor with filter paper, it is uncertain whether an excess of precursor is still left around the surface of template particles or if impregnated precursor is drawn out of the pores. This could also provide the clue for why highest amount of iron oxide resulted in CROX2, whereas lowest in CROX6, both of which followed the same preparation procedure. A small left-over of precursor solution can be considered as acceptable, as it can catalyze the combustion of carbon materials used as templates [36, 47]. However, the existence of a large excess of precursor in the impregnated samples can cause the formation of metal oxides on the surface of the template particles, which basically resemble the oxides made from direct precursor calcinations, bearing less interesting characters, such as low surface area.

3. Effect of Pre-Drying of Templating Material

Parallel CX templated Ce-Ni samples were used to study the effect of preliminary drying of the template material.

The first three materials in Table B6 were prepared with preliminary drying. CX1 was made with 7 ml of precursor in the impregnation stage and no data was recorded on the amount of precursor used for CX3. Comparing CX2 and CX5, it can be seen that preliminary drying of the templaing material led to higher amounts of oxide, whereas lower amount was observed in CX6 in comparison to CX4. However, if the quantity of precursor used in CX3 was relevant to that in CX4, then it seems that pre-drying can lead to more precursor impregnated. But proper conclusion on the effect of pre-drying of templates is hard to be drawn at this stage, as uncertainties were brought by the application of filtration in material synthesis. Further investigation should be carried out on this issue with the elimination of filtration in the preparation procedure.

Table B6: Impregnation efficiency of Ni-Ce made by EX using CX. Theoretical amount of oxide was calculated assuming the formation of NiO and $CeO_2$ in all samples.

| **Material** | **ID** | **Isopropanol** | **Filtration** | **SPV-ratio** | **Pre-drying** | **% of the theoretical amount of oxide** |
|---|---|---|---|---|---|---|
| Ce-Ni CX | 1 | - | + | - | + | 89 |
| | 2 | + | + | + | + | 61 |
| | 3 | - | + | \ | + | 64 |
| | 4 | - | + | + | - | 62 |
| | 5 | + | + | + | - | 50 |
| | 6 | - | + | + | + | 52 |